



**KTH Industrial Engineering
and Management**

Exploring the Electronic and Optical Properties of Cu(In,Ga)Se₂

Rongzhen Chen

Licentiate Thesis

School of Industrial Engineering and Management, Department of
Materials Science and Engineering, KTH, Sweden, 2015

ISBN 978-91-7595-453-0

Materialvetenskap
KTH
SE-100 44 Stockholm
Sweden

Akademisk avhandling som med tillstånd av Kungliga Tekniska Högskolan framlägges till offentlig granskning för avläggande av licentiatexamen fredagen den 6e mars 2015 kl 11:00 i konferensrummet (N111), Materialvetenskap, Kungliga Tekniska Högskolan, Brinellvägen 23, Stockholm.

© Rongzhen Chen, March, 2015

Tryck: Universitetsservice US AB

Abstract

Chalcopyrite copper indium gallium diselenide ($\text{Cu}(\text{In}, \text{Ga})\text{Se}_2 \equiv \text{CuIn}_{1-x}\text{Ga}_x\text{Se}_2$) is today a commercially important material in the thin-film solar cell technology, and it is also in many aspects a very interesting material from a scientifically point of view.

In this licentiate thesis, details in the electronic structure of $\text{CuIn}_{1-x}\text{Ga}_x\text{Se}_2$ alloy ($x = 0.0, 0.5$, and 1.0) and its optical response are explored by means of the all-electron and full-potential linearized augmented plane wave method in conjunction with the density functional theory. The energy band dispersions are parameterized for the three uppermost valence bands (VBs; $v1$, $v2$, and $v3$ where $v1$ is the topmost band) and the lowest conduction band (CB; $c1$), based on the $\mathbf{k} \cdot \mathbf{p}$ method but expanded up to high order. To illustrate the non-parabolic, the constant energy surfaces are presented for the three topmost VBs as well as for the lowest CB.

It is demonstrated that the VBs and CB are anisotropic at the Γ -point, and even more anisotropic and non-parabolic away from the Γ -point. The effect originates from the crystal-field and the spin-orbit split-off energies. This implies that the Γ -point effective mass is not suitable to describe the materials properties such as band filling and strong excitation effects. Instead, the thesis provides the effective electron and hole mass tensors at the Γ -point in the Brillouin zone, but also an energy-dependent effective mass which can better describe both the transport and band filling effect in further experimental and theoretical analyses of the materials.

Based on the parametrized energy bands, the density-of-states as well as the temperature dependence of the Fermi energy level and carrier concentrations are determined for intrinsic and p -type $\text{CuIn}_{1-x}\text{Ga}_x\text{Se}_2$. The results are compared with corresponding results for the commonly used parabolic approximation of the bands.

Furthermore, the dielectric function of $\text{CuIn}_{0.5}\text{Ga}_{0.5}\text{Se}_2$ is calculated, and the band-to-band optical transitions are analyzed. The electronic origins of the observed interband critical points of the optical response are discussed. The theoretical results are compared with the experiment data based on $\text{CuIn}_{0.7}\text{Ga}_{0.3}\text{Se}_2$ at the temperatures 40 and 300 K, demonstrating that the overall shapes of the calculated and measured dielectric function spectra are in good agreement. We find that $v1 \rightarrow c1$ and $v2 \rightarrow c1$ transitions in the Brillouin zone edge are responsible for the main absorption peaks at 3.0 and 3.1 eV. However, also the energetically lower VBs contribute significantly to the high absorption coefficient.

Preface

List of included publications:

- I **Parameterization of CuIn_{1-x}Ga_xSe₂ (x = 0, 0.5, and 1) energy bands**
R. Chen and C. Persson, *Thin Solid Films* **519**, 7503 (2011).
- II **Band-edge density-of-states and carrier concentrations in intrinsic and p-type CuIn_{1-x}Ga_xSe₂**
R. Chen and C. Persson, *Journal of Applied Physics* **112**, 103708 (2012).
- III **Dielectric function spectra at 40 K and critical-point energies for CuIn_{0.7}Ga_{0.3}Se₂**
S.G. Choi, R. Chen, C. Persson, T.J. Kim, S.Y. Hwang, Y. D. Kim, and L. M. Mansfield, *Applied Physics Letters* **101**, 261903 (2012).

My contribution to the publications:

- Paper I:** modeling, analysis of result, literature survey; the manuscript was written jointly.
- Paper II:** modeling, analysis of result, literature survey; main part of the manuscript was written.
- Paper III:** all calculations, analysis of the theoretical part, part of literature survey; the manuscript was written jointly.

Publications not included in the thesis:

Book chapter:

- IV **Electronic structure and optical properties from first-principles modeling**
C. Persson, R. Chen, H. Zhao, M. Kumar, and D. Huang, Chapter in “Copper zinc tin sulphide-based thin film solar cells”, edited by K. Ito (John Wiley & Sons, 2014).

International conference contributions:

- V **Band structure and optical properties of CuInSe₂**
R. Chen and C. Persson, *Advanced Materials Research Journal* **894**, 254 (2014).
4th Int. Conf. on Adv. Mater. Res (ICAMR-4), Macao, China, 23–24 Jan. 2014.

VI Electronic modeling and optical properties of CuIn_{0.5}Ga_{0.5}Se₂ thin film solar cell

R. Chen and C. Persson, *J. Appl. Math. & Phys.* **2**, 41 (2014).

Conf. on New Adv. Cond. Matter Phys. (NACMP 2014), Shenzhen, 14–16 Jan 2014.

Table of Contents

Abstract	iii
Preface	v
Table of Contents	vii
INTRODUCTION	1
1 Solar cell physics	2
1.1 Solar energy	2
1.2 Solar cells	4
1.3 Single-junction	4
1.4 Solar cell materials	9
1.4.1 Crystalline silicon	10
1.4.2 Gallium arsenide	11
1.4.3 Thin-film materials	11
2 Copper indium gallium diselenide	13
2.1 Crystal structure	13
2.2 Optical properties and defects	14
2.3 Solar cell structure	15
3 Computational methods	17
3.1 The quantum many-body problem	17
3.2 The Born-Oppenheimer approximation	18
3.3 Solving the many-body problem	20
3.3.1 Hartree approximation	20
3.3.2 Hartree-Fock approximation	23
3.3.3 Density functional theory	24
3.3.4 Kohn-Sham equation	27
3.3.5 The exchange-correlation potential	29
3.4 Solving the secular equation	30
3.5 Full-potential linearized augmented plane wave method	32

3.5.1	Introduction	32
3.5.2	Wavefunction	33
3.5.3	Effective potential	36
3.6	Dielectric function	36
3.7	Spin-orbit coupling	37
3.7.1	Dirac equation	37
3.7.2	Derivation of spin-orbit coupling	38
3.8	$\mathbf{k} \cdot \mathbf{p}$ method	40
SHORT SUMMARY OF THE PAPERS		45
4	Concluding remarks	46
4.1	Summary of the papers	46
4.2	Conclusions and future perspectives	51
Acknowledgements		55
Bibliography		57
COMPILATION OF SCIENTIFIC PAPERS		65
5	Work presented in scientific journals	66
5.1	Paper I: "Parameterization of $\text{CuIn}_{1-x}\text{Ga}_x\text{Se}_2$ ($x = 0, 0.5$, and 1) energy bands"	66
5.2	Paper II: "Band-edge density-of-states and carrier concentrations in intrinsic and <i>p</i> -type $\text{CuIn}_{1-x}\text{Ga}_x\text{Se}_2$ "	72
5.3	Paper III: "Dielectric function spectra at 40 K and critical-point energies for $\text{CuIn}_{0.7}\text{Ga}_{0.3}\text{Se}_2$ "	84

INTRODUCTION

Chapter 1 Solar cell physics

1.1 Solar energy

With the increasing energy consumption, more and more energy or power is needed. According to the statistical review of world energy on 2014 [1] (**Fig. 1.1**), the required energy is mainly satisfied by fossil fuels (mainly coal, petroleum, and natural gas), with a market share of around 87%. The total energy consumption is between 12000 and 13000 million tonnes oil equivalent (MTOE), which is equivalent to around 15 terawatts [2]. Normally, one light bulb at our homes consumes between 50 and 100 watts of energy, and 1 terawatt implies 10 billion of 100 watts light bulbs are lighted at the same time. Unfortunately, fossil fuels are very limited energy and non-renewable resources. One day, which is not far from now, they will be dissipated due to the energy consumption growth.

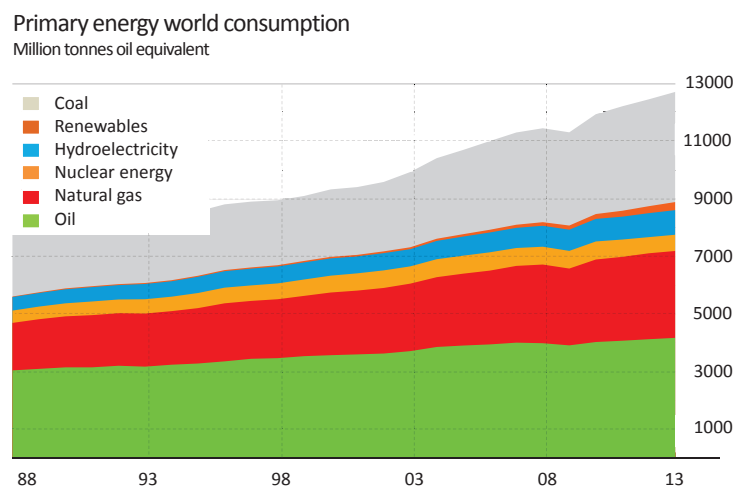


Figure 1.1. Primary energy world consumption in 2014 [1].

By the year of 2050, the total world energy consumption will double [3]. Therefore, it is urgent to explore more sustainable and environmentally friendly energy sources. In **Fig. 1.1**, renewable energy (mainly solar energy, wind power, and geothermal energy)

in 2013 accounts for around 2% of the energy consumption globally. It is important to focus on renewable energy research from a long term point of view. Solar energy technologies are one of the hot topics among renewable energy research considering the point of CO₂ free, reliable energy supply, and operation in silence.

Solar energy technologies are a way to produce electricity from sunlight. Sunlight is a portion of radiation by the sun, such as ultraviolet, visible, and infrared light. Spectrum of the sunlight is given in **Fig. 1.2**. Solar spectrum is established by air mass (AM) at the photovoltaic (PV) industry, which defines a direct optical path length through the Earth's atmosphere [4]. AM1.5 and AM0 are two important references of spectra: AM1.5 is the air mass at a solar zenith angle of 48.19 degree, and AM0 is the solar spectrum outside of the atmosphere. Generally, solar spectrum at AM1.5 is used in PV field in order to standardize solar cell measurements. In **Fig. 1.2**, absorption in the atmosphere is quite strong by gases, dust, and aerosols, as well as scattering light from air molecules [5].

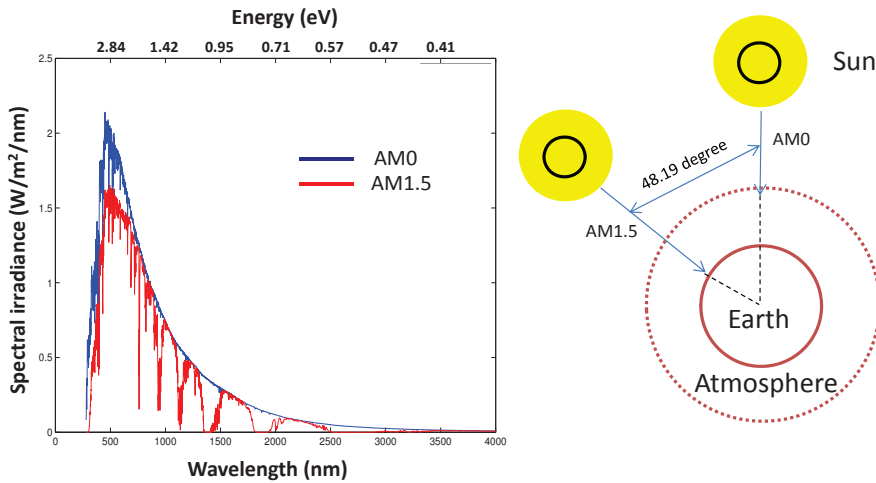


Figure 1.2. Spectral irradiance AM1.5 and AM0.

There are mainly three types of solar energy technologies [6, 7]. The first one is solar thermal technology, which utilizes flat sunlight collector plates to harness energy from sunlight to heat water for use in industries, homes, and pools. The advantage of solar thermal technology is that the conversion efficiency is relatively higher compared with other solar energy technologies. The second one is solar chemical technology, which takes advantage of solar energy by absorbing sunlight in a chemical reaction. However, the conversion efficiency of this technology is quite low so far. The last one is solar photovoltaics (solar cell), which is a way to utilize solar panels to convert sunlight into electricity. The installation of solar panel is easier, and it occupies less space and needs less maintenance compared with solar thermal technology. The conversion efficiency of solar cell is higher than the one of solar chemical technology. However, all the three solar energy technologies are environmentally friendly.

1.2 Solar cells

In the worldwide, the conversion efficiencies in all different types of solar cells are improved remarkably [8]. From Fig. 1.3, the highest efficiency for multijunction cells, crystalline silicon (c-Si) cells, thin-film technologies, and new emerging cells are 44.7%, 27.6%, 23.3%, and 20.1% [9–12]. Therefore, solar cell is a very important and promising way to produce renewable energy.

Multijunction cells are the cells which contain several *p-n* junctions (or subcells). They have different band-gap for each *p-n* junction. Therefore, different wavelengths of sunlight are absorbed for each junction. For example, wider band-gap junction is at the front of the cell, which absorbs photons with high energy; the junction with low band-gap absorbs photons with relatively low energy. In this configuration, the conversion efficiency is higher than the one of single *p-n* junction, for example, the maximum conversion efficiency is 44.7% by Soitec [9] using four-junction or more in Fig. 1.3. Solar cells based on c-Si are the most widely utilized in the PV industries. It has two types in c-Si photovoltaics: monocrystalline silicon and multicrystalline silicon. Solar cells based on c-Si have high efficiency, for example, the maximum conversion efficiency is 27.6% with concentrator by Amonix [10] and maximum 25.6% without concentrator by Panasonic [13] in Fig. 1.3. Thin-film solar cells are the cells which are made by depositing one or several thin layers. They allow cells to be rather flexible and result in lower weight. The maximum conversion efficiency for thin-film solar cells is lower than that for c-Si today, which is 23.3% using copper indium gallium diselenide ($\text{CIGS} \equiv \text{CuIn}_{1-x}\text{Ga}_x\text{Se}_2$) with concentrator by national renewable energy laboratory (NREL) [11] and is 21.7% without concentrator by the center for solar energy and hydrogen research (ZSW) in Stuttgart [14] in Fig. 1.3. The emerging PV represents the newest ways to create electricity from sunlight and potentially with higher conversion efficiency, such as perovskite cells in Fig. 1.3. The maximum conversion efficiency of perovskite cells already reached 20.1% in Korea research institute of chemical technology (KRICT) [12]. Perovskite cells jump into the world of solar cells only from 2009 [15, 16], and the conversion efficiency is improved remarkably within 5 years. In this type of emerging solar cells, also dye-sensitized cells, organic cells, and quantum dot cells have the maximum conversion efficiencies of 11.9% [17], 11.1% [18], and 9.2% [19], respectively. Certainly, search and optimization of alternatively solar cell materials are still an ongoing active area today.

1.3 Single-junction

The *p-n* junction is a fundamental building block of solar cells. Single *p-n* homojunction will be explored in this section. The more detailed information about this topic can be found in Refs. [20–22].

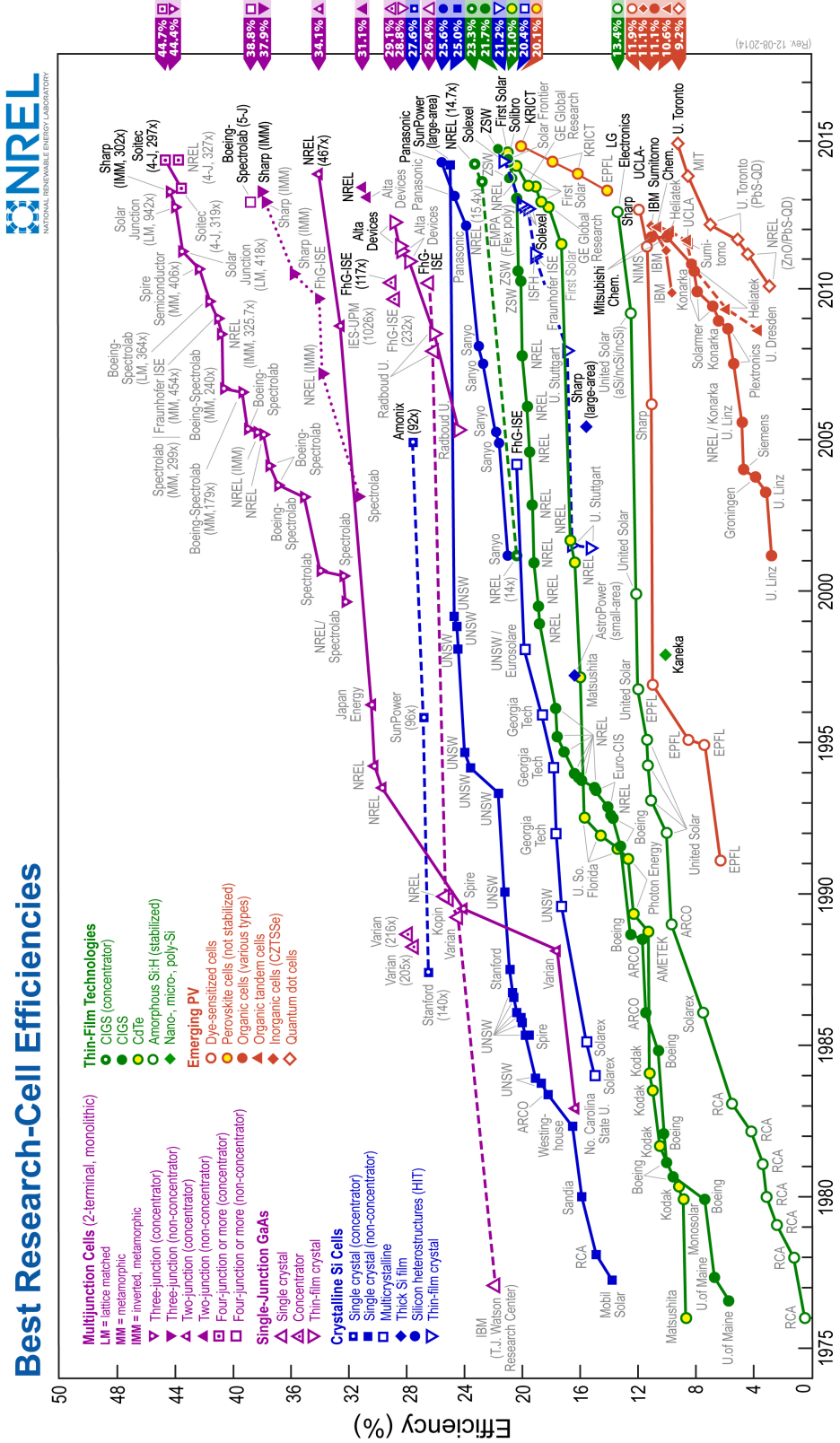


Figure 1.3. Best research-cell efficiencies. Figure is from national renewable energy laboratory (NREL), U.S.A. [8].

We start from separate pieces of *n*- and *p*-type materials at room temperature (assume that all the donor (acceptor) atoms are positively (negatively) ionized at room temperature). In Fig. 1.4, the left panel shows illustration of the *n*- and *p*-type materials. The *n*-type material has many free negatively charged electrons moving freely inside the material, and there are numbers of positively charged immobile donor ions as well. Similarly, a *p*-type material has many free positively charged holes moving freely in the material, and there are numbers of negatively charged immobile acceptor ions as well. However, both the *n*- and *p*-type materials are still neutral. The corresponding Fermi levels are shown on the right panel. The Fermi level (E_{nf}) is close to conduction band minimum for the *n*-type material due to the many free negatively charged electrons. Conversely, the Fermi level of the *p*-type material (E_{pf}) is close to valence band maximum due to the many free positively charged holes.

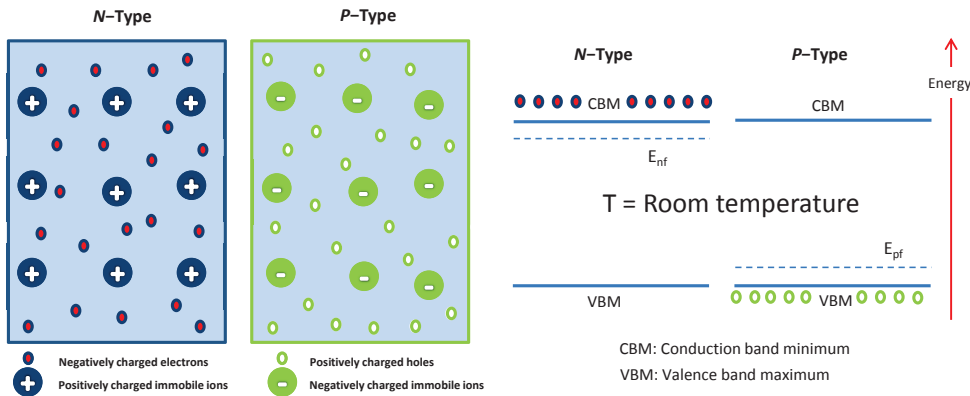


Figure 1.4. Left panel: Doped (*n*-type and *p*-type) materials in dark at room temperature. Right panel: Energy band diagram of *n*- and *p*-type materials in dark at room temperature for two-level model. Assume that all the donor (acceptor) atoms are positively (negatively) ionized at room temperature.

If the *n*-type and *p*-type materials are joined, the free electrons (holes) in the *n*-type (*p*-type) material will diffuse into the *p*-type (*n*-type) material due to the lower concentrations of electrons (holes) in the *p*-type (*n*-type) material (Fig. 1.5). In a region, which is near the interface between the *n*- and *p*-type materials, the ionized donor and acceptor ions create a "build in" electric field which points from the *n*-type material to the *p*-type material. This causes the drift of carriers in the opposite direction. The "build-in" electric field forces the electrons (holes) back into the *n*-type (*p*-type) material. At certain point, the whole material can reach a stable equilibrium due to the achieved balance between diffusion and drift. Formation of the "build-in" electric field is rather important for solar cells, even though there is no current in the material so far. In the following text, the region which forms the "build-in" electric field is also called space charge region (SCR). The different Fermi levels for the *n*-type and *p*-type materials become equal at the stable equilibrium. Therefore, the energy bands bend over and create a potential

barrier near the junction (right panel in Fig. 1.5). At last, there is an internal potential V_{bi} in the junction, which can block the diffusion.

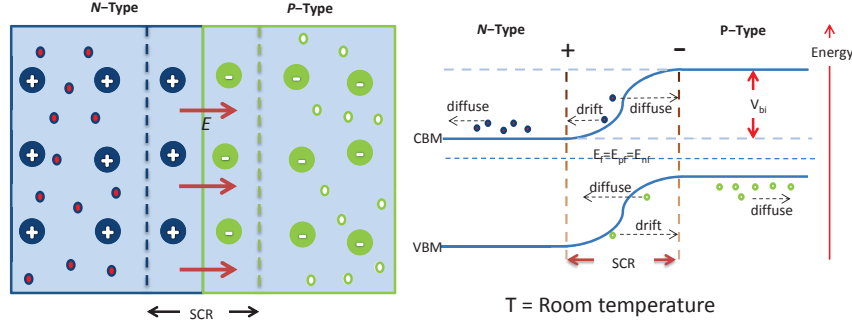


Figure 1.5. Left panel: The p - n homojunction in dark at room temperature. Right panel: Energy band diagram of the p - n homojunction at the equilibrium in dark at room temperature for two-level model.

The p - n junction cell with and without illumination are discussed in Fig. 1.6 and Fig. 1.7. If there was a wire with certain resistance connecting the n - and p -type materials, there is no current in the wire under the condition of dark (no illumination). However, if the light shines on the cell, a current can be generated from the p -type to the n -type side (conventional current). The reason is that pairs of electron-hole are generated inside the p - n junction cell. At the same time, recombination of the paired electron-hole occurs. The rate of paired electron-hole generation is faster than that of recombination for paired electron-hole. Therefore, net current occurs. Apparently, there are three regions in the whole junction cell where the electrons go from VBs to CBs, the n -type region, the p - n junction, and the p -type region. In the either n - or p -type region (especially, region which is far away SCR), the electron–hole pairs only exist for a short time, and it is most probable that electrons will jump down from CBs to VBs again. However, the electron–hole pairs can be separated in the p - n junction region due to the "build-in" electric field. Therefore, current is generated. Actually, the electron–hole pairs in the either n - and p -type material (especially, for them which are near SCR) also have the chance to diffuse into the SCR, which can contribute to generate current or to reduce current.

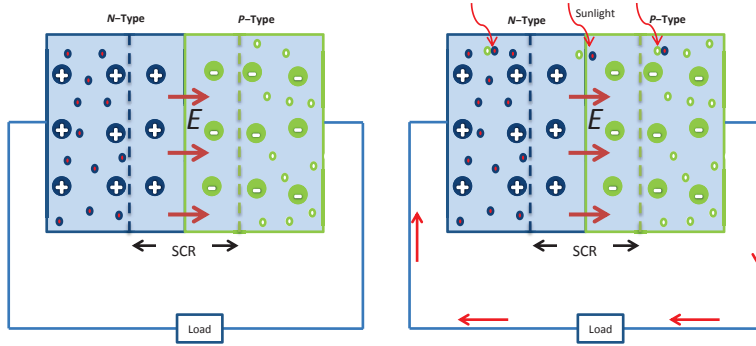


Figure 1.6. Left panel: the p - n homojunction at dark with load. Right panel: the p - n homojunction under illumination with load at room temperature.

In Fig. 1.7, the SCR becomes more "smooth" due to the extra load, such as light bulb. It is equivalent to apply external potential. The stabilized Fermi level at a stable equilibrium splits under illumination. The chemical potential ($\Delta\mu$) is created, which is considered as the electron charge times the voltage across the device. The generation and recombination by impurities are not analyzed in here.

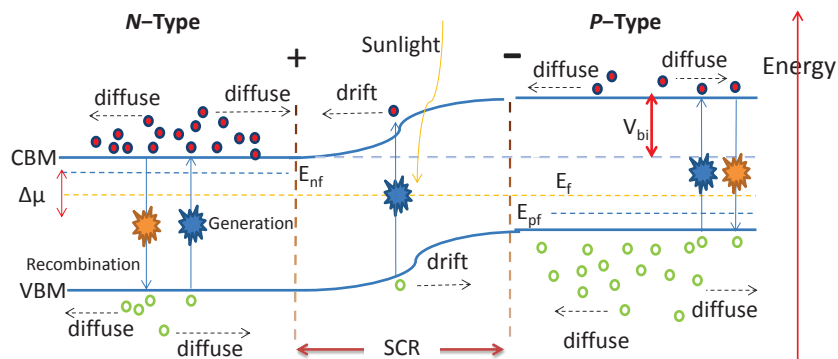


Figure 1.7. Energy band diagram of the p - n homojunction under illumination with load for two-level model.

Current-voltage characteristic is defined in Fig. 1.8 with some important parameters of solar cells. V_{oc} and I_{sc} are the open circuit voltage (the maximum voltage) and short circuit current (maximum current), respectively. V_{mp} and I_{mp} are the voltage and current, respectively, which yield the maximum power. The maximum power generated by solar cells is $P_{out} = V_{mp} \times I_{mp}$. That is the rectangle bounded by dashed lines in Fig. 1.8.

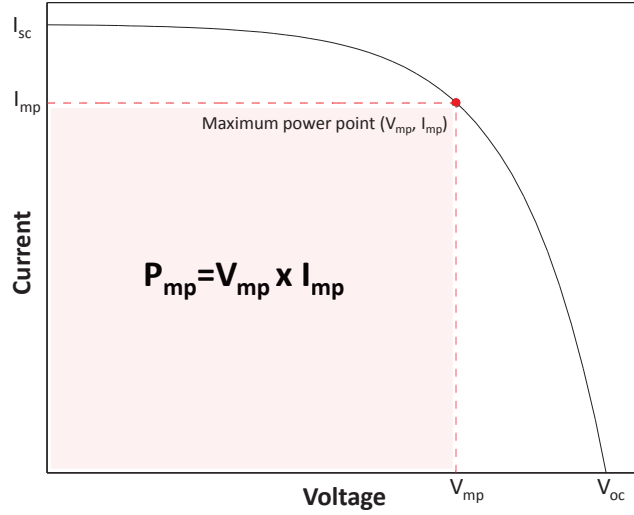


Figure 1.8. Current-voltage characteristic of a solar cell under illumination.

Solar cell performance is often represented by fill factor (FF) and power conversion efficiency (η):

$$FF = \frac{P_{out}}{V_{oc} \cdot I_{sc}} = \frac{V_{mp} \cdot I_{mp}}{V_{oc} \cdot I_{sc}} \quad (1.1)$$

$$\eta = \frac{P_{out}}{P_{in}} = \frac{FF \cdot V_{oc} \cdot I_{sc}}{P_{in}}. \quad (1.2)$$

Here, P_{in} is incident photon power per second. Conversion efficiency of solar cells is proportional to the FF , V_{oc} , and I_{sc} . There are several aspects affecting the conversion efficiency. The V_{oc} is directly proportional to band-gap of a material, and the I_{sc} is proportional to number of absorbed photons. When band-gap is decreased, more spectrum of sunlight can be absorbed. However, the V_{oc} will be reduced in this case. More importantly, excess energy of photons is lost due to thermalization in solar cells. When band-gap is increased, more transparency loss from photons with energy lower than the band-gap occurs. One can find more detailed analysis of conversion efficiency in Ref. [20].

1.4 Solar cell materials

In 1839, French physicist A. E. Becquerel [23] revealed the photovoltaic effect for the first time. Charles Fritts built the first solid state photovoltaic (PV) cell using semiconductor selenium in 1883 [24, 25]. It is not until 1941 that the first silicon-based solar cell was demonstrated [26, 27]. Today, there are many different types of solar cell materials. The

reason why the best solar cell material is not found yet is that it is expected to be not only high efficiency but also environmentally friendly, and low cost. It requires not only that the growth and manufacturing process of solar cell materials should be cheaper, but also that the devices should have longer application life. Moreover, the raw material should be abundant and non-toxic as well. In this section, four main solar cell materials are discussed briefly: silicon (Si), gallium arsenide (GaAs), cadmium telluride (CdTe), copper indium gallium diselenide (CIGS).

Potential solar cell materials need to fulfill several properties, such as large absorption coefficient and a band-gap energy between 0.7 to 2.0 eV. Under these conditions, many materials can be found. However, other properties are needed to be considered as well, such as cost and environmental safety. Thereby, only part of them are suitable to be utilized in reality.

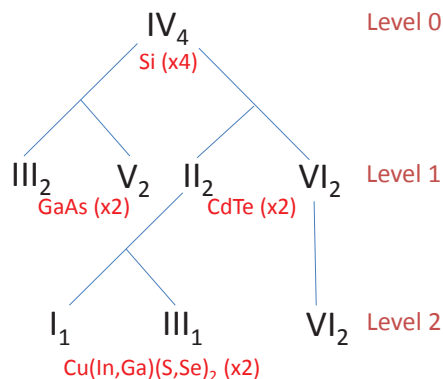


Figure 1.9. Tree of tetragonal bonded semiconductors, the roman numerals mean group numbers in the chemical element periodic table, and the subscript implies number of elements.

In Fig. 1.9, formation of tetragonal semiconductors is considered as a series of cation mutations where total number of valence electrons is the same and it keeps the charge neutral in the compound [28–30]. For example, group number IV element Si (level 0) with four 4⁺ ions is equivalent to two 3⁺ ions and two 5⁺ ions, such as GaAs (level 1). It is also equivalent to two 2⁺ ions and two 6⁺ ions, such as CdTe (level 1). CIGS can be derived applying the same process on group number II element on the level 1 in Fig. 1.9. This method was suggested by Goodman and Pamplin [31, 32].

1.4.1 Crystalline silicon

Solar cells based on Si dominate solar power world today, which account for more than 90% of total PV market [33]. Different forms of Si are used in this type of solar cells, that is, monocrystalline Si and polycrystalline Si. The success of Si is due to a number of reasons. For example, over 90% in the crust of Earth is composed of silicate minerals,

which yields huge available Si. Moreover, it has higher conversion efficiency, and it is also proved that solar cells based on Si has excellent stability and reliability under outdoor conditions. However, Si also has drawbacks. It has an indirect band-gap, hence it has a lower optical absorption coefficient. In order to absorb incident sunlight fully, thicker Si (wafer) (around 0.2 mm) is required [34]. c-Si has to be high quality and defect free in order to avoid losing the carriers before collection. Last but not least, it is expensive to purify the Si from the silicate minerals, which limits the cost reduction of wafer-based Si technology.

However, solar cells based c-Si technology are still leading the market of solar cells since many companies are trying to lower the cost in the whole manufacture.

1.4.2 Gallium arsenide

GaAs has a zinc blende crystal structure with a direct band-gap around 1.5 eV at room temperature [35, 36]. Some electronic properties of GaAs are superior to Si, such as higher electron mobility, higher saturated electron velocity, and absorb sunlight more efficiently due to the direct band-gap. The optimum band-gap for a single junction solar cells is suggested around 1.3 eV by theoretical calculation from Henry (1980) [37], who modified the original Shockley-Queisser limit [38]. Therefore, one of the applications of GaAs is solar cells. GaAs has been extensively researched since 1950s, and the first GaAs solar cell was established in 1970 by Zhores Alferov's team [39]. Today, the conversion efficiency for single junction solar cells based on GaAs is 28.8% [40]. However, the price of solar cells based on GaAs is more expensive in comparison with the price of solar cells based on Si. Researches are focusing on how to reduce the price today, and the main application of solar cells based on GaAs is in the space application. However, the arsenic toxicity should be considered as the main disadvantage of this type of solar cells.

The conversion efficiency of 44.7% for four-junction GaInP/GaAs/GaInAsP/GaInAs concentrator solar cells was achieved by Soitec on March 2014 [9].

1.4.3 Thin-film materials

Thin-film solar cells have several layers of thin-film with total thickness less than 10 μm [41]. The cost of this kind of solar cells can potentially be reduced since less materials are utilized to make thin-film solar cells. The development of thin-film solar cells started since 1970s. Currently, the maximum conversion efficiency for thin-film solar cells is 23.3% [11]. Three different thin-film materials are discussed in this section: amorphous silicon (a-Si), cadmium telluride (CdTe), and copper indium gallium diselenide (CIGS).

The a-Si is the first thin-film solar cell material reaching the large-scale production [42–44]. It has higher absorption coefficient than that of c-Si. Therefore, the thickness can be less than 1 μm . The main disadvantages a-Si solar cells is the lower conversion ef-

ficiency, the actual conversion efficiency for commercial single junction solar cells based on a-Si is between 4% and 8% [45]. This limits the development of a-Si thin-film solar cells. a-Si solar cells are suited to the situations which require low cost over high efficiency.

CdTe was first reported in the 1960s [46]. However, it was not developed rapidly until in the early 1990s. CdTe has a number of advantages as an absorber. It has higher absorption coefficient. The band-gap is around 1.45 eV, which is very near the optimum value for single-junction solar cells. The manufacturing process is easier to control, which results in the cost of manufacture is low [47]. Moreover, the conversion efficiency of commercial modules already reached 17% [48]. However, an important question should be considered in order to large-scale CdTe manufacture: cadmium toxicity and tellurium availability.

CIGS is a direct band-gap semiconductor with high optical absorption coefficient. It is seen as one of the most promising solar cell materials for the near future. It is always employed in a heterojunction structure, mainly it is with the thinner *n*-type CdS layer [49]. The 23.3% CIGS world record conversion efficiency was achieved in the laboratory [11]. The interesting part is that it can be alloyed by the ratio of $[Ga]/([Ga]+[In])$, and the band-gap can be tuned along with that. The band-gap is between 1.0 eV and 1.7 eV for this type of alloy [50–54]. CIGS does not contain any toxic element.

Chapter 2 Copper indium gallium diselenide

CIGS is a chalcopyrite-type material, which is considered as one of the most promising thin-film solar cell materials. CuInSe₂ was first synthesized by Hahn in 1953 [55]. It was first exploited as an absorber material in a single crystal solar cell in 1974 [56], and the conversion efficiency is around 5%. The first thin-film solar cell based on CuInSe₂ and CdS was invented by Kazmerski [57]. During the 1980s, Boeing Corporation did much research on the thin-film polycrystalline CIGS solar cells. To date, the highest conversion efficiency in laboratory situation for the solar cells based on CIGS is 23.3% [11]. Typically, the experimentally and commercially most interesting compound is the CIGS alloy with about 70% In and 30% Ga, that is CuIn_{0.7}Ga_{0.3}Se₂.

2.1 Crystal structure

Crystal structure of CIGS can be derived from zinc blende crystal structure of zinc selenide (ZnSe). In Fig. 2.1, the crystal structures of ZnSe and CuInSe₂ are presented. Atoms Zn are replaced by atoms Cu and In or Ga in the zinc blende of ZnSe. It requires to double the unit cell of ZnSe in the *z*-direction. The lattice parameter *c* for CIGS is not exact *2a* normally, because bond strength and lengths between Cu-Se and In-Se or Ga-Se are different [29].

Chalcopyrite CuInSe₂ and CuGaSe₂ have space group D_{2d}^{12} ($I\bar{4}2d$; space group no. 122). The conventional unit cell has four copper (Cu) atoms on Wyckoff position *4a* (S_4 point-group symmetry), four indium (In) or gallium (Ga) atoms are on position *4b* (S_4 point-group symmetry), and eight selenium (Se) atoms are on position *8d* (C_2 symmetry). The Se *8d* positions are fully defined with the position (*x*, *y*, *z*), and each anion Se atom has two inequivalent bonds $\delta(\text{Cu}-\text{Se})$ and $\delta(\text{In}-\text{Se})$ or $\delta(\text{Ga}-\text{Se})$ [58–60]. For the CuIn_{0.5}Ga_{0.5}Se₂, the structure is chosen so that each Se atom has bonds with two Cu atoms, one In, and one Ga atom. The space group is S_4^2 ($I\bar{4}$; space group no. 82) [61].

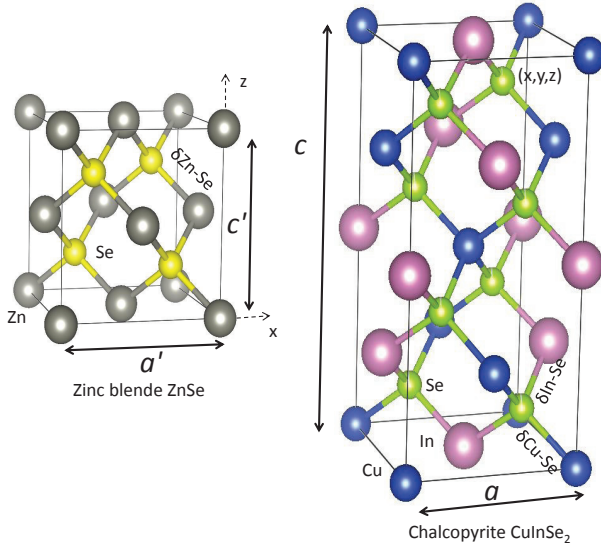


Figure 2.1. Crystal structures of zinc blende ZnSe and chalcopyrite CuInSe₂.

2.2 Optical properties and defects

CuInSe₂ has a direct band-gap around 1.0 eV, and the absorption coefficient is relatively higher than that of c-Si due to the direct band-gap. The quaternary CIGS alloy will be available by alloying Ga element, while the band-gap is tuned as well from 1.0 eV to 1.7 eV. The CIGS can be applied as an absorber layer for the thin-film solar cells due to the high absorption coefficient. The band-gap can be approximated by the function of Ga content (x) [62]

$$E_g(x) = 1.010 + 0.626x - 0.167x(1 - x). \quad (2.1)$$

Alloying the Ga element will decrease the electron affinity of CIGS, which will make conduction bands upward shift. However, the valence bands remain the same positions [63]. This also explains the reason why the band-gap increases with more Ga element in the CIGS. An overview of the properties of CuInSe₂ and CuGaSe₂ are described in **Table. 2.1**.

CIGS is a non-stoichiometric compound, and the high quality thin-film solar cells mainly employ Cu-poor (Cu: 22.5–24.5%) high off-stoichiometric CIGS absorber. V_{Cu} is the most important native defect in CIGS due to the low formation energy. Therefore, CIGS can be grown *p*-type easily under the condition of V_{Cu}. There are some extrinsic divalent cation donors as well, such as Zn_{Cu}, Cd_{Cu}, and Cl_{Se}. The formation energies for them are relatively low for CIS and CuGaSe₂ (CGS). In fact, CIS is possible to be *n*-type as well. However, CGS is not possible to be *n*-type under equilibrium conditions. The reason is that the low formation energy of V_{Cu} limits the possibility of achieving electronic *n*-type

Properties of CuInSe ₂ and CuGaSe ₂		
Properties	CuInSe ₂	CuGaSe ₂
Space group	D_{2d}^{12} (I-42d), no. 122 [36]	D_{2d}^{12} (I-42d), no. 122 [36]
Lattice constants (Å)	$a = b = 5.78, c = 11.55$ [36]	$a = b = 5.61, c = 11.00$ [36]
Wyckoff positions	Cu:4a, In:4b, Se:8d [58–60]	Cu:4a, Ga:4b, Se:8d [58–60]
Direct band-gap (eV)	$E_g = 1.01$ [36]	$E_g = 1.68$ [36]
Effective masses on Γ point (m_0)	Electrons: 0.08 [64] Holes(heavy): 0.71 [64]	Electrons: 0.14 [64] Holes(heavy): 1.2 [64]
Main intrinsic defects	<i>n</i> -type: V _{Se} ; In _{Cu} [65–68] <i>p</i> -type: V _{Cu} ; Cu _{In} [65–68]	<i>n</i> -type: V _{Se} ; Ga _{Cu} [65–68] <i>p</i> -type: V _{Cu} ; Cu _{Ga} [65–68]
Crystal field splitting (eV)	0.006 [36]	−0.10 [69]
Spin-orbit splitting (eV)	0.23 [36]	0.238 [36]
Dielectric constants $\varepsilon(0)$	15.7 [36]	11.0 [64]
Melting temperature (K)	1260 [36]	1310 – 1340 [36]
Thermal expansion coefficients (1/K)	a axis: 11.23×10^{-6} [36] c axis: 7.90×10^{-6} [36]	a axis: 13.1×10^{-6} [36] c axis: 5.2×10^{-6} [36]
Thermal conductivity W/(cm × K)	0.086 [70]	0.129 [36]

Table 2.1. Properties of CuInSe₂ and CuGaSe₂.

character, especially in Ga-rich CIGS [71, 72]. This may also explains why the best solar cell is with the Ga content of 30% ($x = 0.3$), however, the band-gap energy of the CIGS suggests that the optimum solar cell conversion efficiency is obtained with x between 0.5 and 0.7.

2.3 Solar cell structure

The solar cell device based on CIGS is a heterojunction device, which normally has five thin-film layers with different functional properties [73–75]. A schematic of conventional device structure is shown in Fig. 3.3

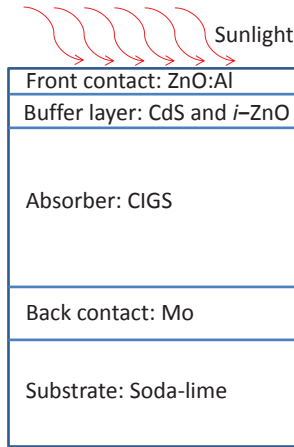


Figure 2.2. Structure of CIGS solar cell device.

Substrate is on the bottom, and there are mainly three types of substrates: soda-lime glass, metal, and polyimide. The most common substrate is the one based on soda-lime glass containing sodium (Na) with thickness 1 mm to 3 mm. The Na can improve the efficiency and reliability of the solar cells as well as process tolerance. The molybdenum (Mo) works as a back contact due to its low resistivity and stability at high temperature with thickness around 500 nm. Most important part of the device is the *p*-type absorber layer: CIGS, which has intrinsic defects and its thickness is 1500 – 2000 nm. The *n*-type buffer layer CdS is on the top of the CIGS, its thickness is around 60 nm. The intrinsic zinc oxide (*i*-ZnO) and *n*-type ZnO layers are followed, and they work as window layers. The *i*-ZnO is used to avoid damage of the CIGS and CdS from sputtering damage when depositing the ZnO:Al window layer. The *n*-type ZnO is doped by aluminum (Al) in order to get higher conductivity [76, 77]. This CIGS/CdS/ZnO structure is optimized to improve the cell performance. The detailed information about the structure CIGS solar cell device can be found in Refs. [78–80].

Chapter 3 Computational methods

3.1 The quantum many-body problem

A solid material contains a huge number of atoms (around 10^{23} cm $^{-3}$), and each atom consists of a nucleus surrounded by one or more electrons. According to the principles of quantum mechanics, all properties of a system are known if one can figure out a way to solve the quantum many-body Schrödinger equation. In this thesis, the time-independent many-body Schrödinger equation is only considered, which is given as

$$H^{en}\Psi^{en}(\{\mathbf{r}_i, \mathbf{R}_I\}) = E^{en}\Psi^{en}(\{\mathbf{r}_i, \mathbf{R}_I\}). \quad (3.1)$$

Here, superscript "en" implies that it is related with electrons and nuclei. $\Psi^{en}(\{\mathbf{r}_i, \mathbf{R}_I\})$ is defined as many-particle wavefunction, \mathbf{r}_i and \mathbf{R}_I stands for coordinators of electron and nucleus. E^{en} is defined as total energy of system. H^{en} denotes Hamiltonian [81], which is defined in atomic units as

$$\begin{aligned} H^{en} = & -\sum_i^{Ne} \frac{\nabla_i^2}{2} - \sum_I^{Nn} \frac{\nabla_I^2}{2M_I} - \sum_i^{Ne} \sum_I^{Nn} \frac{Z_I}{|\mathbf{r}_i - \mathbf{R}_I|} \\ & + \frac{1}{2} \sum_i^{Ne} \sum_{j \neq i}^{Ne} \frac{1}{|\mathbf{r}_i - \mathbf{r}_j|} + \frac{1}{2} \sum_I^{Nn} \sum_{J \neq I}^{Nn} \frac{Z_I Z_J}{|\mathbf{R}_I - \mathbf{R}_J|}. \end{aligned} \quad (3.2)$$

Here, indices i and j are used for the electrons, and I, J are used for the atomic nuclei. Z_I implies charge of the I :th nucleus. M_I denotes mass of the I :th nucleus in atomic units. The first and second terms are kinetic energy operator of the electrons and nuclei. Other terms are Coulomb interactions between electrons and nuclei, electrons and electrons, and nuclei and nuclei in sequence.

Eq. 3.1 can not be solved exactly. Moreover, the exact form of the wavefunction is unknown. To approximate the exact solution, the process of finding the solution can be divided into three different levels generally [81,82]: the first level is the Born-Oppenheimer approximation [83]; the second level is Hartree approximation [84], Hartree-Fock (HF)

approximation [85], density functional theory (DFT) [86], and Kohn-Sham (KS) equation [87]; the last level is to solve the secular equation, which is an equation solved to find eigenvalue of a matrix [81,82].

3.2 The Born-Oppenheimer approximation

Eq. 3.1 should be approximated in order to solve it. A first step is to separate the wavefunction of electron and nucleus. The Schrödinger Hamiltonian in **Eq. 3.2** has a coupling term between the electron and nucleus, thereby one can not do that simply. Positions of nuclei can be treated as fixed because the mass of nucleus is much larger than that of electron. This indicates that the electrons are seen as interacting under both the external potential caused by nuclei that are in fixed positions and that of the other electrons. The separation of motion between electrons and nuclei is called the Born-Oppenheimer approximation [83]. Since the positions of nuclei are fixed, wavefunction can be written as

$$\Psi^{en}(\{\mathbf{r}_i, \mathbf{R}_I\}) \approx \theta(\{\mathbf{R}_I\})\Psi(\{\mathbf{r}_i\}; \{\mathbf{R}_I\}). \quad (3.3)$$

Here, $\Psi(\{\mathbf{r}_i\}; \{\mathbf{R}_I\})$ denotes many-electron wavefunction in the Born-Oppenheimer approximation. Since the electrons are under the potential of nuclei, thus the wavefunction of electron is related with the nucleus positions.

Eq. 3.2 can be rewritten as

$$\begin{aligned} H^{en} &= H + H^n \\ H &= U_e + U_{ext} + U_{int} \\ H^n &= - \sum_I^{Nn} \frac{\nabla_I^2}{2M_I} + U_{nn}. \end{aligned} \quad (3.4)$$

Furthermore, all the unknown terms in **Eq. 3.4** are defined as

$$\begin{aligned}
U_e &= - \sum_i^{Ne} \frac{\nabla_i^2}{2} \\
U_{ext} &= - \sum_i^{Ne} \sum_I^{Nn} \frac{Z_I}{|\mathbf{r}_i - \mathbf{R}_I|} \\
U_{int} &= \frac{1}{2} \sum_i^{Ne} \sum_{j \neq i}^{Ne} \frac{1}{|\mathbf{r}_i - \mathbf{r}_j|} \\
U_{nn} &= \frac{1}{2} \sum_I^{Nn} \sum_{J \neq I}^{Nn} \frac{Z_I Z_J}{|\mathbf{R}_I - \mathbf{R}_J|}.
\end{aligned} \tag{3.5}$$

Here, H represents Hamiltonian for the many-electron system within the Born-Oppenheimer approximation. The subscript ext implies *external* in Eq. 3.4, thus U_{ext} describes the external potentials interaction $V_{ext}(\mathbf{r})$.

The new Schrödinger equation combined with Eq. 3.3 and Eq. 3.4 is given as

$$(H + H^n) (\theta(\{\mathbf{R}_I\}) \Psi(\{\mathbf{r}_i\}; \{\mathbf{R}_I\})) = E^{en}(\{\mathbf{R}_I\}) (\theta(\{\mathbf{R}_I\}) \Psi(\{\mathbf{r}_i\}; \{\mathbf{R}_I\})). \tag{3.6}$$

Here, $E^{en}(\{\mathbf{R}_I\})$ represents system total energy, which is \mathbf{R}_I -dependent because system wavefunction depends on nuclei positions. One ends up with the following equation taking Eq. 3.5 and Eq. 3.6.

$$\begin{aligned}
H\Psi(\{\mathbf{r}_i\}; \{\mathbf{R}_I\}) &= E(\{\mathbf{R}_I\})\Psi(\{\mathbf{r}_i\}; \{\mathbf{R}_I\}) \\
(U_{nn1} + U_{nn2} + U_{nn3} + U_{nn} + E(\{\mathbf{R}_I\}))\theta(\{\mathbf{R}_I\}) &= E^{en}(\{\mathbf{R}_I\})\theta(\{\mathbf{R}_I\}).
\end{aligned} \tag{3.7}$$

Here, $E(\{\mathbf{R}_I\})$ denotes the total energy of many-electron system, which is also \mathbf{R}_I -dependent because electron wavefunction indirectly depends on nuclei positions. The U_{nn1} , U_{nn2} , and U_{nn3} in Eq. 3.7 are derived as

$$\begin{aligned}
U_{nn1} &= - \sum_I^{Nn} \frac{\nabla_I^2}{2M_I} \\
U_{nn2} &= - \sum_I^{Nn} \frac{1}{M_I} \int \Psi(\{\mathbf{r}_i\}; \{\mathbf{R}_I\})^* \nabla_I \Psi(\{\mathbf{r}_i\}; \{\mathbf{R}_I\}) d\mathbf{r} \nabla_I \\
U_{nn3} &= - \sum_I^{Nn} \frac{1}{M_I} \int \Psi(\{\mathbf{r}_i\}; \{\mathbf{R}_I\})^* \nabla_I^2 \Psi(\{\mathbf{r}_i\}; \{\mathbf{R}_I\}) d\mathbf{r}.
\end{aligned} \tag{3.8}$$

In Eq. 3.7, one observes that the lattice dynamical properties of certain system within the Born-Oppenheimer approximation can be obtained. To solve this equation, the ground state energy $E(\{\mathbf{R}_I\})$ of many-electron system is needed. Here, $\{\mathbf{R}_I\}$ denotes a set of atom positions.

In summary, the Schrödinger equations of electrons and nuclei are derived separately within the Born-Oppenheimer approximation. When one calculates ground state properties, the Schrödinger equation of the electrons is applied (the first line in Eq. 3.7). The Schrödinger equation of nuclei is employed for the calculations of lattice dynamics (U_{nn2} and U_{nn3} are ignored [88] in the second line in Eq. 3.7 normally).

The Eq. 3.7 (the first line) is much simpler than Eq. 3.1. However, it is still not solvable. Further approximations are needed to solve this many-body problem.

3.3 Solving the many-body problem

In previous section, the separation of wavefunction is proposed within Born-Oppenheimer approximation. The quantum many-body Schrödinger problem becomes the many-electron Schrödinger problem. There are two major problems from the Born-Oppenheimer approximation: the first problem is that the number of electron is around in the order of 10^{24} cm^{-3} in most of the cases, which is a huge numerical problem. However, it is still possible to solve; the second one is that the Hamiltonian includes operators acting on the single electron. However, how the relation between the wavefunction and the single-electron wavefunction is unknown. The latter problem can be solved by one of the following three methods: the first method is to figure out a way to separate or approximate the wavefunction from the single-electron function, such as the Hartree and Hartree-Fock (HF) methods [84, 85]; the second method is to find an explicit relation between total energy and wavefunction, such as density functional theory (DFT) [86]. Within DFT, the system total energy is a functional of electron density. Either of these two methods has "pros and cons"; the third one is called Kohn-Sham equation [87], which is a combination of above two methods. It starts from DFT, and takes advantage of single-electron wavefunction.

3.3.1 Hartree approximation

The simplest approximation of wavefunction for many-electron Schrödinger equation is the one acting like independent electrons. The wavefunction with N_e independent electrons is defined as

$$\Psi^H(\{\mathbf{r}_i\}) = \phi_1(\mathbf{r}_1)\phi_2(\mathbf{r}_2) \cdots \phi_{N_e}(\mathbf{r}_{N_e}). \quad (3.9)$$

Here, $\phi_i(\mathbf{r}_i)$ implies state of the i :th electron, where different states of electrons are orthonormalized. From here on, the $\{\mathbf{R}_I\}$ are suppressed in the wavefunction since atoms are treated as in fixed positions. The set of variables $\{\mathbf{r}_i\}$ includes the coordinates of space and spin. The total energy of the many-electron system can be written as

$$E^H = \langle \Psi^H(\{\mathbf{r}_i\}) | H | \Psi^H(\{\mathbf{r}_i\}) \rangle . \quad (3.10)$$

H in Eq. 3.4 can be rewritten as

$$\begin{aligned} H &= \sum_i^{Ne} \left(-\frac{\nabla_i^2}{2} - \sum_I^{Nn} \frac{Z_I}{|\mathbf{r}_i - \mathbf{R}_I|} \right) + \frac{1}{2} \sum_i^{Ne} \sum_{j \neq i}^{Ne} \frac{1}{|\mathbf{r}_i - \mathbf{r}_j|} \\ &= \sum_i^{Ne} h_1(\mathbf{r}_i) + \frac{1}{2} \sum_i^{Ne} \sum_{j \neq i}^{Ne} h_2(\mathbf{r}_i, \mathbf{r}_j). \end{aligned} \quad (3.11)$$

Therefore, the system total energy is given as

$$\begin{aligned} E^H &= \sum_i^{Ne} \langle \phi_i(\mathbf{r}_i) | h_1(\mathbf{r}_i) | \phi_i(\mathbf{r}_i) \rangle \\ &\quad + \frac{1}{2} \sum_i^{Ne} \sum_{j \neq i}^{Ne} \langle \phi_i(\mathbf{r}_i) \phi_j(\mathbf{r}_j) | h_2(\mathbf{r}_i, \mathbf{r}_j) | \phi_i(\mathbf{r}_i) \phi_j(\mathbf{r}_j) \rangle . \end{aligned} \quad (3.12)$$

In order to calculate the stationary state with the lowest energy of the system, one method called Lagrange multipliers can be utilized. Furthermore, the constraint is that the different states of electrons are orthonormalized. Therefore, the variation with respect to any wavefunction $\phi_k^*(\mathbf{r})$ and Lagrange multiplier $E_{i,j}^H$ are satisfied [88,89]

$$\frac{\delta \left(E^H - \sum_i^{Ne} \sum_j^{Ne} E_{i,j}^H (\langle \phi_i(\mathbf{r}_i) | \phi_j(\mathbf{r}_j) \rangle - \delta_{ij}) \right)}{\delta \phi_k^*(\mathbf{r})} = 0. \quad (3.13)$$

Here, $\delta \phi_k(\mathbf{r})$ also can be utilized. However, variation with respect to $\phi_k^*(\mathbf{r})$ and $\phi_k(\mathbf{r})$ are equivalent. It is convenient to use $\delta \phi_k^*(\mathbf{r})$.

δE^H in Eq. 3.13 can be calculated by two parts. The first part is

$$\begin{aligned} &\delta \left(\sum_i^{Ne} \langle \phi_i(\mathbf{r}_i) | h_1(\mathbf{r}_i) | \phi_i(\mathbf{r}_i) \rangle \right) \\ &= \langle \delta \phi_k(\mathbf{r}) | h_1(\mathbf{r}) | \phi_k(\mathbf{r}) \rangle + \langle \phi_k(\mathbf{r}) | h_1(\mathbf{r}) | \delta \phi_k(\mathbf{r}) \rangle . \end{aligned} \quad (3.14)$$

The second part is

$$\begin{aligned}
& \frac{1}{2} \delta \sum_i^{Ne} \sum_{j \neq i}^{Ne} \langle \phi_i(\mathbf{r}_i) \phi_j(\mathbf{r}_j) | h_2(\mathbf{r}_i, \mathbf{r}_j) | \phi_i(\mathbf{r}_i) \phi_j(\mathbf{r}_j) \rangle \\
&= \frac{1}{2} \sum_{i \neq k}^{Ne} \left(\langle \phi_i(\mathbf{r}_i) \delta \phi_k(\mathbf{r}) | h_2(\mathbf{r}_i, \mathbf{r}) | \phi_i(\mathbf{r}_i) \phi_k(\mathbf{r}) \rangle \right. \\
&\quad \left. + \langle \phi_i(\mathbf{r}_i) \phi_k(\mathbf{r}) | h_2(\mathbf{r}_i, \mathbf{r}) | \phi_i(\mathbf{r}_i) \delta \phi_k(\mathbf{r}) \rangle \right) \\
&\quad + \frac{1}{2} \sum_{j \neq k}^{Ne} \left(\langle \delta \phi_k(\mathbf{r}) \delta \phi_j(\mathbf{r}_j) | h_2(\mathbf{r}, \mathbf{r}_j) | \phi_k(\mathbf{r}) \phi_j(\mathbf{r}_j) \rangle \right. \\
&\quad \left. + \langle \phi_k(\mathbf{r}) \phi_j(\mathbf{r}_j) | h_2(\mathbf{r}, \mathbf{r}_j) | \delta \phi_k(\mathbf{r}) \phi_j(\mathbf{r}_j) \rangle \right) \\
&= \sum_{i \neq k}^{Ne} \left(\langle \phi_i(\mathbf{r}_i) \delta \phi_k(\mathbf{r}) | h_2(\mathbf{r}_i, \mathbf{r}) | \phi_i(\mathbf{r}_i) \phi_k(\mathbf{r}) \rangle \right. \\
&\quad \left. + \langle \phi_i(\mathbf{r}_i) \phi_k(\mathbf{r}) | h_2(\mathbf{r}_i, \mathbf{r}) | \phi_i(\mathbf{r}_i) \delta \phi_k(\mathbf{r}) \rangle \right). \tag{3.15}
\end{aligned}$$

Here, the factor of $\frac{1}{2}$ is canceled because the 2nd (3rd) line is the same with 4th (5th) line in Eq. 3.15 due to the exchangeable indices of i and j .

To get the final solution, one more calculation is needed

$$\begin{aligned}
& \delta \sum_i^{Ne} \sum_j^{Ne} E_{i,j}^H \left(\langle \phi_i(\mathbf{r}_i) | \phi_j(\mathbf{r}_j) \rangle - \delta_{i,j} \right) \\
&= \sum_j^{Ne} E_{k,j}^H \left(\langle \delta \phi_k(\mathbf{r}) | \phi_j(\mathbf{r}_j) \rangle \right) + \sum_i^{Ne} E_{i,k}^H \left(\langle \phi_i(\mathbf{r}_i) | \delta \phi_k(\mathbf{r}) \rangle \right) \\
&= \sum_i^{Ne} E_{k,i}^H \left(\langle \delta \phi_k(\mathbf{r}) | \phi_i(\mathbf{r}_i) \rangle + \langle \phi_i(\mathbf{r}_i) | \delta \phi_k(\mathbf{r}) \rangle \right). \tag{3.16}
\end{aligned}$$

Therefore, Eq. 3.13 can be derived as

$$\left(-\frac{\nabla_k^2}{2} + \sum_I^{Nn} \frac{Z_I}{|\mathbf{r} - \mathbf{R}_I|} + \sum_{j \neq k}^{Ne} \langle \phi_j(\mathbf{r}') | \frac{1}{|\mathbf{r} - \mathbf{r}'|} | \phi_j(\mathbf{r}') \rangle \right) \phi_k(\mathbf{r}) = \sum_i^{Ne} E_{k,i}^H \phi_i(\mathbf{r}). \tag{3.17}$$

There are many solutions in Eq. 3.17, and each corresponds to a different set of $E_{k,i}^H$. One can choose to the $E_{k,i}^H$, which satisfies $E_{k,i}^H = \delta_{k,i} \epsilon_k^H$. Eq. 3.17 can be rewritten as

$$\begin{aligned} \left(-\frac{\nabla_k^2}{2} + \sum_I^{Nn} \frac{Z_I}{|\mathbf{r} - \mathbf{R}_I|} + \sum_{j \neq k}^{Ne} \langle \phi_j(\mathbf{r}') | \frac{1}{|\mathbf{r} - \mathbf{r}'|} |\phi_j(\mathbf{r}') \rangle \right) \phi_k(\mathbf{r}) &= \epsilon_k^H \phi_k(\mathbf{r}) \\ &\Downarrow \\ \left(-\frac{\nabla_i^2}{2} + \sum_I^{Nn} \frac{Z_I}{|\mathbf{r} - \mathbf{R}_I|} + \sum_{j \neq i}^{Ne} \langle \phi_j(\mathbf{r}') | \frac{1}{|\mathbf{r} - \mathbf{r}'|} |\phi_j(\mathbf{r}') \rangle \right) \phi_i(\mathbf{r}) &= \epsilon_i^H \phi_i(\mathbf{r}). \end{aligned} \quad (3.18)$$

Here, **Eq. 3.18** is a group of dependent single particle equations. ϵ_k^H is identified as the eigenvalue for this single-electron Hartree equation.

3.3.2 Hartree-Fock approximation

Hartree approximation is a simple approximation. Hartree-Fock (HF) approximation is a method which considers antisymmetry of wavefunction. It is shown as

$$\Psi^{HF}(\dots \mathbf{r}_i \dots \mathbf{r}_j \dots) = -\Psi^{HF}(\dots \mathbf{r}_j \dots \mathbf{r}_i \dots). \quad (3.19)$$

Here, each variable \mathbf{r}_i includes the coordinates of space and spin. Slater introduced a way to construct the wavefunction subject to **Eq. 3.19** [90]. The wavefunction of the many-electron Schrödinger equation is described in a matrix determinant for the N number of electrons (for aesthetic reason, N implies the number of electrons and not Ne as in previous sections)

$$\Psi^{HF}(\mathbf{r}_1, \mathbf{r}_2, \dots, \mathbf{r}_N) = \frac{1}{\sqrt{N!}} \begin{vmatrix} \phi_1(\mathbf{r}_1) & \phi_2(\mathbf{r}_1) & \cdots & \phi_N(\mathbf{r}_1) \\ \phi_1(\mathbf{r}_2) & \phi_2(\mathbf{r}_2) & \cdots & \phi_N(\mathbf{r}_2) \\ \vdots & \vdots & & \vdots \\ \phi_1(\mathbf{r}_N) & \phi_2(\mathbf{r}_N) & \cdots & \phi_N(\mathbf{r}_N) \end{vmatrix}. \quad (3.20)$$

Here, the factor in front ensures normalization, and $\phi_i(\mathbf{r}_i)$ implies state of the (i):th electron. **Eq. 3.20** has the antisymmetry property of wavefunction.

The total energy of Hartree-Fock approximation, which can be determined similarly as in the previous section of Hartree approximation, is given as

$$\begin{aligned}
E^{HF} = & \sum_i^N \langle \phi_i(\mathbf{r}) | -\frac{\nabla_i^2}{2} + \sum_I^{Nn} \frac{Z_I}{|\mathbf{r} - \mathbf{R}_I|} |\phi_i(\mathbf{r}) \rangle \\
& + \frac{1}{2} \sum_i^N \sum_j^N \langle \phi_i(\mathbf{r}) \phi_j(\mathbf{r}') | \frac{1}{|\mathbf{r} - \mathbf{r}'|} |\phi_i(\mathbf{r}) \phi_j(\mathbf{r}') \rangle \\
& - \frac{1}{2} \sum_i^N \sum_j^N \langle \phi_i(\mathbf{r}') \phi_j(\mathbf{r}) | \frac{1}{|\mathbf{r} - \mathbf{r}'|} |\phi_i(\mathbf{r}) \phi_j(\mathbf{r}') \rangle.
\end{aligned} \tag{3.21}$$

Here, there is no contribution to the sum when $i = j$. In the same mathematical way as in previous section but somewhat more complicated, the single particle Hartree-Fock equation can be obtained

$$\begin{aligned}
& \left(-\frac{\nabla_i^2}{2} + \sum_I^{Nn} \frac{Z_I}{|\mathbf{r} - \mathbf{R}_I|} + \sum_j^N \langle \phi_j(\mathbf{r}') | \frac{1}{|\mathbf{r} - \mathbf{r}'|} |\phi_j(\mathbf{r}') \rangle \right) \phi_i(\mathbf{r}) \\
& - \sum_j^N \langle \phi_j(\mathbf{r}') | \frac{1}{|\mathbf{r} - \mathbf{r}'|} |\phi_i(\mathbf{r}') \rangle \phi_j(\mathbf{r}) = \epsilon_i^{HF} \phi_i(\mathbf{r}).
\end{aligned} \tag{3.22}$$

In comparison with Hartree equation in Eq. 3.18, there is an extra term in Eq. 3.22, which is so called exchange term. In order to show the equation in a more well organized way, Eq. 3.22 is equivalent to

$$\begin{aligned}
& \left(-\frac{\nabla_i^2}{2} + \sum_I^{Nn} \frac{Z_I}{|\mathbf{r} - \mathbf{R}_I|} + V_{HF}(\mathbf{r}) \right) \phi_i(\mathbf{r}) = \epsilon_i^{HF} \phi_i(\mathbf{r}) \\
V^{HF}(\mathbf{r}) = & \int \frac{\rho(\mathbf{r}') - \rho_i^{HF}(\mathbf{r}, \mathbf{r}')}{|\mathbf{r} - \mathbf{r}'|} d\mathbf{r}' \\
\rho_i^{HF}(\mathbf{r}, \mathbf{r}') = & \sum_j^N \frac{\phi_i(\mathbf{r}') \phi_i^*(\mathbf{r}) \phi_j(\mathbf{r}) \phi_j^*(\mathbf{r}')}{\phi_i(\mathbf{r}) \phi_i^*(\mathbf{r})} \\
\rho(\mathbf{r}) = & \sum_i^N |\phi_i(\mathbf{r})|^2.
\end{aligned} \tag{3.23}$$

3.3.3 Density functional theory

The Hartree and HF methods are very classic methods solving the many-electron Schrödinger equation. However, the HF method only includes the exchange term and not the electron correlation term. Therefore, it is not suitable for solid materials. Apart from the

Hartree and HF methods, there is a modern method solving the more complicated calculations of many-electron system, namely density functional theory (DFT). It is introduced by Hohenberg and Kohn in 1964 [86]. Kohn and Pople were awarded Chemistry Nobel Prize in 1998.

The idea of the DFT is to treat the electron density in solid materials instead of using the many-particle wavefunction. In this case, the degree of freedom reduces from $3N$ (N is the number of electrons) to 3. It is apparently less complicated than Hartree and HF methods.

The density as basic variable

There are two questions coming out if considering the electron density as a role of wavefunction. The first one is whether it is the equivalence relation between electron density and wavefunction in many-electron system. The second one is how to solve the problem if considering the electron density instead of the wavefunction. In order to explain above two questions, there are two very basic theorems introduced by Hohenberg and Kohn:

Theorem 1 *The first theorem states that the external potential $V_{ext}(\mathbf{r})$ is determined uniquely for any many-electron system by the ground-state electron density ρ .*

The above theorem indicates that all ground state properties are determined by the true ground-state density ρ as well, such as, the total energy $E = E[\rho]$.

The above theorem also explains the equivalence relation between the electron density and wavefunction. Hamiltonian is obtained from external potential, thus the wavefunction is obtained from the external potential. Therefore, the corresponding electron density is determined. Moreover, the external potential is unique decided by electron density from the theorem. Therefore, the electron density contains the same information as the wavefunction.

Proof of the theorem is given. Let us assume that there exists two external potentials named $V_{ext}(\mathbf{r})$ and $V'_{ext}(\mathbf{r})$ leading to the same ground state electron density ρ . Obviously, this will lead to two different Hamiltonians, that is, H and H' , as well as two different corresponding wavefunctions named Ψ and Ψ' . Since Ψ is not the ground state wavefunction of H' , the same rules to Ψ' and H , two following inequality equations are satisfied

$$\begin{aligned} E &= \langle \Psi | H | \Psi \rangle < \langle \Psi' | H | \Psi' \rangle \\ E' &= \langle \Psi' | H' | \Psi' \rangle < \langle \Psi | H' | \Psi \rangle. \end{aligned} \tag{3.24}$$

Taking advantage of the Hamiltonian from **Eq. 3.4**, the following equation is derived

$$\begin{aligned}
 & \langle \Psi' | H | \Psi' \rangle \\
 &= \langle \Psi' | H' + H - H' | \Psi' \rangle \\
 &= \langle \Psi' | H' | \Psi' \rangle + \langle \Psi' | H - H' | \Psi' \rangle \\
 &= E' + \int \left(V_{ext}(\mathbf{r}) - V'_{ext}(\mathbf{r}) \right) \rho(\mathbf{r}) d\mathbf{r}.
 \end{aligned} \tag{3.25}$$

Using **Eq. 3.24** and **Eq. 3.25**, the following relation is given by

$$E < E' + \int \left(V_{ext}(\mathbf{r}) - V'_{ext}(\mathbf{r}) \right) \rho(\mathbf{r}) d\mathbf{r}. \tag{3.26}$$

Another similar inequality equation can be obtained if one changes the equation $\langle \Psi | H' | \Psi \rangle$ like **Eq. 3.25**

$$E' < E + \int \left(V'_{ext}(\mathbf{r}) - V_{ext}(\mathbf{r}) \right) \rho(\mathbf{r}) d\mathbf{r}. \tag{3.27}$$

Plus the left side and right side from both **Eq. 3.26** and **Eq. 3.27**, a contradictory result is given as

$$E + E' < E' + E. \tag{3.28}$$

Since this is an incorrect relation, the external potential $V_{ext}(\mathbf{r})$ has to be unique.

Theorem 2 *The second theorem states that there is a universal functional $F[\rho]$ for the total energy in the terms of the electron density ρ with any external potential $V_{ext}(\mathbf{r})$, and the exact ground-state density is obtained when the ground state total energy functional reaches its minimal value, that is, $E[\rho'] > E[\rho]$. Here, ρ is the exact ground-state density.*

Proof of theorem is given. Because of the first theorem, the kinetic and interaction energies are functional of electron density. The total energy can be expressed in the following way (ignoring the interaction between nuclei)

$$\begin{aligned}
 E[\rho] &= \langle \Psi | U_e + U_{int} + U_{ext} | \Psi \rangle \\
 &= \langle \Psi | V_{ext}(\mathbf{r}) | \Psi \rangle + \underbrace{\langle \Psi | U_e + U_{int} | \Psi \rangle}_{\int \rho(\mathbf{r}) V_{ext}(\mathbf{r}) d\mathbf{r}} \\
 &= \int \rho(\mathbf{r}) V_{ext}(\mathbf{r}) d\mathbf{r} + F[\rho].
 \end{aligned} \tag{3.29}$$

In **Eq. 3.29**, the term of $F[\rho]$ is a universal functional for all the many-electron system.

The functional of total energy $E[\rho']$ reaches the minimum at the exact ground-state electron density ρ

$$E[\rho'] = \int \rho'(\mathbf{r}) V_{ext}(\mathbf{r}) d\mathbf{r} + F[\rho'] > E[\rho]. \tag{3.30}$$

Here, the total energy for the case of exact ground-state electron density is lower than any other cases. Therefore, the exact ground-state electron density by minimizing the total energy can be achieved.

From those two theorems, one knows how to solve Schrödinger equation theoretically. However, $E[\rho]$ is unknown in practice. Therefore, another method is needed to solve this problem, which is so called Kohn-Sham (KS) equation.

3.3.4 Kohn-Sham equation

The Hartree and HF methods are introduced to solve the many-body problem, both of which are based on the idea of transforming complex many-electron problem to single-electron problem by using different wavefunctions. The DFT gives the answer to solve many-electron system, however, it does not give explicit expression. This problem in DFT is solved by KS equation, which was introduced by Kohn and Sham in 1965 [87]. It is demonstrated in the following text (ignoring the interaction between nuclei).

Assume that the exact ground-state density is obtained by the Hartree-like wavefunction $\Psi^{KS}(\{\mathbf{r}_i\}) = \Psi_1^{KS}(\mathbf{r}_1)\Psi_2^{KS}(\mathbf{r}_2)\cdots\Psi_N^{KS}(\mathbf{r}_N)$. Here, N is the number of electrons, and $\Psi_i^{KS}(\mathbf{r}_i)$ is an auxiliary independent single-electron wavefunction. The electron density is defined as

$$\rho(\mathbf{r}) = \sum_i^N \Psi_i^{KS*}(\mathbf{r})\Psi_i^{KS}(\mathbf{r}). \quad (3.31)$$

If the electron density is exact, thus the total energy is exact. It is given as

$$\begin{aligned} E[\rho] &= T[\rho] + V_{int}[\rho] + V_{ext}[\rho] \\ &= T_0[\rho] + V_H[\rho] + V_{ext}[\rho] + \underbrace{(T[\rho] - T_0[\rho])}_{(V_{int}[\rho] - V_H[\rho])} \\ &= T_0[\rho] + V_H[\rho] + V_{ext}[\rho] + E_{xc}[\rho]. \end{aligned} \quad (3.32)$$

Here, $E[\rho]$ denotes total energy, and ρ denotes ground-state density. $T[\rho]$, $V_{int}[\rho]$, and $V_{ext}[\rho]$ represent energies from the exact kinetic, the exact electron-electron potential, and external potential in sequence. $E_{xc}[\rho]$ is unknown exchange-correlation energy.

The $T_0[\rho]$, $V_H[\rho]$, and $V_{ext}[\rho]$ represent kinetic energy in the Hartree approximation, electron interaction energy in Hartree approximation, and electron-nuclei interaction energy in sequence.

$$\begin{aligned}
T_0[\rho] &= \sum_i^N \langle \Psi_i^{KS}(\mathbf{r}) | -\frac{\nabla^2}{2} | \Psi_i^{KS}(\mathbf{r}) \rangle \\
V_H[\rho] &= \frac{1}{2} \int \int \frac{\rho(\mathbf{r})\rho(\mathbf{r}')}{|\mathbf{r} - \mathbf{r}'|} d\mathbf{r}d\mathbf{r}' \\
V_{ext}[\rho] &= \int \rho(\mathbf{r}) V_{ext}(\mathbf{r}) d\mathbf{r}.
\end{aligned} \tag{3.33}$$

In order to derive the ground state properties in the many-electron system, one can view this problem as the process of minimizing the total energy by varying the wavefunction $\Psi_k^{KS*}(\mathbf{r})$.

$$\begin{aligned}
&\frac{\delta \left(E[\rho] - \sum_i^{Ne} \sum_j^{Ne} E_{i,j}^H (\langle \Psi_i^{KS}(\mathbf{r}_i) | \Psi_j^{KS}(\mathbf{r}_j) \rangle - \delta_{ij}) \right)}{\delta \Psi_k^{KS*}(\mathbf{r})} = 0 \\
&\downarrow \\
&\frac{\delta T_0[\rho]}{\Psi_k^{KS*}(\mathbf{r})} + \frac{\delta(V_H[\rho] + V_{ext}[\rho] + E_{xc}[\rho])}{\delta \rho(\mathbf{r})} \frac{\delta \rho(\mathbf{r})}{\Psi_k^{KS*}(\mathbf{r})} = \sum_i^N E_{k,i}^{KS} \Psi_i^{KS}(\mathbf{r}).
\end{aligned} \tag{3.34}$$

The derivation is similar as in the section of Hartree approximation, the KS equation is derived as

$$\left(-\frac{\nabla^2}{2} + V^{KS}(\mathbf{r}) \right) \Psi_i^{KS}(\mathbf{r}) = \epsilon_i^{KS} \Psi_i^{KS}(\mathbf{r}). \tag{3.35}$$

Here, ϵ_i^{KS} is identified as eigenvalue for the KS equation. The $V^{KS}(\mathbf{r})$ is give as

$$\begin{aligned}
V^{KS}(\mathbf{r}) &= V_{ext}(\mathbf{r}) + \int d\mathbf{r}' \frac{\rho(\mathbf{r}')}{|\mathbf{r} - \mathbf{r}'|} + \frac{\delta E_{xc}}{\delta \rho(\mathbf{r})} \\
&= V_{ext}(\mathbf{r}) + \int d\mathbf{r}' \frac{\rho(\mathbf{r}')}{|\mathbf{r} - \mathbf{r}'|} + V_{xc}(\mathbf{r}).
\end{aligned} \tag{3.36}$$

In \mathbf{k} -space, KS equation in Eq. 3.35 can be written as

$$\left(-\frac{\nabla^2}{2} + V^{KS}(\mathbf{r}) \right) \Psi_{i,k}^{KS}(\mathbf{r}) = \epsilon_{i,k}^{KS} \Psi_{i,k}^{KS}(\mathbf{r}). \tag{3.37}$$

The total energy is not given in Eq. 3.35. However, if one changes Eq. 3.35 as

$$\sum_i^N \Psi_i^{KS*}(\mathbf{r}) \left(-\frac{\nabla^2}{2} + V^{KS}(\mathbf{r}) \right) \Psi_i^{KS}(\mathbf{r}) = \sum_i^N \Psi_i^{KS*}(\mathbf{r}) \epsilon_i^{KS} \Psi_i^{KS}(\mathbf{r}). \tag{3.38}$$

Based on Eq. 3.33 , Eq. 3.32, and Eq. 3.38, the total energy expression is derived as

$$\begin{aligned} E[\rho] = & \sum_i^N \epsilon_i^{KS} - \frac{1}{2} \int \int d\mathbf{r} d\mathbf{r}' \frac{\rho(\mathbf{r})\rho(\mathbf{r}')}{|\mathbf{r} - \mathbf{r}'|} \\ & + E_{xc}[\rho] - \int V_{xc}(\mathbf{r})\rho(\mathbf{r})d\mathbf{r}. \end{aligned} \quad (3.39)$$

There are two problems still in the air: one is the exact format of $V_{xc}(\mathbf{r})$; the other one is how to solve the KS equation.

3.3.5 The exchange-correlation potential

The exchange-correlation potential is the most difficult part during the process of solving the KS equation, because the exact form is still unknown today. Therefore, there are varies of approximations about it, such as the local density approximation (LDA) [81, 82, 87, 91, 92].

The local density approximation

The LDA is a simple way to approximate the exchange-correlation part. It is based on free electron gas, which has a constant electron density

$$\rho(\mathbf{r}) = \rho = \frac{N}{V}. \quad (3.40)$$

Here, N is number of electrons within solid, and V is volume of solid. The exact exchange-correlation energy per electron is given as

$$\varepsilon_{xc}^{gas}(\rho) = -\frac{3}{4} \cdot \left(\frac{3}{\pi}\right)^{1/3} \cdot \rho^{1/3} + \begin{cases} A \ln r_s + B + C r_s \ln r_s + D r_s & \text{if } r_s \leq 1 \\ \gamma/(1 + \beta_1 \sqrt{r_s} + \beta_2 r_s) & \text{if } r_s > 1. \end{cases} \quad (3.41)$$

Here, $r_s = (3/(4\pi\rho))^{1/3}$. In the LDA, the idea is that the exchange-correlation energy for an electron in a very tiny small volume in many-particle system is equal to the exchange-correlation for an electron in the free electron gas with the same density in the volume ($\varepsilon_{xc}^{gas}(\rho(\mathbf{r})) = \varepsilon_{xc}^{gas}(\mathbf{r})$). The explicit exchange-correlation energy is given as

$$E_{xc}^{LDA}[\rho] = \int \rho(\mathbf{r}) \varepsilon_{xc}^{gas}(\mathbf{r}) d\mathbf{r}. \quad (3.42)$$

Therefore, the exchange-correlation potential is give as

$$V_{xc}^{LDA}(\mathbf{r}) = \frac{\delta E_{xc}^{LDA}[\rho]}{\delta \rho}. \quad (3.43)$$

Today, there exists hundreds of different exchange-correlation potentials [93–96]. It is still ongoing development. The advantage of KS equation is that new potentials are implemented easily. In the same time, it has many potentials due to the simplicity of implementation.

3.4 Solving the secular equation

The process for solving KS equation can be achieved by iteration [81, 82, 88]. Potential in KS equation depends on electron density. However, electron density is calculated by wavefunction, which depends on the potential. An initial guess of electron density is calculated at the beginning of calculation, then the KS equation is solved iteratively until a reasonable solution is obtained.

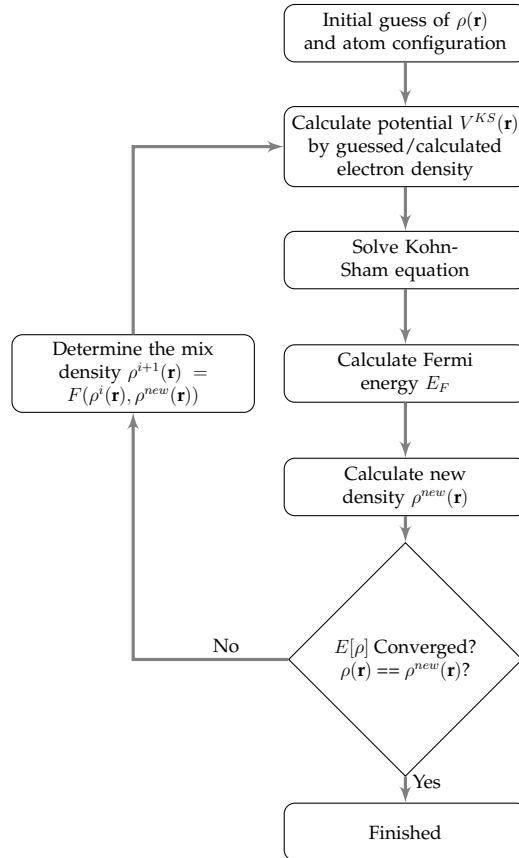


Figure 3.1. Flow chart of the $(i + 1)$:th iteration for solving KS equation.

Here, $\rho^i(\mathbf{r})$ and $\rho^{i+1}(\mathbf{r})$ are the electron densities in the i :th iteration and $(i+1)$:th iteration during solving Kohn-Sham equation, respectively.

In order to solve **Eq. 3.35**, the KS equation can be transformed into the general eigenvalue problem [81, 82]. If the KS equation is given as (the index i is ignored in wavefunction in comparison with **Eq. 3.35**)

$$H^{KS}\Psi^{KS}(\mathbf{r}) = \epsilon^{KS}\Psi^{KS}(\mathbf{r}). \quad (3.44)$$

The wavefunction is defined as

$$\Psi^{KS}(\mathbf{r}) = \sum_j^N C_j \phi_j(\mathbf{r}). \quad (3.45)$$

Here, C_j is a complex number, and $\phi_j(\mathbf{r})$ is basis function of wavefunction.

If **Eq. 3.45** is plugged into **Eq. 3.44**, and $\phi_1^*, \phi_2^*, \dots, \phi_N^*$ are multiplied on the left side of **Eq. 3.44** in sequence, the new equation is

$$\begin{aligned} & \begin{bmatrix} \phi_1^* H \phi_1 & \phi_1^* H \phi_2 & \cdots & \phi_1^* H \phi_N \\ \phi_2^* H \phi_1 & \phi_2^* H \phi_2 & \cdots & \phi_2^* H \phi_N \\ \vdots & \vdots & & \vdots \\ \phi_N^* H \phi_1 & \phi_N^* H \phi_2 & \cdots & \phi_N^* H \phi_N \end{bmatrix} \begin{bmatrix} C_1 \\ C_2 \\ \vdots \\ C_N \end{bmatrix} \\ &= \epsilon^{KS} \begin{bmatrix} \phi_1^* \phi_1 & \phi_1^* \phi_2 & \cdots & \phi_1^* \phi_N \\ \phi_2^* \phi_1 & \phi_2^* \phi_2 & \cdots & \phi_2^* \phi_N \\ \vdots & \vdots & & \vdots \\ \phi_N^* \phi_1 & \phi_N^* \phi_2 & \cdots & \phi_N^* \phi_N \end{bmatrix} \begin{bmatrix} C_1 \\ C_2 \\ \vdots \\ C_N \end{bmatrix}. \end{aligned} \quad (3.46)$$

Eq. 3.46 becomes

$$\begin{aligned} & \begin{bmatrix} H_{11} & H_{12} & \cdots & H_{1N} \\ H_{21} & H_{22} & \cdots & H_{2N} \\ \vdots & \vdots & & \vdots \\ H_{N1} & H_{N2} & \cdots & H_{NN} \end{bmatrix} \begin{bmatrix} C_1 \\ C_2 \\ \vdots \\ C_N \end{bmatrix} \\ &= \epsilon^{KS} \begin{bmatrix} S_{11} & S_{12} & \cdots & S_{1N} \\ S_{21} & S_{22} & \cdots & S_{2N} \\ \vdots & \vdots & & \vdots \\ S_{N1} & S_{N2} & \cdots & S_{NN} \end{bmatrix} \begin{bmatrix} C_1 \\ C_2 \\ \vdots \\ C_N \end{bmatrix}. \end{aligned} \quad (3.47)$$

Here, $H_{ij} = \phi_i^* H \phi_j$ and $S_{ij} = \phi_i^* \phi_j$.

There are left part and right part in **Eq. 3.47**. If the right part moves to the left part. The **Eq. 3.47** is derived as

$$\begin{bmatrix} H_{11} - \epsilon^{KS} S_{11} & H_{12} - \epsilon^{KS} S_{12} & \cdots & H_{1N} - \epsilon^{KS} S_{1N} \\ H_{21} - \epsilon^{KS} S_{21} & H_{22} - \epsilon^{KS} S_{22} & \cdots & H_{2N} - \epsilon^{KS} S_{2N} \\ \vdots & \vdots & & \vdots \\ H_{N1} - \epsilon^{KS} S_{N1} & H_{N2} - \epsilon^{KS} S_{N2} & \cdots & H_{NN} - \epsilon^{KS} S_{NN} \end{bmatrix} \begin{bmatrix} C_1 \\ C_2 \\ \vdots \\ C_N \end{bmatrix} = \begin{bmatrix} 0 \\ 0 \\ \vdots \\ 0 \end{bmatrix}. \quad (3.48)$$

Apparently, Eq. 3.48 is an eigenvalue problem. In order to get the C_i ($i = 1 \dots N$), one needs to solve the following equation

$$\begin{vmatrix} H_{11} - \epsilon^{KS} S_{11} & H_{12} - \epsilon^{KS} S_{12} & \cdots & H_{1N} - \epsilon^{KS} S_{1N} \\ H_{21} - \epsilon^{KS} S_{21} & H_{22} - \epsilon^{KS} S_{22} & \cdots & H_{2N} - \epsilon^{KS} S_{2N} \\ \vdots & \vdots & & \vdots \\ H_{N1} - \epsilon^{KS} S_{N1} & H_{N2} - \epsilon^{KS} S_{N2} & \cdots & H_{NN} - \epsilon^{KS} S_{NN} \end{vmatrix} = 0. \quad (3.49)$$

3.5 Full-potential linearized augmented plane wave method

3.5.1 Introduction

One knows how to solve the KS equation from previous sections. However, there are still two more questions, what is the exact form of wavefunction and potential in realistic calculations?

One maybe naturally choose a set of plane waves as the wavefunction because of Bloch theory [97]. There is a drawback about the plane waves as wavefunction. The wavefunction changes dramatically in the atomic core region, therefore, one needs to choose more plane waves to approximate it. It implies that calculations are time-consuming.

Slater re-considered the way to describe the wavefunction (Eq. 3.51). Unit cell is divided into two regions [98, 99]: one is sphere region called muffin tin (MT) region, which is defined by the center of atom, but non-overlap each sphere; the remaining region is called interstitial (I) region (Fig. 3.2). An atomic-like function is defined in the MT region, this is reason why this method is called augmented plane wave (APW). The dual representation of the wavefunction is reasonable, because the wavefunction approaching atomic core is somehow like inside atom. However, the electrons behave like free electrons far away the atomic core. Therefore, plane waves are suitable to describe wavefunction in I region (Eq. 3.51). The drawback of APW method is that the wavefunction is energy-dependent, which leads to a nonlinear eigenvalue problem (Eq. 3.52). To achieve the exact energy, energy has to be decided repeatedly until certain condition is satisfied, which is time-consuming.

In order to solve the problem in APW, Andesen [100], Koelling and Arbman [101] proposed a way to describe the energy-independent wavefunction. They noticed that the Taylor expansion of radial function (Eq. 3.55). This method is called linearized augmented plane wave (LAPW) method due to make use of the linearized energies in the radial functions. However, the drawback is that it does not describe the semi-core states well. It is corrected by a method named linearized augmented plane wave plus local orbitals (LAPW+LO) which was proposed by Singh (Eq. 3.57) [102]. Sjöstedt, Nordström and Singh [103] also gave an efficient way to linearize Slater's APW method, named augmented plane wave plus local orbitals (APW+lo) (Eq. 3.58). Both of above methods consider local orbitals, it is customary to write in different ways as LO and lo, respectively. LAPW method with the potential defined in Eq. 3.5.3 is called as full-potential linearized augmented plane wave (FPLAPW) method, because there is no shape approximations to the crystal potential. One can read more information about FPLAPW method in Refs. [104, 105].

3.5.2 Wavefunction

Augmented plane wave method

The KS wavefunction can be expanded by a set of basis functions

$$\Psi_{i,\mathbf{k}}^{KS}(\mathbf{r}) = \sum_{\mathbf{G}}^{N_G} C_{i,\mathbf{k}+\mathbf{G}} \phi_{\mathbf{k}+\mathbf{G}}(\mathbf{r}). \quad (3.50)$$

Here, $\phi_{\mathbf{k}+\mathbf{G}}(\mathbf{r})$ denotes the basis function of wavefunction. It is written in slightly different ways in order to distinct different methods in the following text, for example, $\phi_{\mathbf{k}+\mathbf{G}}^{APW}(\mathbf{r})$ represents the basis function for the APW method.

The basis set for APW is defined by Slater [98, 99]

$$\phi_{\mathbf{k}+\mathbf{G}}^{APW}(\mathbf{r}) = \begin{cases} \frac{1}{\sqrt{\Omega}} e^{i(\mathbf{k}+\mathbf{G})\mathbf{r}} & \text{if } \mathbf{r} \in I \\ \sum_{\alpha}^{N_{\alpha}} \sum_{\ell}^{N_{\ell}} \sum_{m}^{N_m} f_{\ell m}(r_{\alpha}, \mathbf{k} + \mathbf{G}) Y_{\ell m}(\hat{\mathbf{r}}_{\alpha}) & \text{if } r_{\alpha} \in MT. \end{cases} \quad (3.51)$$

Here, $f_{\ell m}(r_{\alpha}, \mathbf{k} + \mathbf{G}) = A_{\ell m}^{\alpha}(\mathbf{k} + \mathbf{G}) u_{\ell}(r_{\alpha})$, and $A_{\ell m}^{\alpha}(\mathbf{k} + \mathbf{G})$ is the expansion coefficient. The radial function can be calculated by Eq. 3.52, where the radial function $u_{\ell}(r_{\alpha})$ is dependent with energy $\epsilon_{i,k}^{KS}$.

$$-\frac{1}{r^2} \frac{d}{dr} (r^2 \frac{du_{\ell}}{dr}) + \left(\frac{\ell(\ell+1)}{r^2} + V_0^{KS}(r) \right) u_{\ell}(r_{\alpha}) = \epsilon_{i,k}^{KS} u_{\ell}(r_{\alpha}). \quad (3.52)$$

In MT region, $V^{KS}(\mathbf{r})$ is assumed to be spherically symmetric, and it can be substituted by its spherical average $V_0^{KS}(r)$.

Because the wavefunction has dual representation, one has to make sure the continuity on the sphere boundary, which is solved by matching each ℓm of the dual representation.

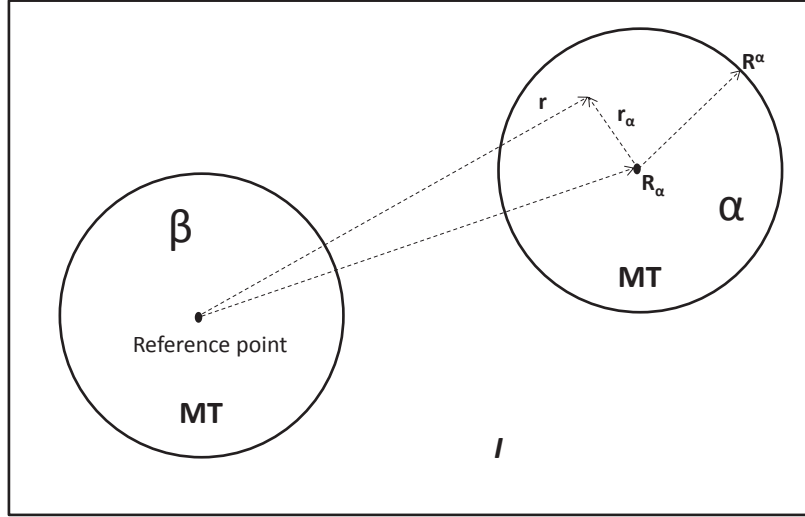


Figure 3.2. Partition of the unit cell.

In Fig. 3.2, one notices that unit cell is divided into MT spheres (α, β) and an I region, where $\mathbf{r} = \mathbf{R}_\alpha + \mathbf{r}_\alpha$ is guaranteed. The Rayleigh expansion formula yields

$$e^{i(\mathbf{k}+\mathbf{G})\mathbf{r}} = e^{i(\mathbf{k}+\mathbf{G})\mathbf{R}_\alpha} 4\pi \sum_{\ell}^{N_\ell} \sum_m^{N_m} i^\ell j_\ell(|\mathbf{k} + \mathbf{G}|r_\alpha) Y_{\ell m}(\hat{\mathbf{r}}_\alpha) \widehat{Y_{\ell m}(\mathbf{k} + \mathbf{G})}. \quad (3.53)$$

Therefore, the following equation is satisfied for each ℓm

$$A_{\ell m}^\alpha(\mathbf{k} + \mathbf{G}) u_\ell^\alpha(r_\alpha) = \frac{4\pi}{\sqrt{\Omega}} e^{i(\mathbf{k}+\mathbf{G})\mathbf{R}_\alpha} \sum_{\ell}^{N_\ell} \sum_m^{N_m} i^\ell j_\ell(|\mathbf{k} + \mathbf{G}|r_\alpha) Y_{\ell m}^*(\widehat{\mathbf{k} + \mathbf{G}}). \quad (3.54)$$

The main drawback about the APW method is that the wavefunction is energy-dependent (Eq. 3.52). It is time-consuming to calculate the exact energy.

Linearized augmented plane wave method

In order to decouple the energy from the wavefunction in the APW method, Andesen, Koelling and Arbman found out a way to separate them [100, 101]. They noticed that the Taylor expansion of the radial function on certain energy, which can be given as

$$u_\ell(r_\alpha, \epsilon) = u_\ell(r_\alpha, \epsilon_{\ell,\alpha}) + (\epsilon - \epsilon_{\ell,\alpha})\dot{u}_\ell(r_\alpha, \epsilon_{\ell,\alpha}) + O((\epsilon - \epsilon_{\ell,\alpha})^2). \quad (3.55)$$

Here, eigenvalue (ϵ) is written without subscript and superscript. Thus, the basis function is re-defined as

$$\phi_{\mathbf{k}+\mathbf{G}}^{LAPW}(\mathbf{r}) = \begin{cases} \frac{1}{\sqrt{\Omega}} e^{i(\mathbf{k}+\mathbf{G})\mathbf{r}} & \text{if } \mathbf{r} \in I \\ \sum_{\alpha} \sum_{\ell m} f_{\ell m}(r_\alpha, \mathbf{k} + \mathbf{G}, \epsilon_{\ell,\alpha}) Y_{\ell m}(\hat{\mathbf{r}}_\alpha) & \text{if } r_\alpha \in MT. \end{cases} \quad (3.56)$$

Here, $f_{\ell m}(r_\alpha, \mathbf{k} + \mathbf{G}, \epsilon_{\ell,\alpha}) = A_{\ell m}^\alpha(\mathbf{k} + \mathbf{G})u_\ell(r_\alpha, \epsilon_{\ell,\alpha}) + B_{\ell m}^\alpha(\mathbf{k} + \mathbf{G})\dot{u}_\ell(r_\alpha, \epsilon_{\ell,\alpha})$. $A_{\ell m}^\alpha(\mathbf{k} + \mathbf{G})$ and $B_{\ell m}^\alpha(\mathbf{k} + \mathbf{G})$ are expansion coefficients, and $\dot{u}_\ell(r_\alpha, \epsilon_{\ell,\alpha})$ is derivative of the radial function. Energy $\epsilon_{\ell,\alpha}$ is considered as pre-calculated parameter in Eq. 3.56. Actually, it is chosen by the middle of each ℓ -character band. Therefore this method is called linearized augmented plane wave (LAPW) method.

Apparently, LAPW method is more suitable in reality, because the wavefunction is decoupled with energy. However it has to match for two parameters. Fortunately, it still takes less time comparing with APW method. However, there is one drawback about this method, what if energy in the same ℓ -character is different enough, which $\epsilon_{\ell,\alpha}$ is correct? These states are called as semi-core states, which exist in the actinides and the rare earth elements.

Local orbitals

In order to solve semi-core states problem, a new basis function is added in the LAPW method. it is defined as

$$\phi_{\mathbf{k}+\mathbf{G}}^{LO}(\mathbf{r}) = \begin{cases} 0 & \text{if } \mathbf{r} \in I \\ (A_{\ell m}^{\alpha,LO}u_\ell(r_\alpha, \epsilon_{\ell,\alpha}) + B_{\ell m}^{\alpha,LO}\dot{u}_\ell(r_\alpha, \epsilon_{\ell,\alpha}) + C_{\ell m}^{\alpha,LO}u_\ell(r_\alpha, \epsilon'_{\ell,\alpha}))Y_{\ell m}(\hat{\mathbf{r}}_\alpha) & \text{if } r_\alpha \in MT. \end{cases} \quad (3.57)$$

Here, $A_{\ell m}^{\alpha,LO}$, $B_{\ell m}^{\alpha,LO}$, and $C_{\ell m}^{\alpha,LO}$ can be obtained by normalization, as well as value and derivation on the sphere boundary to zero. The $\epsilon'_{\ell,\alpha}$ is the chosen energy from semi-core state. This method is called as linearized augmented plane wave method plus local orbitals (LAPW+LO) method.

There is another method called augmented plane wave method plus local orbitals (APW+lo), which can solve the APW method efficiently. The basis function has two types: one is similar with APW method, but without the derivative terms, that is, $f_{\ell m}(r_\alpha, \mathbf{k} + \mathbf{G}, \epsilon_{\ell,\alpha}) = A_{\ell m}^\alpha(\mathbf{k} + \mathbf{G})u_\ell(r_\alpha, \epsilon_{\ell,\alpha})$; the other basis function is

$$\phi_{\mathbf{k}+\mathbf{G}}^{lo}(\mathbf{r}) = \begin{cases} 0 & \text{if } \mathbf{r} \in I \\ (A_{\ell m}^{\alpha,lo} u_\ell(r_\alpha, \epsilon_{\ell,\alpha}) + B_{\ell m}^{\alpha,lo} \dot{u}_\ell(r_\alpha, \epsilon_{\ell,\alpha})) Y_{\ell m}(\hat{\mathbf{r}}_\alpha) & \text{if } r_\alpha \in MT. \end{cases} \quad (3.58)$$

Value of $A_{\ell m}^{\alpha,lo}$ and $B_{\ell m}^{\alpha,lo}$ are obtained by normalization, and local orbital has zero value at the muffin tin boundary. This method is not suitable for the calculations considering semi-core states. However, it does increase the efficiency. Certainly, There are some types of basis function which can mix the advantages from mentioned methods.

3.5.3 Effective potential

The potential in the FPLAPW method is also divided into two regions, the MT region and the I region [104].

$$V(\mathbf{r}) = \begin{cases} \sum_{\mathbf{G}} V_{\mathbf{G}} e^{i\mathbf{Gr}} & \text{if } \mathbf{r} \in I \\ \sum_{\ell m} V_{\ell m}^\alpha(r_\alpha) Y_{\ell m}(\hat{\mathbf{r}}_\alpha) & \text{if } r_\alpha \in MT. \end{cases}$$

3.6 Dielectric function

The dielectric function describes optical property of materials [106, 107]. Normally, it is written as $\varepsilon(\omega)$, which has two parts

$$\varepsilon(\omega) = \varepsilon_1(\omega) + i\varepsilon_2(\omega). \quad (3.59)$$

Here, $\varepsilon_1(\omega)$ denotes how much the material is polarized when an electric field is applied, and $\varepsilon_2(\omega)$ is related with absorption of the material. The imaginary part of interband contribution to the dielectric function is defined as

$$\varepsilon_2^{\alpha\beta}(\omega) = \frac{\hbar e^2}{\pi m^2 \omega^2} \sum_{cv} \int d\mathbf{k} \langle \Psi_{c\mathbf{k}} | p^\alpha | \Psi_{v\mathbf{k}} \rangle \langle \Psi_{v\mathbf{k}} | p^\beta | \Psi_{c\mathbf{k}} \rangle (f(\varepsilon_{c\mathbf{k}}) - f(\varepsilon_{v\mathbf{k}})) \delta(\varepsilon_{c\mathbf{k}} - \varepsilon_{v\mathbf{k}} - \omega). \quad (3.60)$$

Here, f is the Fermi distribution function, c and v are indices of conduction band and valence band. The total imaginary part of dielectric function can be calculated when c and v run over all indices of the conduction bands and valence bands. Similarly, the interband contribution can be achieved by calculating single conduction band and single valence band.

The real part of dielectric function can be calculated by Kramers-Kronig relations

$$\varepsilon_1^{\alpha\beta}(\omega) = \delta_{\alpha\beta} + \frac{2}{\pi} \mathbf{P} \int_0^\infty \frac{\omega' \varepsilon_2^{\alpha\beta}(\omega')}{\omega'^2 - \omega^2} d\omega'. \quad (3.61)$$

Here, \mathbf{P} the Cauchy principal value. The absorption coefficient can be obtained by the real part and imaginary part of dielectric function

$$\alpha^{ii}(\omega) = \frac{\sqrt{2}\omega}{c} \left[\sqrt{\varepsilon_1^{ii}(\omega)^2 + \varepsilon_2^{ii}(\omega)^2} - \varepsilon_1^{ii}(\omega) \right]^{1/2}. \quad (3.62)$$

Here, Eq. 3.62 equation is only valid for the diagonal of the tensor.

In this section, only some basic equations are covered when it is related to calculate the dielectric function. One can find more detailed description in Ref. [108].

3.7 Spin-orbit coupling

3.7.1 Dirac equation

Non-relativistic quantum mechanics has broad application. However, the non-relativistic quantum is not suitable to describe the system, where the velocity of electrons is near the one of light c . Therefore, Dirac introduced an equation, which is called Dirac equation applying for relativistic case [109, 110].

Dirac defined the Hamiltonian as

$$H^{dirac} = c\boldsymbol{\alpha}\mathbf{P} + \beta m_e c^2 + V. \quad (3.63)$$

Here, $\mathbf{P} = -i\hbar\nabla$ is the momentum operator, V is the general potential, and m_e is the mass of electron. $\boldsymbol{\alpha}$ and β are 4×4 matrices, which are defined as

$$\boldsymbol{\alpha} = \begin{pmatrix} 0 & \boldsymbol{\sigma} \\ \boldsymbol{\sigma} & 0 \end{pmatrix}, \beta = \begin{pmatrix} \mathbf{I} & 0 \\ 0 & -\mathbf{I} \end{pmatrix}. \quad (3.64)$$

Here, \mathbf{I} is unit matrix. $\boldsymbol{\sigma}$ is Pauli matrix, which is given as

$$\boldsymbol{\sigma} = (\boldsymbol{\sigma}_x \ \boldsymbol{\sigma}_y \ \boldsymbol{\sigma}_z) \quad (3.65)$$

$$\boldsymbol{\sigma}_x = \begin{pmatrix} 0 & 1 \\ 1 & 0 \end{pmatrix}, \boldsymbol{\sigma}_y = \begin{pmatrix} 0 & -i \\ i & 0 \end{pmatrix}, \boldsymbol{\sigma}_z = \begin{pmatrix} 1 & 0 \\ 0 & -1 \end{pmatrix}. \quad (3.66)$$

3.7.2 Derivation of spin-orbit coupling

Assume that Ψ is the wavefunction of Hamiltonian in Eq. 3.63, which has four components [109, 110]. However, it can be written with only two terms

$$\Psi = \begin{pmatrix} \phi^\uparrow \\ \phi^\downarrow \\ \chi^\uparrow \\ \chi^\downarrow \end{pmatrix}, \Psi = \begin{pmatrix} \phi \\ \chi \end{pmatrix}. \quad (3.67)$$

Here, ϕ includes the two terms of ϕ^\uparrow and ϕ^\downarrow , and χ contains χ^\uparrow and χ^\downarrow . Under the non-relativistic limit, ϕ is bigger than χ by the ratio of v/c . Here, v and c are velocities of electrons and light, respectively. Therefore, the ϕ is considered as the large term and χ is the small one.

In order to derive the spin-orbit coupling term, we need to take use of the non-relativistic limit approximation ($v^2/c^2 \ll 1$). The time-independent Dirac equation is give as

$$E\Psi = (c\boldsymbol{\alpha}\mathbf{P} + \beta m_e c^2 + V)\Psi. \quad (3.68)$$

For convenience, the following equation is defined

$$E' = E - m_e c^2. \quad (3.69)$$

Here, E is the total energy, $m_e c^2$ and E' are the rest mass energy and the remaining energy excluding the rest mass energy, respectively. Under the non-relativistic limit, E' is far smaller than $m_e c^2$. The following equation is given when Eq. 3.67 and Eq. 3.69 are put into Eq. 3.68

$$\begin{aligned} (E' - V)\Phi - c\boldsymbol{\sigma}\mathbf{P}\chi &= 0 \\ -c\boldsymbol{\sigma}\mathbf{P}\Phi + (E' + 2m_e c^2 - V)\chi &= 0. \end{aligned} \quad (3.70)$$

To eliminate the χ (otherwise, it is the antiparticle problem), it ends up with the equation

$$\left(V + \frac{1}{2m_e} (\boldsymbol{\sigma}\mathbf{P}) \left(1 + \frac{E' - V}{2m_e c^2} \right)^{-1} (\boldsymbol{\sigma}\mathbf{P}) \right) \phi = E' \phi. \quad (3.71)$$

Here, $E' - V$ is far smaller than $2mc^2$, therefore, taking advantage of the Taylor expansion of it, as well as the following identites

$$\begin{aligned} [\mathbf{P}, V] &= -i\hbar\nabla V \\ (\boldsymbol{\sigma}\mathbf{A})(\boldsymbol{\sigma}\mathbf{B}) &= \mathbf{AB} + i\boldsymbol{\sigma}[\mathbf{A} \times \mathbf{B}]. \end{aligned} \quad (3.72)$$

The final equation is obtained under the non-relativistic limit

$$E'\phi = \left(\frac{\mathbf{P}^2}{2m_e} + V - \frac{\mathbf{P}^4}{8m_e^3 c^2} - \frac{i\hbar}{4m_e^2 c^2} (\nabla V) \mathbf{P} + \frac{\hbar}{4m_e^2 c^2} \boldsymbol{\sigma} [\nabla V \times \mathbf{P}] \right) \phi. \quad (3.73)$$

Furthermore, we can approximate the above equation to the simpler expression under spherical symmetry potential

$$E'\phi = \left(\frac{\mathbf{P}^2}{2m_e} + V - \frac{\mathbf{P}^4}{8m_e^3 c^2} - \frac{i\hbar}{4m_e^2 c^2} (\nabla V) \mathbf{P} + \frac{1}{2m_e^2 c^2} \frac{1}{R} \frac{dV}{dR} \mathbf{S} \mathbf{L} \right) \phi. \quad (3.74)$$

Here, $\mathbf{S} = \hbar \boldsymbol{\sigma}/2$ is the Pauli spinor, and $\mathbf{L} = \mathbf{R} \times \mathbf{P}$ is the orbital angular momentum operator. The terms of $\mathbf{P}^2/(2m_e) + V$ is Schrödinger term, $\mathbf{P}^4/(8m_e^3 c^2)$ and $i\hbar(\nabla V)\mathbf{P}/(4m_e^2 c^2)$ are the mass enhancement and Darwin term, respectively, both of them together is called the scalar relativistic approximation (SRA). The last term is the spin-orbit coupling (SOC) term. One has to notice that the Darwin term is not hermitian operator, alternatively, $\nabla^2 V/(8m_e^2 c^2)$ is suggested in the realistic implementation.

Eq. 3.73 is only valid if the velocity of electrons is slower than the one of light. It is not true in the region which is close to the nucleus for heavy elements, where the relativistic effects are relatively strong. Moreover, the Coulomb potential can be arbitrarily large negative energies in realistic situation as well. Therefore, there is another way to derive the spin-orbit coupling, which can overcome the mentioned disadvantages.

Eq. 3.71 can be rewritten as

$$\begin{aligned} & \left(V + (\boldsymbol{\sigma} \mathbf{P}) \left(\frac{c^2}{2m_e c^2 - V} \right) \left(1 + \frac{E'}{2m_e c^2 - V} \right)^{-1} (\boldsymbol{\sigma} \mathbf{P}) \right) \phi \\ & \approx \left(V + (\boldsymbol{\sigma} \mathbf{P}) \left(\frac{c^2}{2m_e c^2 - V} \right) (\boldsymbol{\sigma} \mathbf{P}) \right) \phi \\ & \quad - (\boldsymbol{\sigma} \mathbf{P}) \left(\frac{c^2}{2m_e c^2 - V} \right) \left(\frac{E'}{2m_e c^2 - V} \right)^{-1} (\boldsymbol{\sigma} \mathbf{P}) \phi + \dots \\ & = E' \phi. \end{aligned} \quad (3.75)$$

Here, the Taylor expansion is utilized. The zeroth order regular approximation (ZORA) Hamiltonian [111–113] is defined as

$$\begin{aligned} H^{zora} &= V + (\boldsymbol{\sigma} \mathbf{P}) \left(\frac{c^2}{2m_e c^2 - V} \right) (\boldsymbol{\sigma} \mathbf{P}) \\ &= V + \mathbf{P} \left(\frac{c^2}{2m_e c^2 - V} \right) \mathbf{P} + \frac{c^2}{(2m_e c^2 - V)^2} \boldsymbol{\sigma} \cdot (\nabla V \times \mathbf{P}). \end{aligned} \quad (3.76)$$

The last term in **Eq. 3.76** is the spin-orbit coupling term.

3.8 $\mathbf{k} \cdot \mathbf{p}$ method

The energy band dispersion can be obtained exactly by using the $\mathbf{k} \cdot \mathbf{p}$ method in principle. The basic idea of this method is explained in this section based on Refs. [114, 115]. The non-relativistic Kohn-Sham equation (not in atomic units) is given as

$$\left(\frac{\mathbf{p}^2}{2m_e} + V(\mathbf{r}) \right) \Psi_{n,\mathbf{k}}(\mathbf{r}) = \epsilon_{n,\mathbf{k}} \Psi_{n,\mathbf{k}}(\mathbf{r}). \quad (3.77)$$

Here, \mathbf{p} is momentum operator, and the superscript "KS" is ignored compared with Eq. 3.37. According to the Bloch theory, the wavefunction can be written as

$$\Psi_{n,\mathbf{k}}(\mathbf{r}) = e^{i\mathbf{k}\mathbf{r}} u_{n,\mathbf{k}}(\mathbf{r}). \quad (3.78)$$

Here, $u_{n,\mathbf{k}}(\mathbf{r})$ is a function, which has the same periodicity as the potential. If substituting Eq. 3.78 to Eq. 3.77, a new equation is derived as

$$\left(\frac{\mathbf{p}^2}{2m_e} + V(\mathbf{r}) + \frac{\hbar^2 \mathbf{k}^2}{2m_e} + \frac{\hbar \mathbf{k} \mathbf{p}}{m_e} \right) u_{n,\mathbf{k}}(\mathbf{r}) = \epsilon_{n,\mathbf{k}} u_{n,\mathbf{k}}(\mathbf{r}). \quad (3.79)$$

In Eq. 3.79, the Hamiltonian becomes $H_0 = \mathbf{p}^2/2m_e + V(\mathbf{r})$ when $\mathbf{k} = \mathbf{0}$, the corresponding eigenvalue is $\epsilon_{n,\mathbf{0}}$. Here, terms in H_0 can be seen as non-perturbation terms, and remaining terms are seen as perturbation terms. From the perturbation theory, the following equation can be obtained

$$\epsilon_{n,\mathbf{k}} = \epsilon_{n,\mathbf{0}} + \frac{\hbar^2 \mathbf{k}^2}{2m_e} + \frac{\hbar^2}{m_e^2} \sum_n^N \sum_{n' \neq n}^N \frac{| \langle u_{n,\mathbf{0}}(\mathbf{r}) | \mathbf{k} \mathbf{p} | u_{n',\mathbf{0}}(\mathbf{r}) \rangle |^2}{\epsilon_{n,\mathbf{0}} - \epsilon_{n',\mathbf{0}}}. \quad (3.80)$$

In the realistic code implementation, the following derivation is exploited [116]. Assume that the wavefunction and eigenvalue are obtained by some procedures on \mathbf{k}_0 point. $\Psi_{n,\mathbf{k}_0}(\mathbf{r})$ is the corresponding wavefunction and $\epsilon_{n,\mathbf{k}_0}$ is the corresponding eigenvalue. Luttinger-Kohn function is given as

$$\chi_{n,\mathbf{k}}(\mathbf{r}) = e^{i(\mathbf{k}-\mathbf{k}_0)\mathbf{r}} \Psi_{n,\mathbf{k}_0}(\mathbf{r}). \quad (3.81)$$

The wavefunction on \mathbf{k} point can be expanded by $\chi_{n,\mathbf{k}}(\mathbf{r})$, which is given as

$$\Psi_{n,\mathbf{k}}(\mathbf{r}) = \sum_j^N C_{n,j}^{\mathbf{k}} \chi_{j,\mathbf{k}}(\mathbf{r}). \quad (3.82)$$

In Eq. 3.82, the wavefunction can be obtained if the coefficient $C_{n,j}^{\mathbf{k}}$ is obtained. Based on Eq. 3.82 and Eq. 3.77, the following equation is derived

$$\sum_j^N C_{n,j}^{\mathbf{k}} \left(\left(\epsilon_{n,\mathbf{k}_0} - \epsilon_{n,\mathbf{k}} + \frac{\hbar^2}{2m_e} (\mathbf{k}^2 - \mathbf{k}_0^2) \right) \delta_{j',j} + \frac{\hbar}{m_e} (\mathbf{k} - \mathbf{k}_0) \bar{\mathbf{p}}_{j',j} \right) = 0 \quad (3.83)$$

$$\bar{\mathbf{p}}_{j',j} = \langle u_{j',\mathbf{k}_0}(\mathbf{r}) | \mathbf{p} | u_{j,\mathbf{k}_0}(\mathbf{r}) \rangle.$$

Eq. 3.83 can be simplified as

$$\sum_j C_{n,j}^{\mathbf{k}} (H_{j',j} - \epsilon_{n,\mathbf{k}} \delta_{j',j}) = 0 \quad (3.84)$$

$$H_{j',j} = \left(\epsilon_{n,\mathbf{k}_0} + \frac{\hbar^2}{2m_e} (\mathbf{k}^2 - \mathbf{k}_0^2) \right) \delta_{j',j} + \frac{\hbar}{m_e} (\mathbf{k} - \mathbf{k}_0) \bar{\mathbf{p}}_{j',j}.$$

Here, the coefficient $C_{n,j}^{\mathbf{k}}$ and $\epsilon_{n,\mathbf{k}}$ can be calculated. Therefore, the wavefunction on any \mathbf{k} point can be obtained.

To utilize the $\mathbf{k}\cdot\mathbf{p}$ method for a concrete example, band dispersions and average effective masses of the valence band edges are derived briefly for zinc blende type semiconductors. Spin-orbit coupling (SOC) is considered in the derivation.

For most of zinc blende type semiconductors, energy bands of the valence band edges are 3-fold degenerate at the Γ point in the Brillouin zone without considering spin. However, they are 6-fold degenerate considering spin. In the case of SOC, it splits the 6-fold degeneracy into higher energy 4-fold bands (heavy hole (HH) and light hole (LH) bands) and lower energy 2-fold bands (split-off (SO) bands).

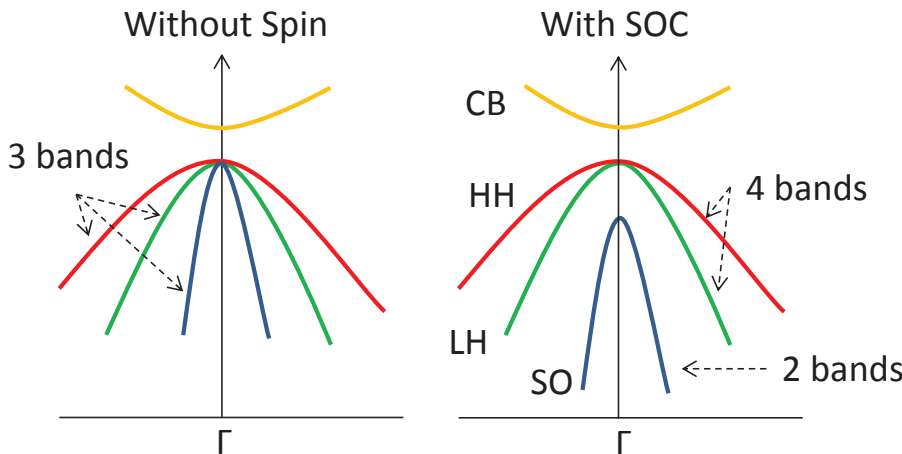


Figure 3.3. Band degeneracy of the valence band edges without spin and with spin-orbit coupling (SOC) for most of zinc blende type semiconductors.

Wavefunctions of these valence bands are p -like. The p -like wavefunction has three degenerate states if the spin is not considered. The arbitrary choice of a basis at $\mathbf{k}=0$,

and Hamiltonian $\hbar\mathbf{kp}/m_e$ is considered as perturbation. The following perturbation equation is derived without considering spin

$$\begin{vmatrix} Lk_x^2 + M(k_y^2 + k_z^2) - \lambda & Nk_xk_y & Nk_xk_z \\ Nk_xk_y & Lk_y^2 + M(k_x^2 + k_z^2) - \lambda & Nk_yk_z \\ Nk_xk_z & Nk_yk_z & Lk_z^2 + M(k_x^2 + k_y^2) - \lambda \end{vmatrix} = 0. \quad (3.85)$$

Here, L , M , and N are electron momentum matrix elements, and the corresponding 3×3 matrix in Eq. 3.85 is written as Y . The energy dispersion around the Γ point can be obtained from λ by

$$\epsilon = \frac{\hbar^2\mathbf{k}^2}{2m_e} + \lambda. \quad (3.86)$$

In the case of spin-orbit interaction, a 6×6 matrix can be expressed by the 3×3 matrix (Y) in Eq. 3.85

$$\begin{pmatrix} Y & 0 \\ 0 & Y \end{pmatrix}. \quad (3.87)$$

If the spin-orbit interaction (see Eq. 3.73) is considered as perturbation, a 6×6 matrix can be calculated. Approximately, the 6×6 matrix can be further divided into a 4×4 matrix and a 2×2 matrix. The 4-fold degenerate energy dispersions around the Γ point can be calculated by diagonalizing the 4×4 matrix, which is derived as

$$\epsilon_{v1,v2}(\mathbf{k}) = \frac{\hbar^2}{2m_0} \left\{ Ak^2 \pm [B^2k^4 + C^2(k_x^2k_y^2 + k_y^2k_z^2 + k_z^2k_x^2)]^{\frac{1}{2}} \right\}. \quad (3.88)$$

Here, A , B , and C are given as

$$\begin{aligned} A &= \frac{1}{3}(L + 2M) + \frac{\hbar^2}{2m_e} \\ B &= \frac{1}{3}(L - M) \\ C^2 &= \frac{1}{3}[N^2 - (L - M)^2]. \end{aligned} \quad (3.89)$$

Actually, L , M , and N do not need to be calculated because A , B , and C are the only fitting parameters in realistic application. .

The average heavy hole mass (m_{hh}) and light hole mass (m_{lh}) around the Γ point can be calculated from Eq. 3.88

$$m_{hh,lh}^{-1} = -m_0^{-1} \left[A \pm \sqrt{B^2 + C^2/5} \right]. \quad (3.90)$$

The 2-fold degenerate energy dispersion around the Γ point can be derived by diagonalizing the 2×2 matrix, which is derived as

$$\epsilon_{SO}(\mathbf{k}) = -\Delta_{SO} + A \frac{\hbar^2 k^2}{2m_0}. \quad (3.91)$$

Here, Δ_{SO} is the spin-orbit splitting energy. The average effective mass m_{SO} around the Γ point can be calculated from Eq. 3.91

$$m_{SO}^{-1} = m_0^{-1} A. \quad (3.92)$$

The derivation is brief, and the detailed derivation can be found in Refs. [117–120].

SHORT SUMMARY OF THE PAPERS

Chapter 4 Concluding remarks

4.1 Summary of the papers

I Parameterization of CuIn_{1-x}Ga_xSe₂ ($x = 0, 0.5$, and 1) energy bands

R. Chen and C. Persson, *Thin Solid Films* **519**, 7503 (2011).

The most fundamental property of a material is the energy of the electrons. That is determined by solving the Kohn-Sham equation (see Eq. 3.37). By understanding the electronic properties of the electrons one can understand many of the fundamental material properties. During the last two decades the electronic structure of CIGS has been explored, however the motivation of the present study is that much of the earlier studies describe the electronic structure and the corresponding density-of-states (DOS) on a wider energy scale, typically from 5–10 eV below valence bands maximum (VBM) to 5–10 eV above conduction band minimum (CBM). With that perspective one gets the overall understanding of the material, and one also gets the bond character, but details near the band edges are less revealed. The reason why details are important can be understood from different energy of relevance in materials. The energy to create defects is typically on the eV-scale (a Cu vacancy costs about 0.8 eV to be formed in CIS), the energy of band filling in heavily doped, degenerated semiconductors are typically in the 0.1 eV scale, and room temperature corresponds to $k_B T$ (around 0.025 eV). Thus, to understand band filling and transport of electrons/holes one has to understand the electronic structure on an energy scale of 1 meV to around 0.1 eV. Moreover, most of the earlier studies are on the ternary compounds CIS and CGS, whereas the experimentally and commercially most interesting compound is the CIGS alloy with about 70% In and 30% Ga, that is CuIn_{0.7}Ga_{0.3}Se₂. It is therefore interesting to understand how Ga-on-In alloying affects the electronic structure.

In this paper, we have therefore conducted a study on CuIn_{1-x}Ga_xSe₂, with $x = 0, 0.5$, and 1 . Here, $x = 0.5$ is not exactly the same configuration as for the commercially interesting compound, but it indicates how CIGS behaves when alloying In and Ga. Moreover, the present study focuses on the details in the electronic structure near the band edges. We do that by analyzing the lowest conduction band (CB) and the three uppermost valence bands (VBs) of CIGS ($x = 0, 0.5$, and 1) based on the FPLAPW calculations (Section

3.5) of the electronic band structure. The advantage of using the FPLAPW within the Wien2k package is that the code generates very accurate energy values in terms of noise and level of degeneracy of states, while the disadvantage is that the code does not have same possibility of choosing post-DFT calculations. Having accurate description of the degenerate states at Γ -point VBM is crucial when determining the effective hole masses there since one needs an accuracy of 0.01–0.1 meV. Therefore, we follow the FPLAPW calculation approach described in Ref. [60] which has shown to be able to overcome the problem with unwanted interaction between VB and CB states which can strongly affect the values of effective masses. It has also been proved to generate accurate values of the effective masses Ref. [120], and our result for effective electron mass of CIS ($m_{c1}=0.08m_0$) is close to the experimental results ($m_{c1}=0.09m_0$) by Weinert [121]. Thus, even if we do not generate the band structure with the exact exchange-correlation potential, we have reason to believe that the results are fairly good, and the results are useful when analyzing future measurements and simulations.

In this paper we present parameterization of electronic band structure of the lowest CB and the three uppermost VBs. These bands are the most important bands for electron and hole transport in the material. With the parameterization of the bands, other researchers can easily generate the energy bands in order to further investigate properties that are related to band filling and carrier transport.

The parameterization of the energy bands demonstrates that the energy dispersions of the lowest CB and three uppermost VBs are strongly anisotropic and non-parabolic close to the Γ -point. This anisotropy and non-parabolicity directly affect the effective electron and hole masses. Thereby we can better understand the CIGS. This parameterization method can be utilized to other materials potentially, such as kesterite and stannite $\text{Cu}_2\text{ZnSn}(\text{S},\text{Se})_4$, which we have presented in another work [122].

Using the parameterized electronic structure, we analyze the electrons and holes effective masses for these bands. The effective mass tensor ($\pm\hbar^2/(\partial^2 E(\mathbf{k})/\partial \mathbf{k}^2)|_{\mathbf{k}}$) is directly related to the curvature of the bands. The effective mass of the electron (or hole) is a very fundamental property of semiconductors and is used for various analyses of experiments and carrier transport simulations. Low effective mass value normally means better transport of the carriers, this is very important for the minority carriers (i. e., the electrons in *p*-type CIGS). In addition, and in models the effective mass is often used to approximately describe the band structure around the band edge, for instance to model band filling. Thus, the effective mass is used in two ways: to describe transport of a single carrier and to describe collective band filling. The effective masses are normally presented (both experimentally and theoretically) as constant value at the very minimum of the CBM or the very maximum of the VBM. That is correct if one can measure (or accurately calculate) details in the electronic structure near the band edges. However, very often one measures effective masses indirectly and for a material with high electron and hole concentrations. Therefore the measured mass value is not the mass at the very CBM or VBM but the mass near the quasi Fermi level. We therefore describe

the effective mass both as the Γ -point effective mass of the CB and the three VBs, but also an average mass that is energy-dependent and shall better represent the effective mass in models that describe transport. That is, one can use the energy-dependent mass $m(E)$ in existing models and a little better describe the physics of the material.

In Fig. 3 of Paper I, we illustrate how strongly the effective masses of the bands depend on specific \mathbf{k} -state that one considers. The Γ -point effective mass (value when wave vector equals 0) is only valid close to the Γ -point. Already some 5–10% away from the Γ -point mass value has changed. This is very obvious for the second uppermost VB (red lines) in CIS. One can notice that the behavior of the effective electron masses are similar while it differs much more for the effective holes masses between of the three compounds (i.e., $x = 0, 0.5$, and 1.0). This is a direct consequence of the different spin-orbit split-off and the crystal-field split-off energies. These splits directly affect the band curvatures and therefore the effective masses. This is discussed in the paper. Moreover, in the figure one can see that the effective mass is very anisotropic, that is, different in different \mathbf{k} directions; this is most obvious for the holes in the VBs. That means that carrier transport will be different in different \mathbf{k} directions.

In short, the main conclusions are:

1. The energy dispersions of the three uppermost VBs are strongly anisotropic and non-parabolic even very close to the Γ -point VBM.
2. The lowest CB is anisotropic and non-parabolic for energies around 50 meV above the band-gap energy.
3. The effective hole masses of the two topmost VBs are very strong anisotropy at the Γ -point.
4. All the three $\text{CuIn}_{1-x}\text{Ga}_x\text{Se}_2$ ($x = 0, 0.5$, and 1.0) compositions show comparable \mathbf{k} -dependency of their effective hole masses.

II Band-edge density-of-states and carrier concentrations in intrinsic and *p*-type $\text{CuIn}_{1-x}\text{Ga}_x\text{Se}_2$

R. Chen and C. Persson, *Journal of Applied Physics* **112**, 103708 (2012).

When a solar cell is under operation, the sunlight strongly excites electrons up to the CB and thereby also creating holes in the VBs. Then, one has quasi Fermi levels for the CB and the VBs. Also, with illumination, the device operation is in the order of 25 degrees Celsius and the temperature affects the carrier concentration. In addition, if the material is *n*- or *p*-type, one also needs to consider the electron states related to the dopants.

The motivation of this study is that we utilize the parameterized band dispersion of $\text{CuIn}_{1-x}\text{Ga}_x\text{Se}_2$ ($x = 0, 0.5$, and 1) in Paper I, and we want better analyze the impact on density-of-states (DOS) as well as carrier concentrations and Fermi energy by taking into account the non-parabolicity and anisotropy of the energy bands.

That is, in this work we explore how temperature and doping affect the carrier concentration and we compare the analyses done with the true, full electronic band structure and done with a corresponding model of the band structure generated by the Γ -point effective mass; the latter model is commonly used in semiconductor physics. In the paper, we denote these two models as full band parameterization (fpb) and the parabolic band approximation (pba), respectively. Also here we analyze the ternaries CIS ($x = 0$) and CGS ($x = 1$), but also the CIGS alloy with $x = 0.5$ to complement the analyses for materials that are used in today's solar cells. In the paper, we explore the DOS of the VBs and the CB, and we find that the parabolic approximation very poorly describes the DOS for especially the VB. Normally one uses the effective DOS mass to represent the parabolic description of the DOS, but that is thus not an accurate method for the VBs in CIGS. Therefore, we introduce energy-dependent DOS mass that can better represent the energy-dependent DOS, and that can be used in the traditional models. That is, with the DOS mass one can describe the band filling better, still using models that have been derived for a constant value of the DOS mass. The advantage is that the energy-dependent mass easily can be used in analyses of measurements where band filling is strong.

Moreover, with the parameterized bands we analyze temperature dependence of the carrier concentrations ($n = p$) in intrinsic material. As expected, the carrier concentration depends much on the band-gap energy of the material; the carrier concentration for Si (multi-valley CBM and $E_g \approx 1.2$ eV) is similar as in CIS ($E_g \approx 1.0$ eV) and the carrier concentration for GaAs ($E_g \approx 1.5$ eV) lies between CIGS with $x = 0.5$ ($E_g \approx 1.3$ eV) and CGS ($E_g \approx 1.6$ eV).

We also model the temperature-dependent Fermi levels and carrier concentrations in *p*-type CIGS since the material is used as *p*-type absorber layer in solar cells. Thus, an accurate description of the temperature dependences are important in analyses and simulations of the material and devices. Here, we find that there is a large difference for the full band description compared with the parabolic approximation. The difference is explained by the non-parabolicity and anisotropy of the energy bands.

In short, the main conclusions are:

1. The three uppermost VBs are strongly anisotropic and non-parabolic.
2. The lowest CB becomes non-parabolic for energies 50–100 meV above the Γ -point band minimum.
3. A constant density-of-states (DOS) mass cannot accurately describe band filling of the valence bands even at low hole concentrations. Instead, we introduce an energy-dependent DOS mass that can be utilized to describe the carrier concentration and the Fermi energy using traditional equations for the DOS.
4. With the full description of the energy dispersion, the hole concentration is improved by a factor of 10–50 and the electron concentration is improved by a factor of 2–10 depending on quasi-Fermi energy.

5. The transition from the freeze-out region to the extrinsic region occurs well below the room temperature for uncompensated acceptor concentration below around 10^{17} cm^{-3} , whereas for higher concentrations, not all acceptors are ionized at $T = 300 \text{ K}$. Thus, with a more correct description of the energy dispersions, one can better analyze the electron and hole dynamics in the $\text{CuIn}_{1-x}\text{Ga}_x\text{Se}_2$ ($x = 0, 0.5$, and 1) alloys, thereby better understand the electrical properties of these compounds.

III Dielectric function spectra at 40 K and critical-point energies for $\text{CuIn}_{0.7}\text{Ga}_{0.3}\text{Se}_2$
 S.G. Choi, R. Chen, C. Persson, T.J. Kim, S.Y. Hwang, Y. D. Kim, and L. M. Mansfield, *Applied Physics Letters* **101**, 261903 (2012).

The most important optical property of a solar cell material is how the material absorbs the sunlight efficiently. The absorption coefficient $\alpha(\omega)$ describes this efficiency in units of $1/\text{length}$. That is, if the absorption coefficient is large, the thickness of the material can be thinner but still the material absorbs the same amount of sunlight. The absorption coefficient is related to the dielectric function through the expression in Eq. 3.62. There the imaginary part $\varepsilon_2(\omega)$ of the dielectric function is closely related to the absorption coefficient; for instance, both $\varepsilon_2(\omega)$ and $\alpha(\omega)$ are zero for photon energies smaller than the band-gap. That is, by analyzing the dielectric function one can also understand how the optical transition occurs and how good or bad the material is for a solar cell. That is, the imaginary part of the dielectric function is obtained from (see Eq. 3.60)

$$\varepsilon_2^{\alpha\beta}(\omega) = \frac{\hbar e^2}{\pi m^2 \omega^2} \sum_{cv} \int d\mathbf{k} \langle \Psi_{c\mathbf{k}} | p^\alpha | \Psi_{v\mathbf{k}} \rangle \langle \Psi_{v\mathbf{k}} | p^\beta | \Psi_{c\mathbf{k}} \rangle (f(\varepsilon_{c\mathbf{k}}) - f(\varepsilon_{v\mathbf{k}})) \delta(\varepsilon_{c\mathbf{k}} - \varepsilon_{v\mathbf{k}} - \omega). \quad (4.1)$$

Thus, it is a summation of all possible band-to-band direct transitions from unoccupied to occupied states. The energy needed for excitation depends on the energy difference between final and initial states (indicated by the delta-Dirac function in the equation) and the strength of the absorption possibility which is described by the optical matrix element $\langle \Psi_{c\mathbf{k}} | p^i | \Psi_{v\mathbf{k}} \rangle$. While the energy difference between final and initial states only depends on the electronic band structure, the optical matrix element depends on the shape and symmetry of the electron wave function. Certain band-to-band transition can be weak or strong depending on the wavefunction of the final and initial states. To understand the optical properties of a material, one needs to analyze the dielectric function in details.

The motivation of this study is that we help experimentalists to understand the dielectric function spectrum of $\text{CuIn}_{0.7}\text{Ga}_{0.3}\text{Se}_2$, but we also want to understand details in the optical transition for these types of materials. That is, we want to explore which energy bands and which electrons states are most optical active when the solar cell is under operation. By understanding that we can better explain the optical activity of the CIGS

material, but also understand how one shall modify the material or tailor-make similar compounds with even better optical efficiency.

In this paper, we have therefore calculated the spectrum of the dielectric function for $\text{CuIn}_{0.5}\text{Ga}_{0.5}\text{Se}_2$ by means of the all-electron FPLAPW method as in Papers I and II. The calculated dielectric function is compared with experimental data ($\text{CuIn}_{0.7}\text{Ga}_{0.3}\text{Se}_2$) at temperatures of 40 K and 300 K, and we find that results based on theory and experiment are in reasonable good agreement. We decompose the full dielectric function into the contributions from each band-to-band transition and for each state in the Brillouin zone. The different contributions to imaginary part of dielectric function in terms of the transitions between the valence bands and the conduction bands are identified based on this calculation. Moreover, the \mathbf{k} -dependence of the interband critical points along the main symmetry directions are analyzed as well. With these results, we can better understand and explain the dielectric function spectra obtained by experimentalist. The surprising conclusion is that there are different band-to-band transitions that are important and that several low-lying states in the VBs that strongly contribute to the total dielectric function. That is, a full band description is needed to accurately describe the optical activity of these materials.

In short, the main conclusions are:

1. The dielectric function calculated by our theoretical method shows a good agreement with the result of experiment.
2. Electronic origins of the observed critical-point (CP) features are discussed based on our theoretical calculations.
3. The pairs of valence and conduction bands along the main symmetry directions of Brillouin zone are suggested for the major CP features based on our theoretical calculations.

4.2 Conclusions and future perspectives

Chalcopyrite CIGS is seen as one of the most promising materials for the near future thin-film solar-cell technology. The maximum conversion efficiency of 23.3% for the CIGS was achieved in the laboratory [11]. Solar cell modules based on CIGS are already commercially reality and contribute today with about 2.5% of the solar cell market.

Although the material properties are known from earlier theoretical and experimental studies, details in the electronic structure of the band edges are less studies, especially not for the alloy $\text{CuIn}_{1-x}\text{Ga}_x\text{Se}_2$.

In this licentiate thesis, two major researches are presented: (i) Analysis of the electronic structure of $\text{CuIn}_{1-x}\text{Ga}_x\text{Se}_2$ with $x = 0, 0.5$, and 1. Here, we parameterize the energy

bands in order to better describe energy dispersions and better analyze the electron and hole dynamics in the materials. We consider intrinsic and *p*-type materials, and we model the temperature dependence. The research is presented in Paper I and II. (ii) Analysis of the optical properties of $\text{CuIn}_{0.5}\text{Ga}_{0.5}\text{Se}_2$. Here, the dielectric function spectra is calculated and compared with experimental result. The probable electronic origins of the critical point features are discussed as well. The research is presented in Paper III.

Overall, we find that it is important to consider the full band description of the material to understand the fundamental properties of the electronic structure and the optical activity. Especially, the energetically high lying Cu *d*-states in CIGS plays a significant role since they hybridized with the In or Ga and Se states near the VBM and some 2–5 eV below the VBM. Cu *d*-states form flat energy bands in the VB that contribute to a high optical efficiency of the compound. This hybridization makes the VBs very non-parabolic, also for the uppermost VBs at least away from the Γ -point of the Brillouin zone. Therefore, a parameterization of the bands is rather complex. Moreover, we find that it is crucial to include the spin-orbit interaction when analyzing details in the electronic structure. Both the spin-orbit split-off and the crystal-field split-off make the uppermost VBs strongly non-parabolic also close to the Γ -point. The impacts of the spin-orbit interaction and the crystal-field are less important when studying properties related to total energy, like ion relaxation, defect formation energies, etc, but in studies related to excitation, band filling, and carrier transport one needs to consider these effects.

For future perspective and from a theoretical point of view, improved analyses can be done when better computational methods are developed. The LDA and GGA are fairly accurate methods, but have limitations in terms of inaccurate band-gap energies and localization of *d*- and *f*-states. The GW approach that we employ today is very time-consuming and it does not generate total energies; that limits the usability of the approach. Hybrid functionals (like HSE [123]) can give better band-gap energies, but this approach is as time-consuming as the GW approach which is a limitation for extensive research of complex materials. Moreover, there are discussions how the approach is to model details in accurately for instance defect transition energies. That is, further development of computational methods will help improving the results, however it is not certain that it will reveal very much new physics. Already with LDA and GGA we have reasonable understanding of the materials.

By understanding the electronic and optical properties of CIGS, we have the basic knowledge for studying also alternative materials in the future. Ideally, such materials should consist of inexpensive, earth-abundant, and non-toxic elements in addition to have crystal stability and high optical absorption efficiency.

The cost and scarcity of indium in the CIGS device is a problem, and copper zinc tin selenide ($\text{Cu}_2\text{ZnSnSe}_4$) and copper zinc tin sulfide ($\text{Cu}_2\text{ZnSnS}_4$) can therefore be alternative to CIGS due to the low cost and non-toxicity elements. $\text{Cu}_2\text{ZnSn}(\text{S},\text{Se})_4$ has many

similarities with CIGS, such as comparable crystal structure and tunable band-gap via anion alloying, as well as similar solar cell device structure and fabrication techniques. Since the research on those materials is relatively young, the solar-cell conversion efficiency is only around 12.6% in the laboratory [124]. The disadvantage is however that these quaternary chalcogenide semiconductors are more complicated compared with the more traditional thin-film materials, and the materials have more complex native defects.

One can also speculate if there are other similar materials that are of interest. CIGS and CZTS can be considered to be in a class denoted as Cu-XY-chalcogenide, where X and Y are two cation elements that replace the group-III In or Ga in CIGS. From the present study, we understand the advantage of having Cu as an element in the compound, but with choosing proper element for additional cation element one can maybe find optimal material with higher absorption coefficient. For instance, there are interesting papers describing $\text{Cu}(\text{Sb,Bi})(\text{S,Se})_2$ indicating very high absorption coefficient. Of course, Sb or Bi is not the best element to replace In or Ga, but by understanding the electronic and optical properties of these materials one can further understand the Cu-XY-chalcogenide type compounds. Cu_2O is studied as an absorber material for solar cells quite earlier [125], and this material is still considered as an interesting solar cell material if one can stabilize the structure. Cu_2S or $\text{Cu}_2(\text{O,S})$ is an alternative to that type of material.

For all these materials, and perhaps other Cu-XY-chalcogenide compounds one needs to explore the electronic and optical properties in combination with studies of crystalline stability/degradation, defect formation, and dopability. By systematically analyzing and understanding the materials one has better possibilities to tailor-make compounds with optimal performance for thin-film, and perhaps ultra-thin-film solar cells.

Acknowledgements

I would like to express my sincere appreciation to my supervisor Prof. Clas Persson for his academic encouragement and professional guidance. He is always showing a great interest to my projects and patient to teach me detailed material physics, which will be an invaluable asset to my future career.

I am grateful to Prof. Börje Johansson for the acceptance in his research group as a PhD student at KTH Royal Institute of Technology. I also thank Prof. Börje Johansson and Prof. Natalia Skorodumova for being my co-supervisor during my PhD study.

I appreciate Prof. Claudia Draxl to accept me visiting her group to learn the exciting code at the University of Leoben in Austria and Humboldt University of Berlin in Germany, respectively. I also thank all the people who give me support and discuss with me during my staying there.

I would like to thank all the group colleagues in Stockholm and Oslo for helpful research discussions and chatting: Alexander, Carlos, Dan, Fabiano, Girma, Gustavo, Hanyue, Kristian, Mathias, Maofeng, Mukesh, Priya, Roger, Sasha, Shen, Tiago. I also would like to thank Xuemei to help me arrange my apartment during staying in University of Oslo. I would like to thank all other people at the Department of Material Sciences and Engineering at KTH for creating a nice working atmosphere, especially for Huahai, Qiang and Song (names in alphabetical order).

The China Scholarship Council, the Swedish Energy Agency, the Swedish Research Council, Stiftelsen Axel Hultgrens fond, Olle Erikssons stiftelse för materialteknik, and KTH Computational Science and Engineering Centre (KCSE) are acknowledged for financial support.

Bibliography

- [1] British Petroleum, *Statistical Review of World Energy*. London: British Petroleum, 2014.
- [2] X. Xie and E. Bakker *Physical Chemistry Chemical Physics*, vol. 16, p. 19781, 2014.
- [3] N. S. Lewis and D. G. Nocera *Proceedings of the National Academy of Sciences*, vol. 103, p. 15729, 2006.
- [4] G. P. Smestad, *Optoelectronics of Solar Cells*. SPIE Press, 2002.
- [5] J. H. Seinfeld and S. N. Pandis, *Atmospheric Chemistry and Physics: from Air Pollution to Climate Change*. John Wiley & Sons, 2012.
- [6] G. Boyle, *Renewable Energy*. Oxford University Press, 2004.
- [7] D. Chiras, *Solar Electricity Basics: A Green Energy Guide*. New Society Publishers, 2010.
- [8] National Renewable Energy Laboratory, *Best Research-Cell Efficiencies*. United States of America: National Renewable Energy Laboratory, 2014.
- [9] F. Dimroth, M. Grave, P. Beutel, U. Fiedeler, C. Karcher, T. N. Tibbits, E. Oliva, G. Siefer, M. Schachtner, A. Wekkeli, A. W. Bett, R. Krause, M. Piccin, N. Blanc, C. Drazek, E. Guiot, B. Ghyselen, T. Salvetat, A. Tauzin, T. Signamarcheix, A. Dobrich, T. Hannappel, and K. Schwarzburg *Progress in Photovoltaics: Research and Applications*, vol. 22, p. 277, 2014.
- [10] A. Slade and V. Garboushian in *Technical Digest, 15th International Photovoltaic Science and Engineering Conference, Beijing*, 2005.
- [11] J. S. Ward, B. Egaas, R. Noufi, M. Contreras, K. Ramanathan, C. Osterwald, and K. Emery in *Photovoltaic Specialist Conference (PVSC), 2014 IEEE 40th*, p. 2934, IEEE, 2014.
- [12] M. A. Green, K. Emery, Y. Hishikawa, W. Warta, and E. D. Dunlop *Progress in Photovoltaics: Research and Applications*, vol. 23, p. 1, 2015.

- [13] Panasonic Corporation, *Panasonic's HIT Solar Cell Hits Record 25.6 Percent Conversion Efficiency*. Japan: Panasonic Corporation, 2014.
- [14] Zentrum für Sonnenenergie- und Wasserstoff-Forschung, *New Best Mark in Thin-film Solar Performance with 21.7 Percent Efficiency*. Germany: Zentrum für Sonnenenergie- und Wasserstoff-Forschung, 2014.
- [15] M. A. Green, A. Ho-Baillie, and H. J. Snaith *Nature Photonics*, vol. 8, p. 506, 2014.
- [16] M. D. McGehee *Nature Materials*, vol. 13, p. 845, 2014.
- [17] Fujifilm Corp, *High-durability Dye Improves Efficiency of Dye-sensitized Solar Cells*. Japan: Fujifilm Corp, 2013.
- [18] Mitsubishi Chemical Corp, *Mitsubishi Chemical Claims Efficiency Record for Organic Thin-film PV Cell*. Japan: Mitsubishi Chemical Corp, 2012.
- [19] A. J. Labelle, S. M. Thon, S. Masala, M. M. Adachi, H. Dong, M. Farahani, A. H. Ip, A. Fratalocchi, and E. H. Sargent *Nano Letters*, 2014.
- [20] E. in Chief: Ali Sayigh, *Comprehensive Renewable Energy*. Elsevier Science, 2012.
- [21] A. Sproul *Solar Cells: Resource for the Secondary Science Teacher*, 2003.
- [22] D. A. Neamen and B. Pevzner, *Semiconductor Physics and Devices : Basic Principles*. McGraw-Hill New York, 2003.
- [23] A. E. Becquerel *Comptes Rendus de l'Académie des Sciences*, vol. 9, p. 561, 1839.
- [24] L. Etgar *Materials*, vol. 6, p. 445, 2013.
- [25] G. Gourdin, *Introduction to Green Chemistry*. Lecture notes, 2007.
- [26] R. S. Ohl, *US Patent 2402622*. 1941.
- [27] R. S. Ohl, *US Patent 2443542*. 1941.
- [28] S. Chen, X. Gong, A. Walsh, and S.-H. Wei *Physical Review B*, vol. 79, p. 165211, 2009.
- [29] S. Chen, X. Gong, A. Walsh, and S.-H. Wei *Applied Physics Letters*, vol. 94, p. 041903, 2009.
- [30] A. Walsh, S.-H. Wei, S. Chen, and X. Gong in *Photovoltaic Specialists Conference (PVSC), 2009 34th IEEE*, p. 001875, 2009.
- [31] C. Goodman *Journal of Physics and Chemistry of Solids*, vol. 6, p. 305, 1958.
- [32] B. Pamplin *Journal of Physics and Chemistry of Solids*, vol. 25, p. 675, 1964.

- [33] W. Hoffmann *Solar Energy Materials and Solar Cells*, vol. 90, p. 3285, 2006.
- [34] W. D. Brewer, R. Wengenmayr, and T. Bührke, *Renewable Energy: Sustainable Concepts for the Energy Change*. John Wiley & Sons, 2013.
- [35] M. Cardona and Y. Y. Peter, *Fundamentals of Semiconductors*. Springer, 2005.
- [36] O. Madelung, *Semiconductors: Data Handbook*. Springer, 2004.
- [37] C. H. Henry *Journal of Applied Physics*, vol. 51, p. 4494, 1980.
- [38] W. Shockley and H. J. Queisser *Journal of Applied Physics*, vol. 32, p. 510, 1961.
- [39] Z. I. Alferov *Reviews of Modern Physics*, vol. 73, p. 767, 2001.
- [40] E. Yablonovitch, O. Miller, and S. Kurtz in *Photovoltaic Specialists Conference (PVSC), 2012 38th IEEE*, p. 001556, IEEE, 2012.
- [41] L. I. Maissel and R. Glang, *Handbook of Thin Film Technology*. McGraw-Hill, 1995.
- [42] D. E. Carlson and C. R. Wronski *Applied Physics Letters*, vol. 28, p. 671, 1976.
- [43] R. A. Street, *Technology and Applications of Amorphous Silicon*. Springer, 2000.
- [44] R. E. Schropp and M. Zeman, *Amorphous and Microcrystalline Silicon Solar Cells: Modeling, Materials and Device Technology*. Kluwer Academic Boston, 1998.
- [45] International Renewable Energy Agency Innovation Technology Centre, *Renewable Energy Technologies: Cost Analysis Series-Solar Photovoltaics*. Germany: International Renewable Energy Agency Innovation Technology Centre, 2012.
- [46] C. A. Wolden, J. Kurtin, J. B. Baxter, I. Repins, S. E. Shaheen, J. T. Torvik, A. A. Rockett, V. M. Fthenakis, and E. S. Aydil *Journal of Vacuum Science & Technology A*, vol. 29, p. 030801, 2011.
- [47] P. V. Meyers *Solar Cells*, vol. 23, p. 59, 1988.
- [48] First Solar, Inc., *First Solar Sets Thin-Film Module Efficiency World Record of 17.0 Percent*. United States of America: First Solar, Inc., 2014.
- [49] M. A. Green *Journal of Materials Science: Materials in Electronics*, vol. 18, p. 15, 2007.
- [50] M. Kumar, H. Zhao, and C. Persson *Thin Solid Films*, vol. 535, p. 318, 2013.
- [51] R. Chen and C. Persson *Journal of Applied Physics*, vol. 112, p. 103708, 2012.
- [52] R. Chen and C. Persson *Thin Solid Films*, vol. 519, p. 7503, 2011.
- [53] C. Persson *Thin Solid Films*, vol. 517, p. 2374, 2009.

- [54] M. A. Green, *Third Generation Photovoltaics: Advanced Solar Energy Conversion*. Springer, 2006.
- [55] H. Hahn, G. Frank, W. Klingler, A.-D. Meyer, and G. Störger *Zeitschrift für Anorganische und Allgemeine Chemie*, vol. 271, p. 153, 1953.
- [56] S. Wagner, J. L. Shay, P. Migliorato, and H. M. Kasper *Applied Physics Letters*, vol. 25, p. 34, 1974.
- [57] L. Kazmerski, F. White, and G. Morgan *Applied Physics Letters*, vol. 29, p. 268, 1976.
- [58] C. Parlak and R. Eryigit *Physical Review B*, vol. 73, p. 245217, 2006.
- [59] K. Hönes, M. Eickenberg, S. Siebentritt, and C. Persson *Applied Physics Letters*, vol. 93, p. 092102, 2008.
- [60] C. Persson *Applied Physics Letters*, vol. 93, p. 072106, 2008.
- [61] Z. B. Li *Advanced Materials Research*, vol. 239, p. 1304, 2011.
- [62] A. Luque and S. Hegedus, *Handbook of Photovoltaic Science and Engineering*. John Wiley & Sons, 2011.
- [63] C.-S. Jiang, R. Noufi, K. Ramanathan, J. AbuShama, H. Moutinho, and M. Al-Jassim *Applied Physics Letters*, vol. 85, p. 2625, 2004.
- [64] U. Rau and S. Siebentritt, *Wide-Gap Chalcopyrites*. Springer, 2006.
- [65] S. Chen, J.-H. Yang, X. Gong, A. Walsh, and S.-H. Wei *Physical Review B*, vol. 81, p. 245204, 2010.
- [66] S. Schuler, S. Siebentritt, S. Nishiwaki, N. Rega, J. Beckmann, S. Brehme, and M. C. Lux-Steiner *Physical Review B*, vol. 69, p. 045210, 2004.
- [67] S. Lany and A. Zunger *Physical Review Letters*, vol. 100, p. 016401, 2008.
- [68] S. Zhang, S.-H. Wei, A. Zunger, and H. Katayama-Yoshida *Physical Review B*, vol. 57, p. 9642, 1998.
- [69] O. Madelung, U. Rössler, and M. Schulz, *Springer Materials*. Springer, 2010.
- [70] H. Neumann *Solar Cells*, vol. 16, p. 317, 1986.
- [71] C. Persson, Y.-J. Zhao, S. Lany, and A. Zunger *Physical Review B*, vol. 72, p. 035211, 2005.
- [72] Y.-J. Zhao, C. Persson, S. Lany, and A. Zunger *Applied Physics Letters*, vol. 85, p. 5860, 2004.

- [73] O. Lundberg, M. Edoff, and L. Stolt *Thin Solid Films*, vol. 480, p. 520, 2005.
- [74] O. Lundberg, J. Lu, A. Rockett, M. Edoff, and L. Stolt *Journal of Physics and Chemistry of Solids*, vol. 64, p. 1499, 2003.
- [75] K. Ramanathan, M. A. Contreras, C. L. Perkins, S. Asher, F. S. Hasoon, J. Keane, D. Young, M. Romero, W. Metzger, R. Noufi, J. Ward, and A. Duda *Progress in Photovoltaics: Research and Applications*, vol. 11, p. 225, 2003.
- [76] K. H. Kim, K. C. Park, and D. Y. Ma *Journal of Applied Physics*, vol. 81, p. 7764, 1997.
- [77] T. Minami, H. Nanto, and S. Takata *Japanese Journal of Applied Physics*, vol. 23, p. L280, 1984.
- [78] N. Naghavi, D. Abou-Ras, N. Allsop, N. Barreau, S. Bücheler, A. Ennaoui, C.-H. Fischer, C. Guillen, D. Hariskos, J. Herrero, et al. *Progress in Photovoltaics: Research and Applications*, vol. 18, p. 411, 2010.
- [79] S. Niki, M. Contreras, I. Repins, M. Powalla, K. Kushiya, S. Ishizuka, and K. Matsubara *Progress in Photovoltaics: Research and Applications*, vol. 18, p. 453, 2010.
- [80] J. Kessler, M. Bodegård, J. Hedström, and L. Stolt *Solar Energy Materials and Solar Cells*, vol. 67, p. 67, 2001.
- [81] R. M. Martin, *Electronic Structure: Basic Theory and Practical Methods*. Cambridge University Press, 2004.
- [82] S. Cottenier, *Density Functional Theory and the Family of (L)APW-methods: A Step-by-step Introduction*. freely available http://www.wien2k.at/reg_user/textbooks, 2013.
- [83] M. Born and J. R. Oppenheimer *Annalen der Physik (Leipzig)*, vol. 84, p. 457, 1927.
- [84] D. R. Hartree *Proceedings of the Royal Society of London*, vol. A113, p. 621, 1927.
- [85] V. Fock *Zeitschrift für Physik*, vol. 61, p. 126, 1930.
- [86] P. Hohenberg and W. Kohn *Physical Review*, vol. 136, p. B864, 1964.
- [87] W. Kohn and L. J. Sham *Physical Review*, vol. 140, p. A1133, 1965.
- [88] C. Persson, *Brief Introduction to the Density Functional Theory*. Lecture notes, 2013.
- [89] D. P. Bertsekas, A. Nedić, and A. E. Ozdaglar, *Convex Analysis and Optimization*. Athena Scientific Belmont, 2003.
- [90] J. C. Slater *Physical Review*, vol. 81, p. 385, 1951.

- [91] U. von Barth and L. Hedin *Journal of Physics C: Solid State Physics*, vol. 5, p. 1629, 1972.
- [92] L. Hedin and B. Lundqvist *Journal of Physics C: Solid State Physics*, vol. 4, p. 2064, 1971.
- [93] D. J. Tozer and N. C. Handy *The Journal of Chemical Physics*, vol. 108, p. 2545, 1998.
- [94] F. A. Hamprecht, A. J. Cohen, D. J. Tozer, and N. C. Handy *The Journal of Chemical Physics*, vol. 109, p. 6264, 1998.
- [95] T. Grabo and E. K. Gross *Chemical Physics Letters*, vol. 240, p. 141, 1995.
- [96] A. J. Cohen, P. Mori-Sánchez, and W. Yang *The Journal of Chemical Physics*, vol. 126, p. 191109, 2007.
- [97] C. Kittel and P. McEuen, *Introduction to Solid State Physics*. Wiley New York, 1976.
- [98] J. Slater *Physical Review*, vol. 51, p. 846, 1937.
- [99] T. L. Loucks, *Augmented Plane Wave Method*. W.A. Benjamin, 1967.
- [100] O. K. Andersen *Physical Review B*, vol. 12, p. 3060, 1975.
- [101] D. Koelling and G. Arbman *Journal of Physics F: Metal Physics*, vol. 5, p. 2041, 1975.
- [102] D. Singh *Physical Review B*, vol. 43, p. 6388, 1991.
- [103] E. Sjöstedt, L. Nordström, and D. Singh *Solid State Communications*, vol. 114, p. 15, 2000.
- [104] L. Nordstrom and D. J. Singh, *Planewaves, Pseudopotentials, and the LAPW Method*. Springer, 2006.
- [105] A. Gulans, S. Kontur, C. Meisenbichler, D. Nabok, P. Pavone, S. Rigamonti, S. Sagmeister, U. Werner, and C. Draxl *Journal of Physics: Condensed Matter*, vol. 26, p. 363202, 2014.
- [106] D. R. Penn *Physical Review*, vol. 128, p. 2093, 1962.
- [107] M. Fox and G. F. Bertsch *American Journal of Physics*, vol. 70, p. 1269, 2002.
- [108] C. Ambrosch-Draxl and J. O. Sofo *Computer Physics Communications*, vol. 175, p. 1, 2006.
- [109] B. Thaller, *The Dirac Equation*. Springer-Verlag Berlin, 1992.
- [110] P. A. M. Dirac, *The Principles of Quantum Mechanics*. The Clarendon Press, 1930.

- [111] E. van Lenthe, E.-J. Baerends, and J. G. Snijders *The Journal of Chemical Physics*, vol. 101, p. 9783, 1994.
- [112] S. Faas, J. Snijders, J. Van Lenthe, E. Van Lenthe, and E. Baerends *Chemical Physics Letters*, vol. 246, p. 632, 1995.
- [113] E. Van Lenthe, J. Snijders, and E. Baerends *The Journal of Chemical Physics*, vol. 105, p. 6505, 1996.
- [114] L. C. L. Y. Voon and M. Willatzen, *The kp Method*. Springer, 2009.
- [115] E. Kane *Semiconductors and Semimetals*, vol. 1, p. 75, 1966.
- [116] C. Persson and C. Ambrosch-Draxl *Computer Physics Communications*, vol. 177, p. 280, 2007.
- [117] Y. Peter and C. Manuel, *Fundamentals of Semiconductors: Physics and Materials Properties*. Springer, 2010.
- [118] M. Suzuki, T. Uenoyama, and A. Yanase *Physical Review B*, vol. 52, p. 8132, 1995.
- [119] G. Dresselhaus, A. Kip, and C. Kittel *Physical Review*, vol. 98, p. 368, 1955.
- [120] C. Persson and U. Lindefelt *Journal of Applied Physics*, vol. 82, p. 5496, 1997.
- [121] H. Neumann, N. Van Nam, H.-J. Höbler, and G. Kühn *Solid State Communications*, vol. 25, p. 899, 1978.
- [122] C. Persson, R. Chen, H. Zhao, M. Kumar, and D. Huang, "Electronic structure and optical properties from first-principles modeling," in *Copper zinc tin sulphide-based thin film solar cells* (K. Ito, ed.), John Wiley & Sons, 2014.
- [123] J. Paier, M. Marsman, K. Hummer, G. Kresse, I. C. Gerber, and J. G. Ángyán *The Journal of Chemical Physics*, vol. 124, p. 154709, 2006.
- [124] W. Wang, M. T. Winkler, O. Gunawan, T. Gokmen, T. K. Todorov, Y. Zhu, and D. B. Mitzi *Advanced Energy Materials*, vol. 4, p. 1301465, 2014.
- [125] L. O. Grondahl *Reviews of Modern Physics*, vol. 5, p. 141, 1933.

COMPILATION OF SCIENTIFIC PAPERS

Chapter 5 Work presented in scientific journals

5.1 Paper I: "Parameterization of CuIn_{1-x}Ga_xSe₂ (x = 0, 0.5, and 1) energy bands"

R. Chen and C. Persson, *Thin Solid Films* **519**, 7503 (2011).

Parameterization of $\text{CuIn}_{1-x}\text{Ga}_x\text{Se}_2$ ($x=0, 0.5$, and 1) energy bands

Rongzhen Chen*, Clas Persson

Department of Materials Science and Engineering, Royal Institute of Technology, SE-100 44 Stockholm, Sweden

ARTICLE INFO

Available online 13 January 2011

Keywords:
 CuInSe_2
 CuGaSe_2
 Chalcopyrite
 Solar cells
 Band structure
 Electronic structure
 Effective mass

ABSTRACT

Parameterization of the electronic band structure of $\text{CuIn}_{1-x}\text{Ga}_x\text{Se}_2$ ($x=0, 0.5$, and 1) demonstrates that the energy dispersions of the three uppermost valence bands [$E_j(\mathbf{k})$; $j=v1, v2$, and $v3$] are strongly anisotropic and non-parabolic even very close to the Γ -point valence-band maximum $E_{v1}(\mathbf{0})$. Also the lowest conduction band $E_{c1}(\mathbf{k})$ is anisotropic and non-parabolic for energies ~ 0.05 eV above the band-gap energy. Since the electrical conductivity depends directly on the energy dispersion, future electron and hole transport simulations of $\text{CuIn}_{1-x}\text{Ga}_x\text{Se}_2$ need to go beyond the parabolic approximation of the bands. We therefore present a parameterization of the energy bands, the \mathbf{k} -dependency of the effective electron and hole masses $m_j(\mathbf{k})$, and also an average energy-dependent approximation of the masses $m_j(E)$.

© 2011 Elsevier B.V. All rights reserved.

1. Introduction

The effective electron and hole masses $m_j(\mathbf{k})$ are very often utilized to represent the shape of the energy bands, thus assuming parabolic energy dispersion. However, typically these effective masses describe the energy bands only near the considered \mathbf{k} -point, whereas away from this point the bands can be strongly non-parabolic. If the non-parabolicity occurs within the energy region of temperature statistics (~ 0.03 eV), band-filling effects (~ 0.1 eV) or sunlight absorption and hot electron transport (~ 0.5 eV), the exact shape of the bands has to be considered when analyzing modeled and measured results involving for instance electron transport or band filling of the materials.

In this work, we have parameterized the lowest conduction band (CB) and the three uppermost valence bands (VBs) of $\text{CuIn}_{1-x}\text{Ga}_x\text{Se}_2$ ($x=0, 0.5$, and 1 ; thus CuInSe_2 , $\text{CuIn}_{0.5}\text{Ga}_{0.5}\text{Se}_2$, and CuGaSe_2) in order to better describe the non-parabolic and anisotropy of the energy bands $E_j(\mathbf{k})$. We report that the three topmost VBs ($E_j(\mathbf{k})$ with $j=v1, v2$, and $v3$) are very non-parabolic and anisotropic for energies $E_j(\mathbf{k}) < E_{v1}(\mathbf{0}) - 0.01$ eV. This non-parabolicity is mainly due to the split of degeneracy caused by the spin-orbit and crystal-field interactions. Also the lowest CB ($j=c1$) starts to become non-parabolic and anisotropic for energies above $E_{c1}(\mathbf{k}) > E_{c1}(\mathbf{0}) + 0.05$ eV. However, this non-parabolicity is a normal effect of the Bloch-periodic crystal potential. With the parameterized energy dispersion, the \mathbf{k} -dependent electron and hole masses are analyzed, and especially the hole masses of the two topmost VBs show a strong \mathbf{k} -dependency. We also present an energy-dependent approximation of the masses $m_j(E)$ that can be used in already existing analysis methods involving the parabolic approximation and/or strong band-filling effects.

2. Parameterization of the energy bands

The employed electronic band structure originates from an all-electron and full-potential linearized augmented plane wave calculation [1,2] using the Engel–Vosko (EV) exchange-correlation potential within the generalized gradient approximation [3]. We have recently shown [4] that the regular local density approximation (LDA) underestimates the effective masses for materials with small direct energy gaps; this is due to a too strong coupling between the CB and VBs. For GaAs for instance (which is the group-III-V analogue to CuGaSe_2 , having also similar band-gap energies), the measured Γ -point electron mass is $m_c = 0.067 m_0$, the heavy-hole mass (averaged over \mathbf{k} -direction) is $m_{hh} = 0.51 m_0$, the light-hole mass is $m_{lh} = 0.08 m_0$, and the spin-orbit split-off hole mass is $m_{hh} = 0.15 m_0$ [5]. LDA underestimates the masses [6]: $m_c = 0.018 m_0$, $m_{lh} = 0.55 m_0$, $m_{lh} = 0.01 m_0$, and $m_{so} = 0.08 m_0$, whereas the EV potential generates much more accurate masses [6]: $m_c = 0.061 m_0$, $m_{hh} = 0.55 m_0$, $m_{lh} = 0.07 m_0$, and $m_{so} = 0.16 m_0$. The reason for the improved energy dispersion of the EV potential is that this exchange-correlation model generates better interaction potentials but less accurate total energies compared with LDA.

The employed calculation from Refs. [1] and [2] shows (solid lines in Fig. 1) that the VBs are anisotropic in an energy region about 0.0 – 1.0 eV below the VB maximum (VBM). In the (110) and (112) directions the two uppermost VBs are very flat, and they reach the Brillouin zone (BZ) edge at about -0.5 eV. A closer look at the VBM (Fig. 2; solid lines) reveals that the energy bands start to become very non-parabolic already in the 0.01 – 0.1 eV region below VBM. The parabolic approximation of ellipsoidal energy bands reads

$$E_j^{pb}(\mathbf{k}) = E_j(\mathbf{0}) \pm \left[\frac{\tilde{k}_x^2 + \tilde{k}_y^2}{m_j^\perp} + \frac{\tilde{k}_z^2}{m_j^\parallel} \right] \quad \text{with} \quad \tilde{k}_\alpha^2 = \frac{\hbar^2 k_\alpha^2}{2e}, (\alpha = x, y \text{ and } z), \quad (1)$$

* Corresponding author.

E-mail address: rche@kth.se (R. Chen).

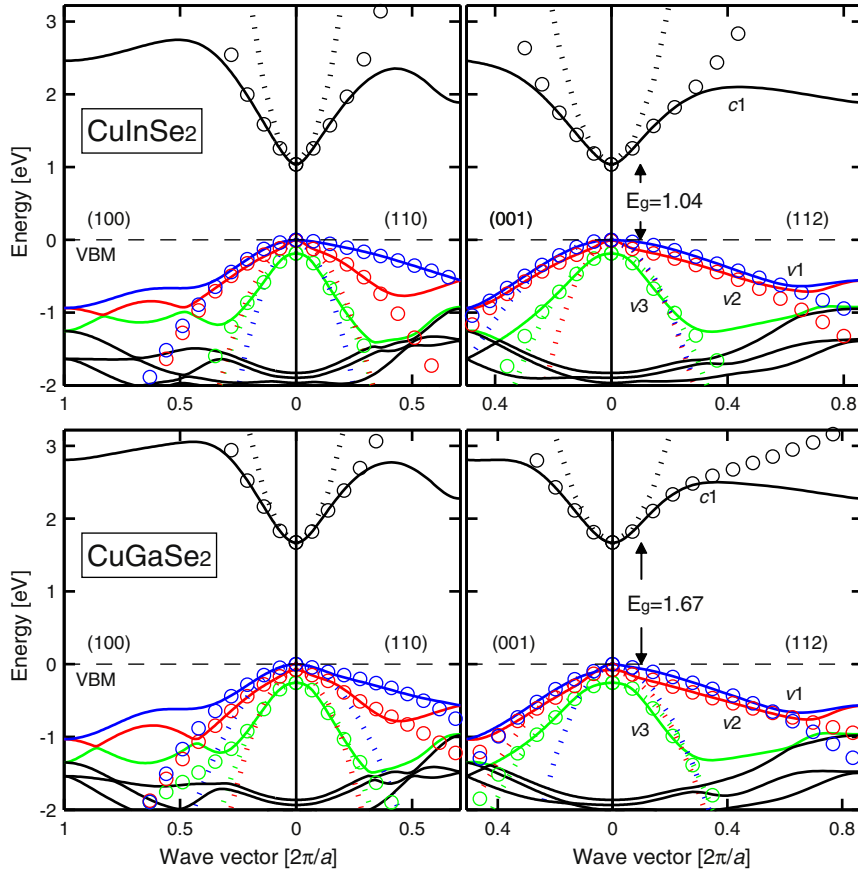


Fig. 1. Electronic band structure $E_j(\mathbf{k})$ of CuInSe₂ (upper panels) and CuGaSe₂ (lower panels) along the four symmetry directions (100), (110), (001), and (112). The energies referred to the VBM (dashed lines). The notation of the energy bands ($j = c1, v1, v2$, and $v3$) at the band edges refers to a spin-independent band indexing, where $c1$ represents the lowest CB and $v1$ represents the topmost VB. These VBs are highlighted with colors in the online version. The solid lines show the full-potential results from Refs. [1] and [2], the dotted lines represent the parabolic approximation of Eq. (1), and the circles are the fitted results of Eq. (2). Notice that the two uppermost VBs are badly described by the parabolic approximation in the main (100), (110), and (112) symmetry directions. Here, the notation of the symmetry directions (k_x , k_y , and k_z) is in units of $2\pi/a$, $2\pi/a$, and $2\pi/c$.

where e is the elementary charge and positive (negative) sign is for the CB (VBs). We have verified in this study that the ellipsoidal energy dispersion (Table 1) is valid for all four considered energy bands ($j = c1, v1, v2$, and $v3$) in the very vicinity of the Γ -point. However, away from the Γ -point, the parabolic approximation (dotted lines in Figs. 1 and 2) obviously fails to describe the energy dispersion of the VBs, especially for the topmost band in the (110) and (112) directions.

A common way to parameterize the energy bands is within the so called $\mathbf{k}\cdot\mathbf{p}$ approximation [7]. For cubic materials with twofold degenerate cation-s-anion-p bonding-like VBM the (spin-independent) energy dispersion has the form [7,8] $E_j(\mathbf{k}) = E_j^{pb}(\mathbf{k}) \pm \Delta \cdot (\delta \cdot (k_x^2 k_y^2 + k_y^2 k_z^2 + k_z^2 k_x^2) + k^4)^{1/2}$, and the corresponding expression for hexagonal structure is of the form $E_j(\mathbf{k}) = E_j^{pb}(\mathbf{k}) \pm \Delta \cdot (\delta \cdot k_\perp^4 + 1)^{1/2}$. However, the disadvantage with this method is that even for rather simple materials (like cubic or hexagonal SiC [8]) the parameterized bands can describe the VBs only close to the Γ -point. CuIn_{1-x}Ga_xSe₂ has a VBM involving Cu-d-Se-p antibonding-like state, and the crystal-field interaction as well as the spin-orbit coupling generates rather complex (anisotropic and non-parabolic) energy dispersions (Figs. 1 and 2). Therefore, the regular $\mathbf{k}\cdot\mathbf{p}$ approximation is not a sufficient method for describing the energy bands of CuIn_{1-x}Ga_xSe₂ down to ~ 0.5 eV below VBM. Instead, we start extend the $\mathbf{k}\cdot\mathbf{p}$ expressions to higher orders and with lower band symmetries, choosing the form $E_j(\mathbf{k}) = E_j^{pb}(\mathbf{k}) + \sum_{\alpha,n} \Delta_{\alpha,n} \cdot (\delta_{\alpha,n} \cdot k_\alpha^{2n} + 1)^{1/n}$. Each term alone describes a parabolic dispersion, but the higher order terms affect the dispersion for the larger wave vectors away from the

Γ -point. Thus, the combination of terms can therefore describe how local effects (like crystal field and spin-orbit coupling) re-shape the energy dispersion, that otherwise would be parabolic. We find that the following expression is suitable to describe the energy bands of CuIn_{1-x}Ga_xSe₂ down to ~ 0.5 eV below VBM:

$$\begin{aligned}
 E_j(\mathbf{k}) = & E_j^{pb}(\mathbf{k}) + E_j^0 + \Delta_{j,1} \left(\delta_{j,1}^2 \left(\frac{\tilde{k}_x^4 + \tilde{k}_y^4}{m_0^2} \right) + \delta_{j,2}^2 \left(\frac{\tilde{k}_x^2 \tilde{k}_y^2}{m_0^2} \right) + 1 \right)^{1/2} \\
 & + \Delta_{j,2} \left(\delta_{j,3}^3 \left(\frac{\tilde{k}_x^6 + \tilde{k}_y^6}{m_0^3} \right) + \delta_{j,4}^3 \left(\frac{\tilde{k}_x^2 \tilde{k}_y^4 + \tilde{k}_x^4 \tilde{k}_y^2}{m_0^3} \right) + 1 \right)^{1/3} \\
 & + \Delta_{j,3} \left(\delta_{j,5}^2 \left(\frac{\tilde{k}_z^4}{m_0^2} \right) + 1 \right)^{1/2} + \Delta_{j,4} \left(\delta_{j,6}^3 \left(\frac{\tilde{k}_z^6}{m_0^3} \right) + 1 \right)^{1/3} \\
 & + \Delta_{j,5} \left(\delta_{j,7}^2 \left(\frac{\tilde{k}_x^2 \tilde{k}_z^2 + \tilde{k}_y^2 \tilde{k}_z^2}{m_0^2} \right) + 1 \right)^{1/2} \\
 & + \Delta_{j,6} \left(\delta_{j,8}^3 \left(\frac{\tilde{k}_x^4 \tilde{k}_z^2 + \tilde{k}_y^4 \tilde{k}_z^2}{m_0^3} \right) + \delta_{j,9}^3 \left(\frac{\tilde{k}_x^2 \tilde{k}_z^4 + \tilde{k}_y^2 \tilde{k}_z^4}{m_0^3} \right) + \delta_{j,10}^3 \left(\frac{\tilde{k}_x^2 \tilde{k}_y^2 \tilde{k}_z^2}{m_0^3} \right) + 1 \right)^{1/3}. \tag{2}
 \end{aligned}$$

Unfortunately, the rather complex VB energy dispersions of CuIn_{1-x}Ga_xSe₂ require quite many fitting parameters (Eq. (2) and Table 2). The CB, however, needs less parameters.

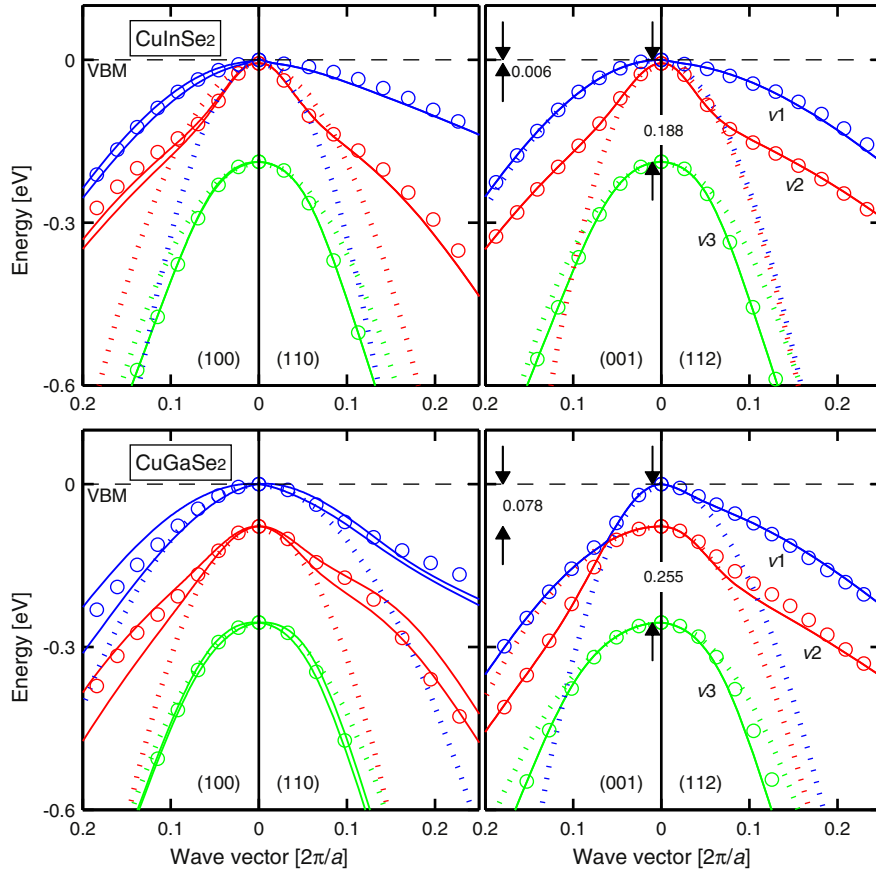


Fig. 2. Close-up of Fig. 1 demonstrating the strong non-parabolicity of the topmost VBs. Our parameterized energy bands $E_j(\mathbf{k})$ consider the average of the two spinor states $\psi_j^\sigma(\mathbf{k})$ with $\sigma = \downarrow$ and \uparrow , although there is a relatively large split of the spin-up- and spin-down-like bands in the (100)-direction; this average approximation is justified by $\psi_j^\sigma(-\mathbf{k}) = \psi_j^\sigma(\mathbf{k})$. Thus, the notation of the energy bands is $j = c1, v1, v2$, and $v3$ (where $c1$ represents the lowest CB and $v1$ represents the topmost VB) refers to a spin-independent band indexing.

Table 1

Parameters of Eq. (1) to describe the parabolic energy dispersions of the lowest CB and the three uppermost VBs in the vicinity of the Γ -point. $E_{v1}(\mathbf{0})$ is the VBM and $E_{c1}(\mathbf{0})$ is the fundamental band-gap energy E_g .

$\text{CuIn}_{1-x}\text{Ga}_x\text{Se}_2$	$x = 0.0$				$x = 0.5$				$x = 1.0$			
	$c1$	$v1$	$v2$	$v3$	$c1$	$v1$	$v2$	$v3$	$c1$	$v1$	$v2$	$v3$
$E_j(\mathbf{0})$ [eV]	0.97	0.00	0.01	0.19	1.20	0.00	0.02	0.20	1.47	0.00	0.08	0.26
m_j^\perp [m_0]	0.08	0.14	0.25	0.27	0.10	0.40	0.17	0.29	0.13	0.47	0.20	0.29
m_j^{\parallel} [m_0]	0.09	0.66	0.12	0.28	0.11	0.14	0.61	0.40	0.13	0.15	0.61	0.49

Table 2

Parameters of Eq. (2) to describe the non-parabolic contribution to the energy dispersions $E_j(\mathbf{k})$ of the lowest CB and the three uppermost VBs. The notation of the energy bands ($j = c1, v1, v2$, and $v3$) refers to a spin-independent band indexing, where $c1$ represents the bottommost CB and $v1$ represents the topmost VB (see Figs. 1 and 2).

$\text{CuIn}_{1-x}\text{Ga}_x\text{Se}_2$	$x = 0.0$				$x = 0.5$				$x = 1.0$			
	$c1$	$v1$	$v2$	$v3$	$c1$	$v1$	$v2$	$v3$	$c1$	$v1$	$v2$	$v3$
E_j^0 [eV]	-4.010	-5.311	-5.242	-5.620	-4.146	-6.210	-6.426	-5.835	-3.927	5.284	-5.789	-2.783
Δ_{j1} [eV]	-0.295	0.006	-0.002	-0.021	-0.230	0.106	1.321	-0.026	-0.454	0.116	1.284	1.194
Δ_{j2} [eV]	0	0.098	0.104	0.308	0	0.002	0.096	0.386	0	-10.771	-0.837	-0.024
Δ_{j3} [eV]	-0.242	0.018	0.124	-0.025	-0.293	0.937	-0.017	-0.838	-0.419	0.088	0.347	-0.303
Δ_{j4} [eV]	0	0.188	0.076	0.238	0	0.021	0.163	0.789	0	0.076	-0.051	0.608
Δ_{j5} [eV]	-0.016	-0.048	0.001	-0.009	-0.046	0.001	0.011	0.370	-0.047	0.022	0.274	0.374
Δ_{j6} [eV]	0	0.037	-0.073	0.117	0	-0.022	-0.313	-0.012	0	-0.111	-0.525	-4.362
δ_{j1} [eV $^{-1}$]	30.669	952.000	2304.147	94.139	27.157	5.517	1.029	57.007	11.865	10.526	9.269	3.839
δ_{j2} [eV $^{-1}$]	47.374	1754.386	4587.156	220.556	44.506	13.610	0.413	153.435	20.262	28.545	21.582	6.232
δ_{j3} [eV $^{-1}$]	0	3.970	72.296	11.746	0	487.805	46.950	8.489	0	0.131	9.116	59.625
δ_{j4} [eV $^{-1}$]	0	3.688	123.274	18.078	0	1128.668	72.844	13.509	0	0.126	21.328	148.516
δ_{j5} [eV $^{-1}$]	31.852	6.041	56.004	64.137	21.124	1.314	247.158	7.921	12.978	7.709	12.141	8.014
δ_{j6} [eV $^{-1}$]	0	3.134	6.100	12.031	0	267.523	29.076	8.743	0	64.185	66.808	5.309
δ_{j7} [eV $^{-1}$]	222.641	37.004	3846.154	206.148	79.879	3322.259	212.902	16.836	76.319	236.742	16.240	5.092
δ_{j8} [eV $^{-1}$]	0	12.647	16.269	6.982	0	92.954	4.885	57.890	0	31.947	6.710	1.209
δ_{j9} [eV $^{-1}$]	0	61.565	33.169	34.114	0	118.064	0.000	273.400	0	34.784	4.831	1.394
δ_{j10} [eV $^{-1}$]	0	46.679	31.275	32.237	0	110.327	6.074	153.523	0	40.765	5.243	2.124

The parameterized energy bands (circles in Figs. 1 and 2) can fairly accurately describe the energy bands for energies ~ 0.5 eV below the VBM and ~ 0.5 eV above the CB minimum (CBM). The energy difference of the two uppermost VBs at the Γ -point is only $E_{v1}(\mathbf{0}) - E_{v2}(\mathbf{0}) = 6, 18$, and 78 meV for CuInSe_2 , $\text{CuIn}_{0.5}\text{Ga}_{0.5}\text{Se}_2$, and CuGaSe_2 , respectively. These two VBs interact in this energy region which affects the band curvatures, and thus making the bands non-parabolic and anisotropic. Therefore, the parabolic approximation (represented by the Γ -point effective hole masses) is strictly valid only for energies to about -4 , -10 , and -40 meV below the VBM for CuInSe_2 , $\text{CuIn}_{0.5}\text{Ga}_{0.5}\text{Se}_2$, and CuGaSe_2 , respectively (see Fig. 2).

The CB has a rather spherical energy dispersion close to the Γ -point (i. e., $m_{c1,\perp} \approx m_{c1,\parallel}$; [1]). Since the CB is a single band, it is expected that the band is more parabolic and isotropic compared with the VBs. This is true, but already at an energy about 0.05 eV above the CBM $E_{c1}(\mathbf{0})$, the

band becomes both non-parabolic and anisotropic (e. g. Fig. 1). This is a consequence of the crystal potential that makes the CB flat at about 50% out from the Γ -point in the first BZ. Our fitting using Eq. (2) can describe this non-parabolicity and the anisotropy to describe the CB to about $\sim 50\%$ of the first BZ. However, the fitting cannot describe the flat curvature in the remaining part of the BZ in especially the (100) direction.

3. Effective electron and hole masses

From the parameterized energy bands of Eq. (2), the effective electron and hole mass tensors $m_j(\mathbf{k}) = \pm \hbar^2 / (\partial^2 E_j(\mathbf{k}) / \partial \mathbf{k}^2)|_{\mathbf{k}}$ were determined along the four symmetry directions. In Fig. 3, we present the inverse of the mass $m_j(\mathbf{k})^{-1}$ for better visibility; for instance, the mass goes to infinity (whereas inverse mass is zero) when the energy

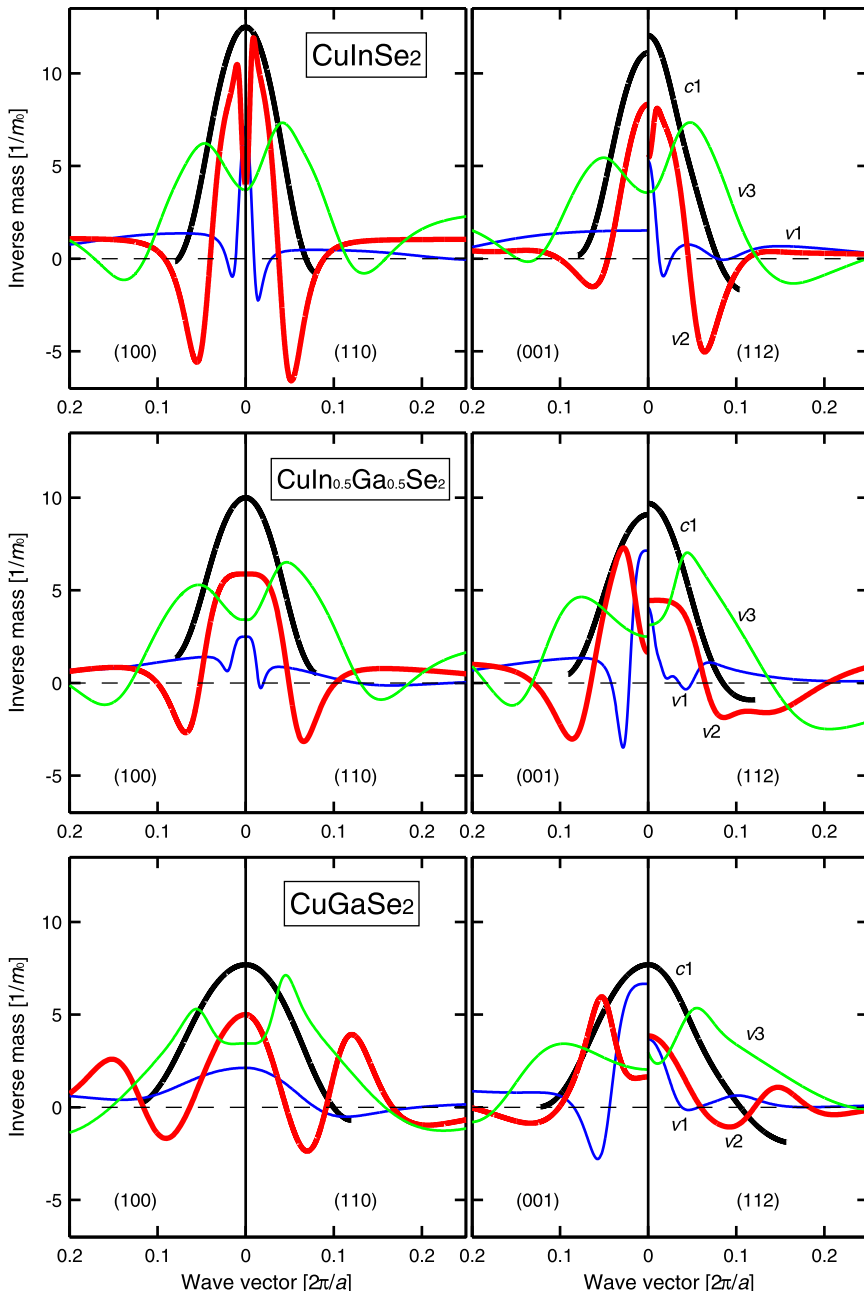


Fig. 3. Inverse of the effective electron and hole masses for $\text{CuIn}_{1-x}\text{Ga}_x\text{Se}_2$ ($x = 0, 0.5$, and 1) in the four symmetry directions as in Fig. 2, obtained from the second derivative of the energy dispersion: $m_j(\mathbf{k})^{-1} = \pm (\partial^2 E_j(\mathbf{k}) / \partial \mathbf{k}^2) / \hbar^2$. The band indices ($j = c1, v1, v2$, and $v3$) refer to the energy bands in Figs. 1 and 2. The presented masses are the component parallel to the considered symmetry directions.

dispersion $E_j(\mathbf{k})$ is linear with respect to \mathbf{k} . Fig. 3 demonstrates a strong non-parabolicity of all the considered bands, that is, $m_j(\mathbf{k})^{-1}$ is not constant along each symmetry direction. Moreover, it is clear from the figure that the CB has a rather isotropic electron mass tensor at the Γ -point [thus, $m_{c1}^{100}(\mathbf{0}) \approx m_{c1}^{110}(\mathbf{0}) \approx m_{c1}^{001}(\mathbf{0}) \approx m_{c1}^{112}(\mathbf{0})$]; this is especially true for CuGaSe₂ whereas the electron mass of CulnSe₂ is somewhat anisotropic, as discussed also in Ref. [1]. The effective hole masses of the two topmost VBs ($j=v1$ and $v2$) show very strong anisotropy at the Γ -point [e.g., $m_{v1}^{100}(\mathbf{0}) \neq m_{v1}^{001}(\mathbf{0}) \neq m_{v1}^{112}(\mathbf{0})$]. However, for all bands and at the Γ -point, the inverse mass in the (110)-direction equals the inverse mass in the (100)-direction [thus, $m_{j1}^{100}(\mathbf{0}) = m_{j1}^{110}(\mathbf{0})$], conforming that we can use the notation transverse mass $m_j^{\perp} \equiv m_{j1}^{100}$ and longitudinal mass $m_j^{\parallel} \equiv m_{j1}^{001}$ at the Γ -point.

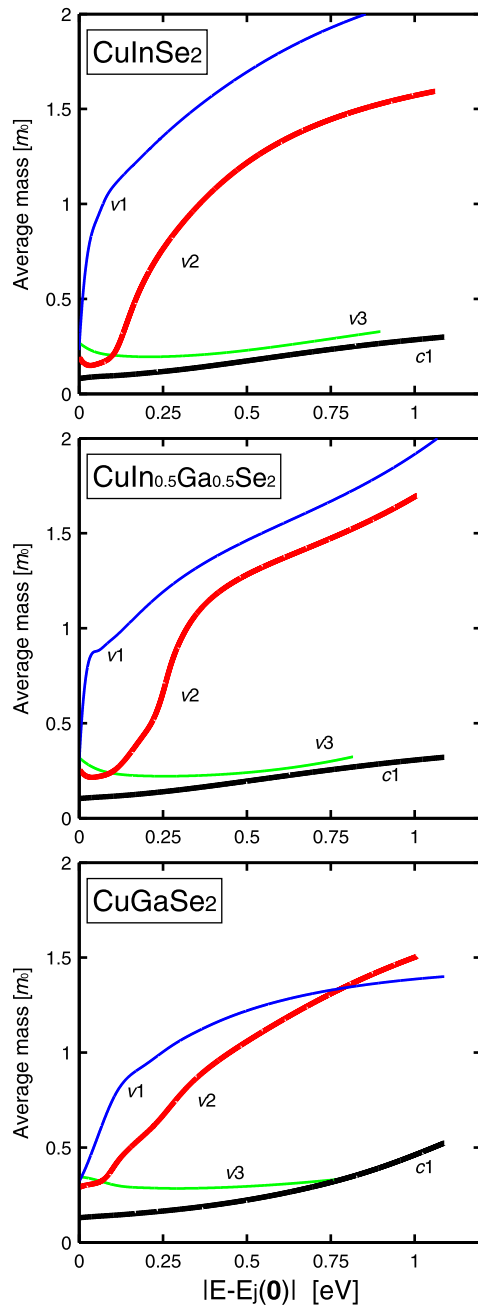


Fig. 4. The average energy-dependent masses of $\text{Culn}_{1-x}\text{Ga}_x\text{Se}_2$ ($x=0, 0.5$, and 1) to be used in analysis methods involving the parabolic approximation: $m_j(E) = \hbar^2(3\pi^2N/V)^{2/3}/2|E - E_j(\mathbf{0})|$, where N is the number of energy states inside the constant energy surface for a crystal with volume V . The band indices ($j=c1, v1, v2$, and $v3$) refer to the energy bands in Figs. 1 and 2.

At the very Γ -point, the values of the electron masses $m_{c1}(\mathbf{k}=\mathbf{0})$ in Table 1 confirm our earlier theoretical results [1]. Moreover, for CulnSe₂ the calculated electron mass components $m_{c1}^{\perp}=0.08\ m_0$ and $m_{c1}^{\parallel}=0.09\ m_0$ verify the Faraday rotation data by Weinert et al. [9] $m_{c1}=0.09\ m_0$ and Shubnikov-de Haas oscillation data by Arushanov et al. [10] $m_{c1}=0.08\ m_0$. However, from Fig. 3, it is clear that the effective electron mass increases (i.e., inverse mass decreases) away from the Γ -point. This will affect the electron transport properties at high electric applied field. At $|\mathbf{k}| \approx 0.1 \cdot 2\pi/a$ the mass is infinity (i.e., $m_j(\mathbf{k})^{-1}=0$). This occurs at about 0.3 eV above the CBM, reflecting that the CB starts to become more flat with a negative mass further out in the BZ (see Fig. 1). Our parameterized energy dispersion describes this effect on the mass, but it cannot describe the negative electron mass for $|\mathbf{k}| > 0.15 \cdot 2\pi/a$.

Since the spin-orbit coupling and the crystal field affect the VB curvatures near the Γ -point primarily, the uppermost VBs are strongly non-parabolic (Fig. 2), and this will directly affect the effective hole masses (Fig. 3). Hole masses of CuGaSe₂ vary somewhat less compared with those of CulnSe₂, mainly because CuGaSe₂ has larger split between the VBs. Overall, all the three $\text{Culn}_{1-x}\text{Ga}_x\text{Se}_2$ compositions show comparable \mathbf{k} -dependency of their masses.

Due to the strong non-parabolicity, the Γ -point hole masses are strictly valid only close to the Γ -point, and can therefore not be used to describe band filling. We therefore present also an average energy-dependent effective mass $m_j(E)$ that can be employed in future analysis (Fig. 4). This mass can thus describe the quasi Fermi level $|E - E_j(\mathbf{0})|$ as function of band filling. From the figure, it is clear that one needs to consider the non-parabolicity of the two uppermost VBs when to analyze hole transport or band filling effects. For instance, $m_{v1}^{\perp}=0.14\ m_0$ and $m_{v1}^{\parallel}=0.66\ m_0$ in CulnSe₂ yield $m_{v1}(E \approx 0) = (m_{v1}^{\perp}m_{v1}^{\parallel}m_{v1}^{\parallel})^{1/3}=0.23\ m_0$. This mass increases drastically when E increases to about $1.00\ m_0$ at $E=0.1\ \text{eV}$. This can thus explain the large measured hole masses $m_{v1} \approx 0.7\ m_0$ in CulnSe₂ [11,12] since the indirect measurements involves high hole concentrations. Also analyses involving band filling of the CB need to consider the non-parabolicity since the $m_{c1}(E)$ is increased by about a factor of 2 at energy $|E - E_{c1}(\mathbf{0})|=0.5\ \text{eV}$.

4. Summary

To summarize, the parameterization of the electronic band structure of $\text{Culn}_{1-x}\text{Ga}_x\text{Se}_2$ ($x=0, 0.5$, and 1) demonstrates that the energy dispersions of the lowest CB and uppermost VBs [that is, $E_j(\mathbf{k})$ with $j=v1, v2$, and $v3$] are strongly anisotropic and non-parabolic close to the Γ -point VBM $E_{v1}(\mathbf{0})$. This anisotropy and non-parabolicity directly affect the effective electron and hole masses.

Acknowledgements

This work is supported by the Swedish Energy Agency, the Swedish Research Council, the China Scholarship Council, and the computers centers NSC and HPC2N through SNIC/SNAC.

References

- [1] C. Persson, Appl. Phys. Lett. 93 (2008) 072106.
- [2] C. Persson, Thin Solid Films 517 (2009) 2374.
- [3] E. Engel, S.H. Vosko, Phys. Rev. B 47 (1993) 13164.
- [4] C. Persson, S. Mirbt, Br. J. Phys. 36 (2006) 286.
- [5] O. Madelung (Ed.), Semiconductors - Basic Data, 2nd ed., Springer, Berlin, 1996.
- [6] C. Persson, R. Ahuja, B. Johansson, Phys. Rev. B 64 (2001) 033201.
- [7] J.M. Luttinger, W. Kohn, Phys. Rev. 97 (1955) 869.
- [8] C. Persson, U. Linddefelt, J. Appl. Phys. 82 (1997) 5496.
- [9] H. Weinert, H. Neumann, H.-J. Höbler, G. Kühn, N. van Nam, Phys. Status Solidi B 81 (1977) K59.
- [10] E. Arushanov, L. Essaleh, J. Galibert, J. Leotin, M.A. Arsene, J.P. Peyrade, S. Askenazy, Appl. Phys. Lett. 61 (1992) 958.
- [11] N.N. Syrbu, I.M. Tiginyanu, L.L. Nemerenco, V.V. Ursaki, V.E. Tezlevan, V.V. Zalama, J. Phys. Chem. Solids 66 (2005) 1974.
- [12] H. Neumann, W. Kissinger, H. Sobotta, V. Riede, G. Kühn, Phys. Status Solidi B 108 (1981) 483.

5.2 Paper II: "Band-edge density-of-states and carrier concentrations in intrinsic and *p*-type CuIn_{1-x}Ga_xSe₂"

R. Chen and C. Persson, *Journal of Applied Physics* **112**, 103708 (2012).

Band-edge density-of-states and carrier concentrations in intrinsic and *p*-type $\text{CuIn}_{1-x}\text{Ga}_x\text{Se}_2$

Rongzhen Chen¹ and Clas Persson^{1,2}

¹Department of Materials Science and Engineering, Royal Institute of Technology, SE-100 44 Stockholm, Sweden

²Department of Physics, University of Oslo, P.O. Box 1048 Blindern, NO-0316 Oslo, Norway

(Received 25 May 2012; accepted 26 October 2012; published online 21 November 2012)

The electronic structures of chalcopyrite $\text{CuIn}_{1-x}\text{Ga}_x\text{Se}_2$ have recently been reported to have strongly anisotropic and non-parabolic valence bands (VBs) even close to the Γ -point VB maximum. Also, the lowest conduction band (CB) is non-parabolic for energies 50–100 meV above the CB minimum. The details in the band-edge dispersion govern the material's electrical properties. In this study, we, therefore, analyze the electronic structure of the three uppermost VBs and the lowest CB in $\text{CuIn}_{1-x}\text{Ga}_x\text{Se}_2$ ($x = 0$, 0.5, and 1). The parameterized band dispersions are explored, and the density-of-states (DOS) as well as the constant energy surfaces are calculated and analyzed. The carrier concentration and the Fermi energy E_F in the intrinsic alloys as functions of the temperature is determined from the DOS. The carrier concentration in *p*-type materials is modeled by assuming the presence of Cu vacancies as the acceptor type defect. We demonstrate that the non-parabolicity of the energy bands strongly affects the total DOS. Therefore, it is important to take into account full band dispersion of the VBs and CB when analyzing the free carrier concentration, like for instance, in studies of electronic transport and/or measurements that involve strong excitation conditions. © 2012 American Institute of Physics. [<http://dx.doi.org/10.1063/1.4767120>]

I. INTRODUCTION

The chalcopyrite $\text{CuIn}_{1-x}\text{Ga}_x\text{Se}_2$ alloy is one of the most important absorber material in the thin-film photovoltaic technology.¹ The performance of the solar cell is directly related to fundamental transport physics of the device.² The electrical properties of $\text{CuIn}_{1-x}\text{Ga}_x\text{Se}_2$ are dominated by the native defects, and whereas the defect concentration can vary in the order of percentage, the carrier concentration is typically well below 10^{20} cm^{-3} and the concentration can be controlled by the stoichiometry.^{3–5} Whereas CuInSe_2 can become *n*-type like, the Ga-rich compounds are compensated by charged Cu vacancies that will counteract the *n*-type character.^{3,6} $\text{CuIn}_{1-x}\text{Ga}_x\text{Se}_2$ is, therefore, preferable *p*-type. At very low temperatures, the acceptors are not fully thermally activated, and the electronic properties are governed by hopping conductivity.^{7–9}

Analyses of the measurements and modeling of for instance excitonic effects,¹⁰ carrier mobilities,¹¹ and current-voltage characteristics¹² require knowledge of basic the material electronic properties. Although most macroscopic properties of the compound are fairly well understood, there are only a handful studies on the details in the electronic energy dispersion near the valence-band (VB) and conduction-band (CB) edges.^{13,14} These studies consider primarily the characterization of the Γ -point states, involving measurements or calculations of the VB crystal-field and spin-orbit split-off energies. More detailed understanding of the energy dispersion at the VB maximum and the CB minimum is required to better understand the electrical properties of the material.

We have in Ref. 15 presented a parameterization of the energy bands $E_j(\mathbf{k})$ for the three energetically uppermost

VBs ($j = v1$, $v2$, and $v3$) and the lowest CB ($j = c1$) in $\text{CuIn}_{1-x}\text{Ga}_x\text{Se}_2$ with $x = 0$, 0.5, and 1. The parameterization was based on an expansion of the traditional $\mathbf{k} \cdot \mathbf{p}$ expression¹⁶ to higher order in order to describe the electronic band curvatures near the Γ -point. It was demonstrated that the VBs and CB are very non-parabolic away from the Γ -point. This indicates that one cannot use the Γ -point effective masses to describe material properties that depend on band filling and/or strong excitation effects. Instead, a full description of the band curvatures is required in combination with proper physical model of band filling.

In this work, we utilize these parameterized band dispersion $E_j(\mathbf{k})$ of $\text{CuIn}_{1-x}\text{Ga}_x\text{Se}_2$ from Ref. 15 for the group-III cation composition $x = 0$, 0.5, and 1, and we analyze the impact on the carrier concentrations n and Fermi energy $E_F(n)$ due to the non-parabolicity and anisotropy of the energy bands. The density-of-states (DOS) and the constant energy surface $S_j(E)$ are calculated for the three topmost VBs as well as for the lowest CB. From these calculations, we describe the intrinsic carrier concentration and the Fermi energy as functions of temperature T . Since as-grown $\text{CuIn}_{1-x}\text{Ga}_x\text{Se}_2$ typically has *p*-type character, we model also the carrier concentration in *p*-type materials by assuming the presences of the native Cu vacancies V_{Cu} as acceptors.¹⁷ Our main conclusion is that it is crucial to consider the non-parabolic of the VBs and CB dispersions when analyzing properties that are related to band filling. For instance, the intrinsic carrier concentration in CuInSe_2 increases by a factor of 2.4 at $T = 300 \text{ K}$ when the non-parabolicity is included.

We believe the results are important for accurately describing electron and hole dynamics in the $\text{CuIn}_{1-x}\text{Ga}_x\text{Se}_2$ alloys. For example, the DOS and the Fermi energy are fundamental quantities in Monte Carlo simulations of electronic transport

properties and also in modeling the transition probabilities. The Hall measurements involve the carrier concentration, and across-gap excitations depend on the details in the VBs and CB dispersions. These simulations and measurements require a detail description of the energy distribution of the free carriers.

II. THEORETICAL BACKGROUND

The parameterized electronic band structures (circles in Figs. 1 and 2) of $\text{CuIn}_{1-x}\text{Ga}_x\text{Se}_2$ are based on first-principles band structure calculation (solid lines in these figures) using the full-potential linearized augmented plane wave (FPLAPW) calculation.^{18,19} The parameterization was optimized in Ref. 15, and the details of the parameterization as well as a discussion about the methods are presented in that work. Here, we focus on the exploring the DOS and the carrier concentration.

Throughout this work, the energies are referenced to the VB maximum. The longitudinal \parallel direction is along the (001)

c -axis, and the transverse \perp direction is in the plane perpendicular to the longitudinal direction.

A. The density-of-states

The band-resolved DOS for the specific j th energy band is defined as

$$g_j(E) = \frac{1}{\Omega} \sum_{\mathbf{k}} 2\delta(E - E_j(\mathbf{k})) = \frac{1}{4\pi^3} \int_{E_j(\mathbf{k})=E} \frac{dS(\mathbf{k})}{|\nabla_{\mathbf{k}} E_j(\mathbf{k})|}, \quad (1)$$

where Ω is the volume of the solid, $E_j(\mathbf{k})=E$ is the \mathbf{k} -space surface with constant energy E , and $\nabla_{\mathbf{k}} E_j(\mathbf{k})$ is the gradient of the energy dispersion, $S(\mathbf{k})$ means the smooth two dimensional surface, and $dS(\mathbf{k})$ represents the gradient of this surface. Within the parabolic band approximation (pba), this equation becomes

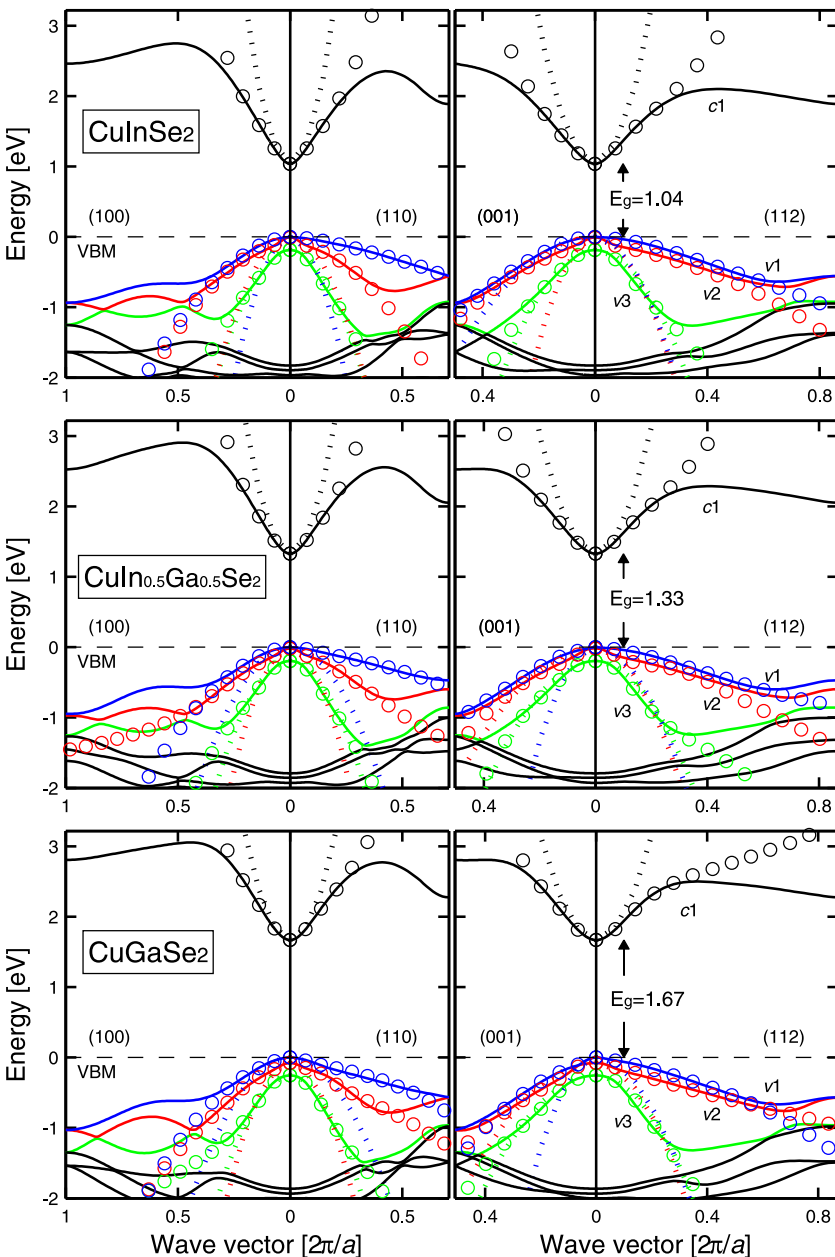


FIG. 1. Electronic band structure $E_j(\mathbf{k})$ of CuInSe_2 (upper panels), $\text{CuIn}_{0.5}\text{Ga}_{0.5}\text{Se}_2$ (middle panels), and CuGaSe_2 (lower panels) along four directions. The energies are referred to the VBM (dashed lines). Spin-orbit coupling is included, however, the notation of the energy bands ($j=v1, v2, v3$, and $c1$) refers to a spin-independent band indexing where $c1$ represents the lowest CB and $v1$ represents the topmost VB; these VBs are highlighted with colors in the online version. The solid lines show the full-potential results from Refs. 18 and 19, the circles are the results of the full band parameterization from Ref. 15, and the dotted lines represent the parabolic band approximation. Notice that the parabolic bands describe the two uppermost VBs poorly in the directions (100), (110), and (112).

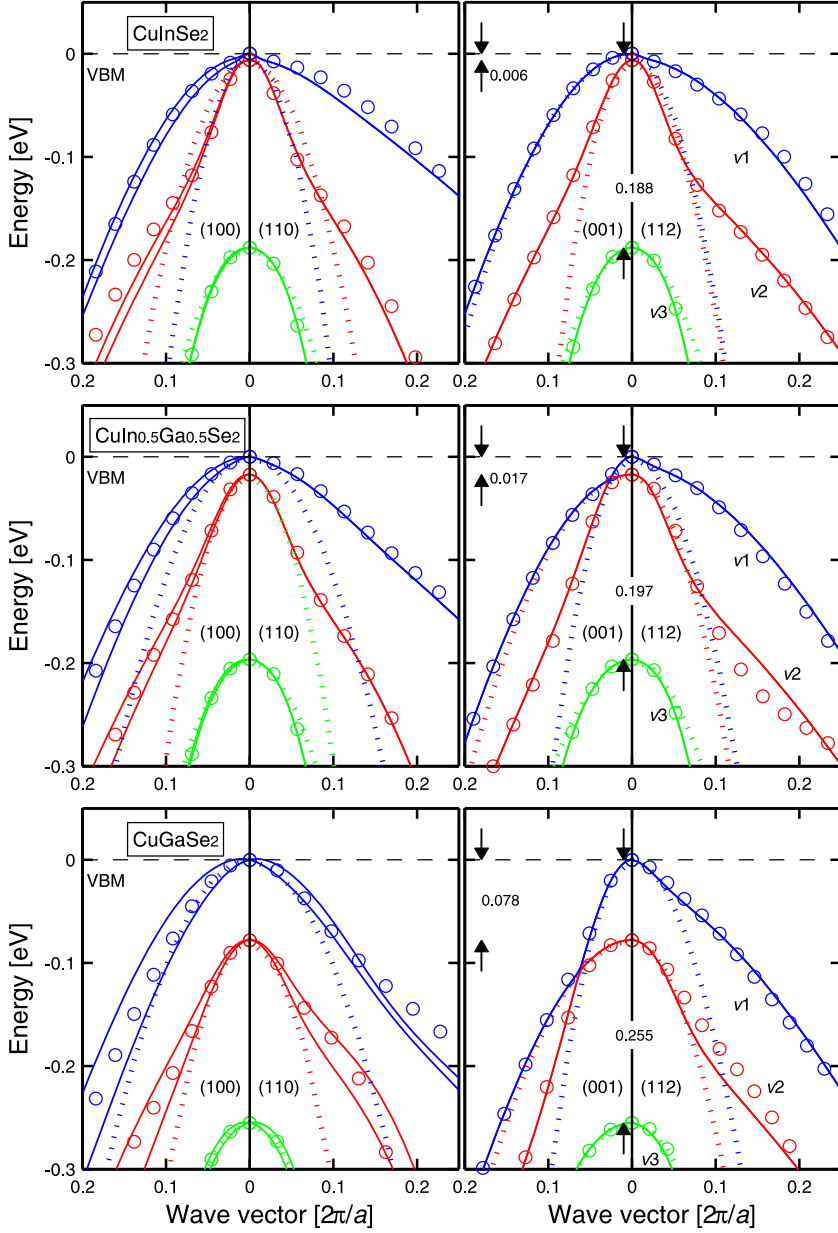


FIG. 2. Close-up of Fig. 1, demonstrating the strong non-parabolicity of the three uppermost VBs. Our parameterized energy bands $E_j(\mathbf{k})$ consider the average of the two spinor states $\psi_j^\sigma(\mathbf{k})$ with $\sigma = \downarrow$ and \uparrow , even though there is a relatively large split of the spin-up- and spin-down-like bands in the (100)-direction. This average approximation is justified by $\psi_j^\downarrow(-\mathbf{k}) = \psi_j^\uparrow(\mathbf{k})$, which overall make the material spin-independent. Therefore, the notation of the energy bands is $j = v1$, $v2$, and $v3$ refers to a spin-independent band indexing.

$$g_j^{pba}(E) = \frac{1}{2\pi^2} \left(\frac{2m_j^{DOS}}{\hbar^2} \right)^{3/2} \sqrt{|E - E_j(\mathbf{0})|}. \quad (2)$$

Here, $E_j(\mathbf{0})$ is the band-edge energy, and the DOS mass $m_j^{DOS} = (m_j^\perp m_j^\parallel m_j^{\parallel\parallel})^{1/3}$ is a parameter that represents the capability of filling the specific band with free carriers to certain energy. For non-parabolic energy bands, Eq. (1) still holds, but the surface energy and the gradient of the energy dispersion are more complex. However, in order to utilize the simple and conventional form of the DOS (i.e., Eq. (2)), we define an energy-dependent DOS mass $m_{v/c}^{DOS}(E)$ as

$$\begin{aligned} g_{v/c}(E) &= \sum_j g_j(E) \\ &= \frac{1}{2\pi^2} \left(\frac{2m_{v/c}^{DOS}(E)}{\hbar^2} \right)^{3/2} \sqrt{|E - E_{v1/c1}(\mathbf{0})|}. \end{aligned} \quad (3)$$

With this definition to describe the full DOS, the energy-dependent DOS mass $m_{v/c}^{DOS}(E)$ will include the non-parabolicity and anisotropy of the band dispersion. The total DOS $g_{v/c}(E)$ is obtained by a summation over all relevant bands of the band-resolved DOS $g_j(E)$; in this work, we distinguish between the total DOS of the valence bands $g_v(E)$ and the total DOS of the conduction bands $g_c(E)$.

B. The carrier concentration

The number of states $N_j(E)$ with energies up to E in the j th band is directly proportional to the \mathbf{k} -space volume enclosed by the constant energy surface $S_j(E)$. $N_j(E)$ is thus obtained by integrating $g_j(E)$ from $E_{v1/c1}(\mathbf{0})$ down/up to the energy E . In the case of band filling of free carriers with the concentration n , the constant energy surface is the Fermi energy $E_F(n)$.

The total concentration of free holes $n_v(T)$ in the valence bands and the total concentration of free electrons $n_c(T)$ in the conduction bands can be calculated from the DOS

$$n_v(T) = \int_{-\infty}^{E_{v1}(0)} g_v(E)(1-f(E))dE \text{ and} \quad (4)$$

$$n_c(T) = \int_{E_{c1}(0)}^{\infty} g_c(E)f(E)dE.$$

$f(E) = 1/[1+\exp\{(E-E_F)/k_B T\}]$ is the temperature dependent Fermi distribution function where E_F is the Fermi energy and k_B is the Boltzmann constant. The intrinsic carrier concentration $n_i(T)$ can be determined from

$$n_i(T) = \sqrt{n_c(T) \cdot n_v(T)}, \quad (5)$$

whereas the extrinsic carrier concentration for *p*-type materials can be calculated from²⁰

$$n_v(T) = \frac{n_i^2(T)}{n_v(T)} + \sum_{\alpha} \frac{N_{A_{\alpha}}}{1 + g_{A_{\alpha}} e^{(\Delta_{A_{\alpha}} - E_F)/k_B T}}. \quad (6)$$

Here, $N_{A_{\alpha}}$ is the acceptor concentration of the α th defect, $\Delta_{A_{\alpha}}$ is the energy level of the acceptor state, and $g_{A_{\alpha}}$ is the spin-degeneracy factor. In this work, we assume two inequivalent acceptor levels in $\text{CuIn}_{1-x}\text{Ga}_x\text{Se}_2$ due to the presence of Cu vacancies V_{Cu} . The measured ionization energies for V_{Cu} are:¹⁷ $E_A = 0.04$ eV and 0.06 eV for CuInSe_2 , $E_A = 0.055$ eV and 0.08 eV for $\text{CuIn}_{0.5}\text{Ga}_{0.5}\text{Se}_2$, and $E_A = 0.06$ eV and 0.10 eV for CuGaSe_2 . The value 0.08 eV for $\text{CuIn}_{0.5}\text{Ga}_{0.5}\text{Se}_2$ is an average estimate based on the values for CuInSe_2 and CuGaSe_2 . Since the energy levels are very similar in the three compounds, we expect that the two acceptor states are equally populated.

III. RESULTS: INTRINSIC $\text{CuIn}_{1-x}\text{Ga}_x\text{Se}_2$

The electronic structure of the $\text{CuIn}_{1-x}\text{Ga}_x\text{Se}_2$ alloys ($x=0$, 0.5 , and 1) is presented in Figs. 1 and 2. The solid lines represent the results from the FPLAPW calculation. The full band parameterization refers to results based on parameterized energy dispersion¹⁵ (circles in these figures), whereas the parabolic energy distribution (dotted lines) refers to the results based on energy bands with ellipsoidal shapes described by the Γ -point effective masses.^{18,19} It is clear from Fig. 1 that parabolic bands are not accurate enough for neither the lowest CB (at least not for energies larger than 50 – 100 meV above the band gap) nor for the three uppermost VBs. Especially, the VBs are strongly non-parabolic. This is due to the fact that the crystal-field and spin-orbit interactions are strongly \mathbf{k} -dependent. This is evident from Fig. 2, which shows the energy dispersion near the VB maximum, displaying non-parabolic band curvatures. The details in the curvatures of the topmost VBs and bottommost CB are related to the optical absorption in $\text{CuIn}_{1-x}\text{Ga}_x\text{Se}_2$. The absorption coefficient is relatively high in these chalcopyrites.^{7,21} It is almost $3 \times 10^4 \text{ cm}^{-1}$ at a photon energy of 0.5 eV above the band-gap energy and this is, in part, a direct consequence of the flat character of the band-energy dispersion.

To further illustrate the non-parabolicity, the constant energy surfaces $S_j(E)$ are determined (Fig. 3) for the energies $E = 1$ meV (thus, $S_j(E)$ near the Γ -point; left column in the figure) and $E = 200$ meV ($S_j(E)$ away from the Γ -point; right column). Close to the Γ -point, the effective mass tensor is a proper parameter to represent the energy dispersion¹⁸ in $\text{CuIn}_{1-x}\text{Ga}_x\text{Se}_2$, and thus the bands are in general ellipsoidal shaped there. For example, the effective masses for the top-most VB for CuInSe_2 are anisotropic ($m_{v1}^{\perp} = 0.14m_0$ and $m_{v1}^{\parallel} = 0.66m_0$), so the constant energy surface is ellipsoidal in the vicinity of the Γ -point. The average value ($\sim 0.23m_0$) of the calculated hole masses is smaller than the measured value $m_{v1} \approx 0.7m_0$ in CuInSe_2 by Syrbu *et al.*²³ and Neumann *et al.*²⁴ Moreover, the effective hole mass in CuGaSe_2 [average value of $\sim 0.32m_0$ (Ref. 15)] has been estimated experimentally to be $m_{v1} \approx 0.64m_0$ by Luckert *et al.*¹⁰ via magnetophotoluminescence measurements. Since the top-most VB is very non-parabolic, we expect that experimental results will yield a larger value if the measurements involves high hole concentration; see Sec. III A. Altogether, this indicates that the average hole mass at the Γ -point should be smaller than $\sim 0.7m_0$. The effective masses of the CB is however almost isotropic ($m_{c1}^{\perp} = 0.08m_0$ and $m_{c1}^{\parallel} = 0.09m_0$ for CuInSe_2), so the corresponding constant energy surface is nearly spherical. These theoretical data for the effective electron mass are verified experimentally by Weinert *et al.*²⁵ $m_{c1} = 0.09m_0$ from Faraday rotation and also by Arushanov *et al.*²⁶ $m_{c1} = 0.08m_0$ from Shubnikov-de Haas oscillation results.

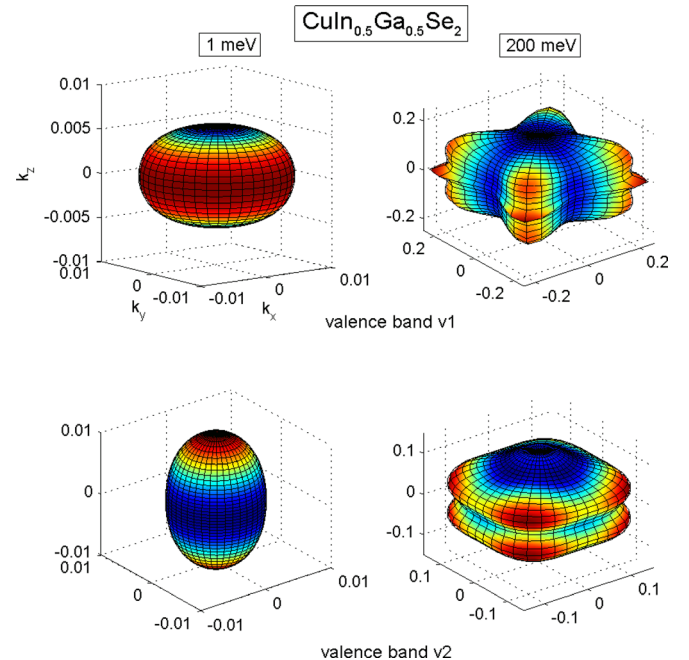


FIG. 3. Constant energy surfaces $S_j(E)$ for the two uppermost VBs in $\text{CuIn}_{0.5}\text{Ga}_{0.5}\text{Se}_2$ for the energies $E = 1$ meV (left column) and $E = 200$ meV (right column). The energy surfaces demonstrate that the VBs have ellipsoidal shapes in the vicinity of the Γ -point, but that they are very non-parabolic and anisotropic away from the Γ -point. In the supplementary information (Ref. 22), we present $S_j(E)$ for the CB, as well as corresponding results for CuInSe_2 and CuGaSe_2 .

With an increasing distance from the Γ -point, the shape of the constant energy surfaces change. For the CB, the change is small. Also for the third uppermost VB (denoted $v3$ in the figure), the change is moderate. However, the changes of the constant energy surfaces for the two uppermost VBs ($v1$ and $v2$) are significant. For example, the topmost VB shows an extended energy surface in the (110) directions, which is a direct consequence of the very flat energy dispersion along that symmetry direction (cf. Fig. 2). One can, therefore, expect a larger concentration of free holes in these \mathbf{k} -directions.

A. The DOS and the DOS masses

The total DOS of the VBs $g_v(E)$ and the total DOS of the CB $g_c(E)$ are presented in Fig. 4 for $\text{CuIn}_{1-x}\text{Ga}_x\text{Se}_2$. The difference between the parabolic approximation and the full parameterization of the bands is remarkable. This is true especially for the total DOS of the VBs, whereas the DOS of the CB indicates an ellipsoidal band curvature up to 50–100 meV above the band-gap energy. The full band

parameterization generates always larger DOS, and this is a direct consequence from the fact that the overall band curvature is more flat than the curvature at the vicinity of the VB maximum and CB minimum. It is also evident that the VB DOS is much larger than the CB DOS for corresponding energy E (notice the different scales for DOS of the VB and the CB in the figure). The VB DOS of CuGaSe_2 is somewhat smaller than those of CuInSe_2 and $\text{CuIn}_{0.5}\text{Ga}_{0.5}\text{Se}_2$. The reason is that CuGaSe_2 has larger split-off energies of the second and third VBs (thus, $v2$ and $v3$ contribute less to the DOS in CuGaSe_2) and that CuGaSe_2 has a less flat topmost VB (thus, $v1$ has a smaller DOS in CuGaSe_2). The CB DOS of CuGaSe_2 , however, is somewhat larger than those of CuInSe_2 and $\text{CuIn}_{0.5}\text{Ga}_{0.5}\text{Se}_2$ due to a more flat CB minimum.

From the total DOS and from the constant energy surfaces, the number of states with energies up to E is determined (Fig. 5). This quantity describes thus the carrier concentration due to external band filling of holes in the VBs and electrons in the CB for the given quasi-Fermi energies $E_{F,v}^*$ and $E_{F,c}^*$, respectively, and at temperature $T=0$ K. In agreement

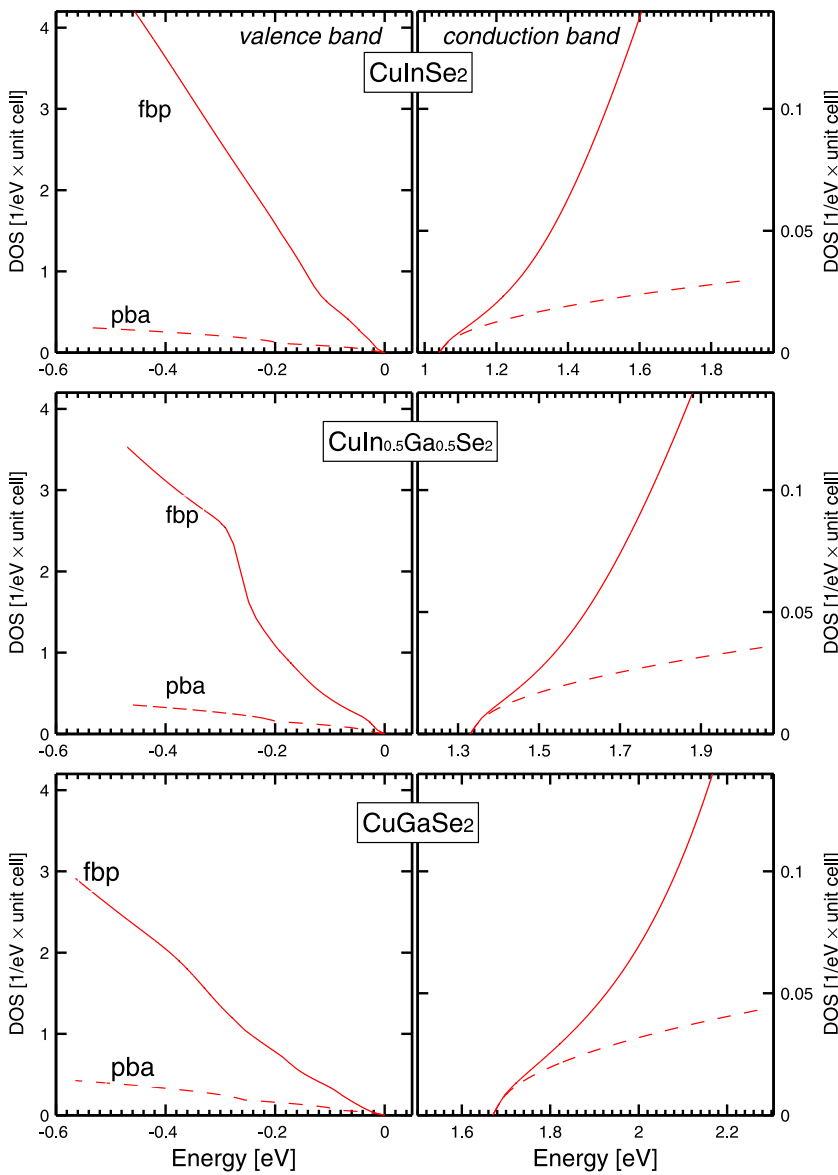


FIG. 4. Total DOS of the VBs (left panels) and of the CB (right panels) for CuInSe_2 , $\text{CuIn}_{0.5}\text{Ga}_{0.5}\text{Se}_2$, and CuGaSe_2 . The solid lines show the full band parameterization (fbp), and the dashed lines represent the parabolic band approximation (pba). The energies refer to the VBM. Notice the different scales in the figures for the VB and the CB. The results demonstrate that the non-parabolicity of the bands strongly affect the DOS dispersions.

with the discussion above for the total DOS, it is obvious that the VBs (CB) in Ga rich compounds will be less (more) populated by holes (electrons) for a given quasi-Fermi energy $E_{F,v}^*$ ($E_{F,c}^*$). Thus, CuGaSe₂ can more easily host free electrons due to a more flat CB. However, a flat band implies heavier mass and thereby a weaker response to an applied electric field, which is negative for the electron transport.

Fig. 5 also demonstrates that the parabolic approximation of the bands strongly underestimates the band filling in the VBs and the CB. For example, the number of VB states of CuInSe₂ is increased by a factor of ~ 18 at the positive energy $|\Delta E| = E_{v1}(0) - E_{F,v}^* = 0.1$ eV when the non-parabolicity is

included, and for the corresponding CB, the number is increased by a factor of ~ 3 . At $|\Delta E| = 0.5$ eV, the increase is as much as ~ 41 and ~ 8 times, respectively. This will have a strong impact on modeling band filling of especially holes for p-type CuIn_{1-x}Ga_xSe₂ materials.

In simulations and in analyses of measurements that involves free carrier concentrations, band filling of the energy bands is traditionally represented by the constant DOS mass (cf. Eq. (2)). This approach is valid for perfectly parabolic energy bands, but it is not an accurate description for CuIn_{1-x}Ga_xSe₂ with more complex energy dispersions (Figs. 1–3). In order to still use the traditional expression for

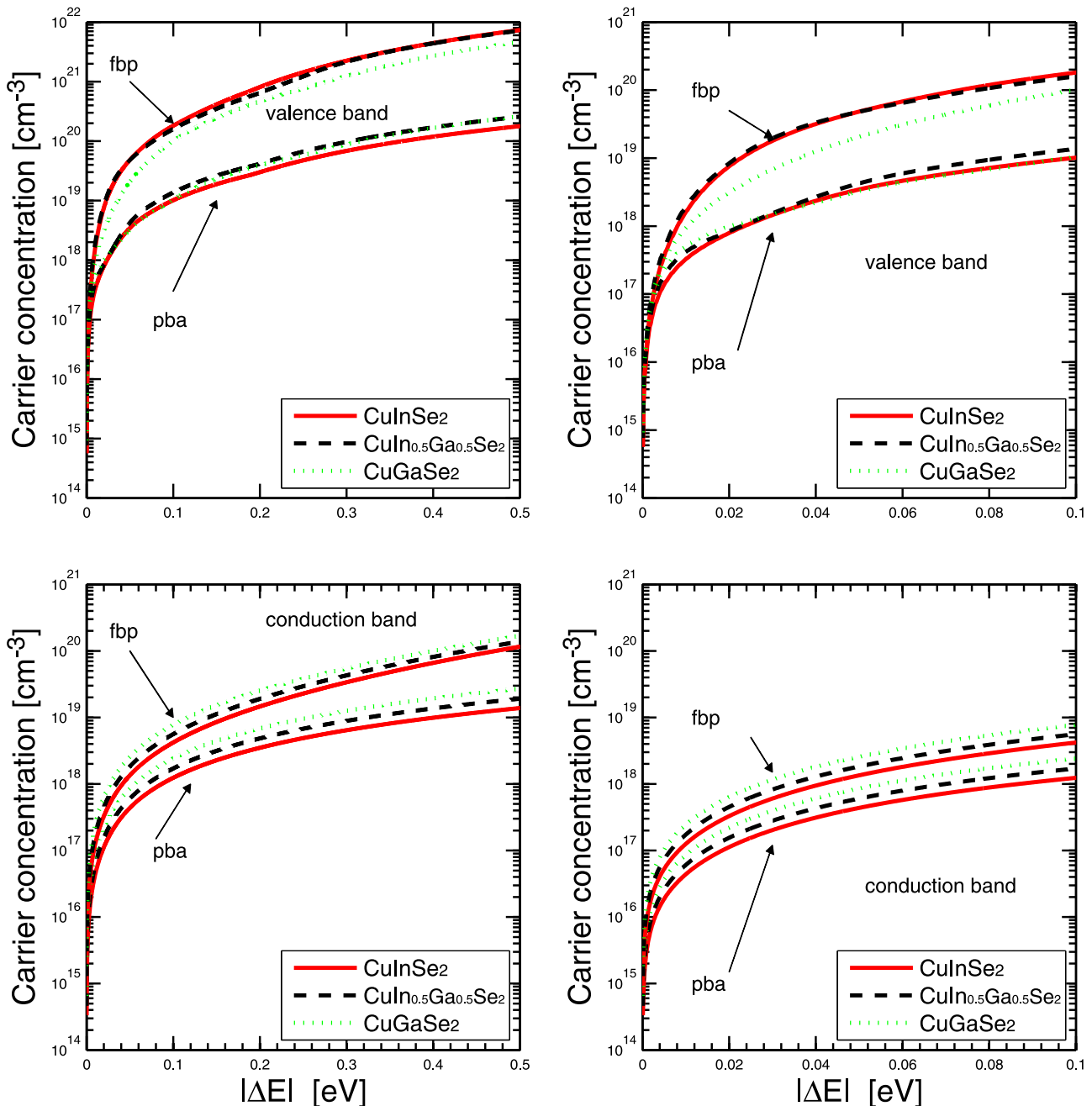


FIG. 5. Carrier concentration p or n as functions of the quasi-Fermi energy $E_{F,v}^*$ of the VBs and of the CB $E_{F,c}^*$. Left column shows the results for large energy scale up to 0.5 eV, and right column displays a close-up for small Fermi energies. In the figure, $|\Delta E|$ is the positive energy difference $E_{v1}(0) - E_{F,v}^*$ for the VBs and $E_{F,c}^* - E_{c1}(0)$ for the CB. The carrier concentrations consider external band filling in intrinsic materials at $T = 0$ K. The results demonstrate that the parabolic band approximation strongly underestimates the band filling of both the VBs and CB.

the DOS, we utilize the energy dependent DOS mass to model the DOS; see Eq. (3). The DOS masses for the $\text{CuIn}_{1-x}\text{Ga}_x\text{Se}_2$ (Fig. 6) show a very strong energy dependence of the VB DOS mass. This is directly related to the non-parabolicity and anisotropy of the VBS (cf. Fig. 2). For instance, the VB DOS masses in CuInSe_2 is $m_{v1}(E \approx 0) = (m_{v1}^\perp m_{v1}^\parallel)^{1/3} = 0.23m_0$ in the vicinity of the Γ -point. This mass increases to $\sim 1.00m_0$ when E is increased to ~ 0.1 eV. This may, therefore, explain the large measured hole masses $m_{v1} \approx 0.7m_0$ in CuInSe_2 (Refs. 23 and 24) and

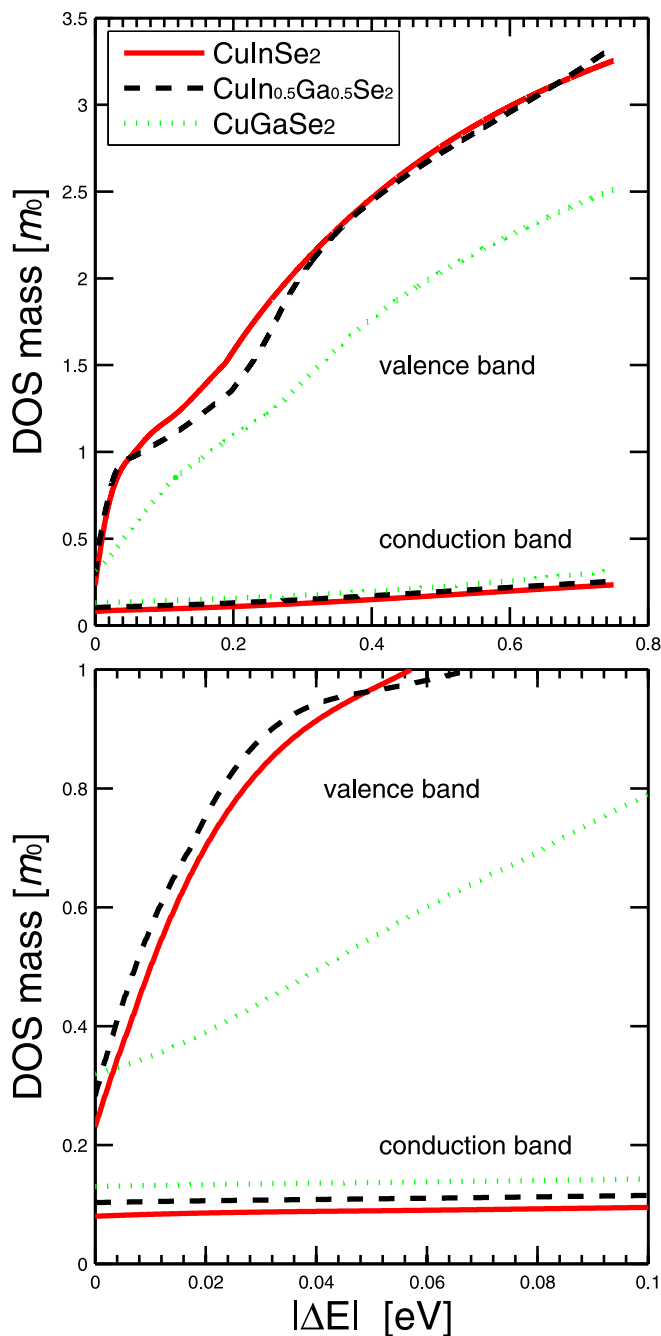


FIG. 6. The DOS mass $m_{v/c}^{DOS}(E)$ of the VBs and the CB in CuInSe_2 , $\text{CuIn}_{0.5}\text{Ga}_{0.5}\text{Se}_2$, and CuGaSe_2 . The upper (lower) panel shows $m_{v/c}^{DOS}(E)$ in a wider (narrower) energy region. This energy-dependent mass generates accurate quasi-Fermi energy $E_{F,v}^*$ and $E_{F,c}^*$ as function of the carrier concentration; see Eq. (3). $|\Delta E|$ is the energy difference $E_{v1}(0) - E_{F,v}^*$ for the VBs and $E_{F,c}^* - E_{c1}(0)$ for the CB; cf. Fig. 5.

$\sim 0.64m_0$ in CuGaSe_2 (Ref. 10) since indirect measurements normally involves high hole concentrations.

The absolute change in the CB DOS mass is small, but the relative increase is 2–3 times with respect to the Γ -point value: $m_c^{DOS}(|\Delta E| = 0) = 0.080m_0$, $0.103m_0$, and $0.130m_0$, whereas $m_c^{DOS}(|\Delta E| = 0.75 \text{ eV}) = 0.234m_0$, $0.255m_0$, and $0.316m_0$, for CuInSe_2 , $\text{CuIn}_{0.5}\text{Ga}_{0.5}\text{Se}_2$, and CuGaSe_2 , respectively.

B. Temperature dependent band gap and Fermi level

The temperature dependency of the band-gap energy $E_g(T)$ is in this work modeled by empirical temperature dependence²⁷

$$E_g(T) = E_g(0) - \frac{a \cdot T^2}{b + T}. \quad (7)$$

We use the experimental values for these parameters:^{27,28} $E_g(0) = 1.04 \text{ eV}$, $a = 1.086 \times 10^{-4} \text{ eV} \cdot \text{K}^{-1}$, $b = 97 \text{ K}$ for CuInSe_2 ; $E_g(0) = 1.67 \text{ eV}$, $a = 3 \times 10^{-4} \text{ eV} \cdot \text{K}^{-1}$, $b = 277 \text{ K}$ for CuGaSe_2 ; $E_g(0) = 1.33 \text{ eV}$, $a = 2.017 \times 10^{-4} \text{ eV} \cdot \text{K}^{-1}$ and $b = 209 \text{ K}$ for $\text{CuIn}_{0.5}\text{Ga}_{0.5}\text{Se}_2$. Here, the values of a and b for $\text{CuIn}_{0.5}\text{Ga}_{0.5}\text{Se}_2$ are estimated by averaging the data for CuInSe_2 and CuGaSe_2 .

The band gap and the Fermi level of intrinsic $\text{CuIn}_{1-x}\text{Ga}_x\text{Se}_2$ are presented in Fig. 7(a). At temperature $T \approx 0 \text{ K}$, the band gap is $E_g(0) = 1.04$, 1.33 , and 1.67 eV for $x = 0$, 0.5 , and 1 , respectively, and the Fermi level is exactly the mid-gap energy $E_F(0) = E_g(0)/2$. With increasing temperature, the band gap is decreased as a consequence of the second term in Eq. (7). The corresponding Fermi level changes only slightly with temperature, but for CuInSe_2 and $\text{CuIn}_{0.5}\text{Ga}_{0.5}\text{Se}_2$, the Fermi levels increase somewhat more compared with CuGaSe_2 . This is primarily due to the CB of DOS mass for CuGaSe_2 is almost the same, but the VB of DOS mass for CuGaSe_2 change smaller compared with CuInSe_2 and $\text{CuIn}_{0.5}\text{Ga}_{0.5}\text{Se}_2$ which will affect the DOS. As a consequence, the Fermi level is closer to the CB minimum in the In rich compounds. At $T = 300 \text{ K}$ and 600 K , the band-gap energies and Fermi energy are $E_g(300) = 1.02$, 1.29 , and 1.62 eV , $E_g(600) = 0.98$, 1.24 , and 1.55 eV , $E_F(300) = 0.55$, 0.69 , and 0.84 eV , and $E_F(600) = 0.59$, 0.71 , and 0.84 eV for $x = 0$, 0.5 , and 1 respectively. The largest effect is thus seen for the Ga rich compounds, however the temperature effect is rather moderate (Table I).

C. Carrier concentration

The free carrier concentration (Fig. 7(b)) of intrinsic $\text{CuIn}_{1-x}\text{Ga}_x\text{Se}_2$ is calculated by considering the temperature dependency of the band gaps in Eq. (7). For comparison, we present also the results for Si and GaAs assuming parabolic energy dispersion. With increasing temperature, the carrier concentration is increased considerably. For instance, an increase of the temperature from 300 K to 600 K implies $\sim 10^5$ times higher carrier concentration in CuInSe_2 . The small change in band gap and Fermi level as functions of temperature will have only small influence on the temperature dependence of carrier concentration. Instead, it is the temperature dependent Fermi distribution that governs the intrinsic carrier

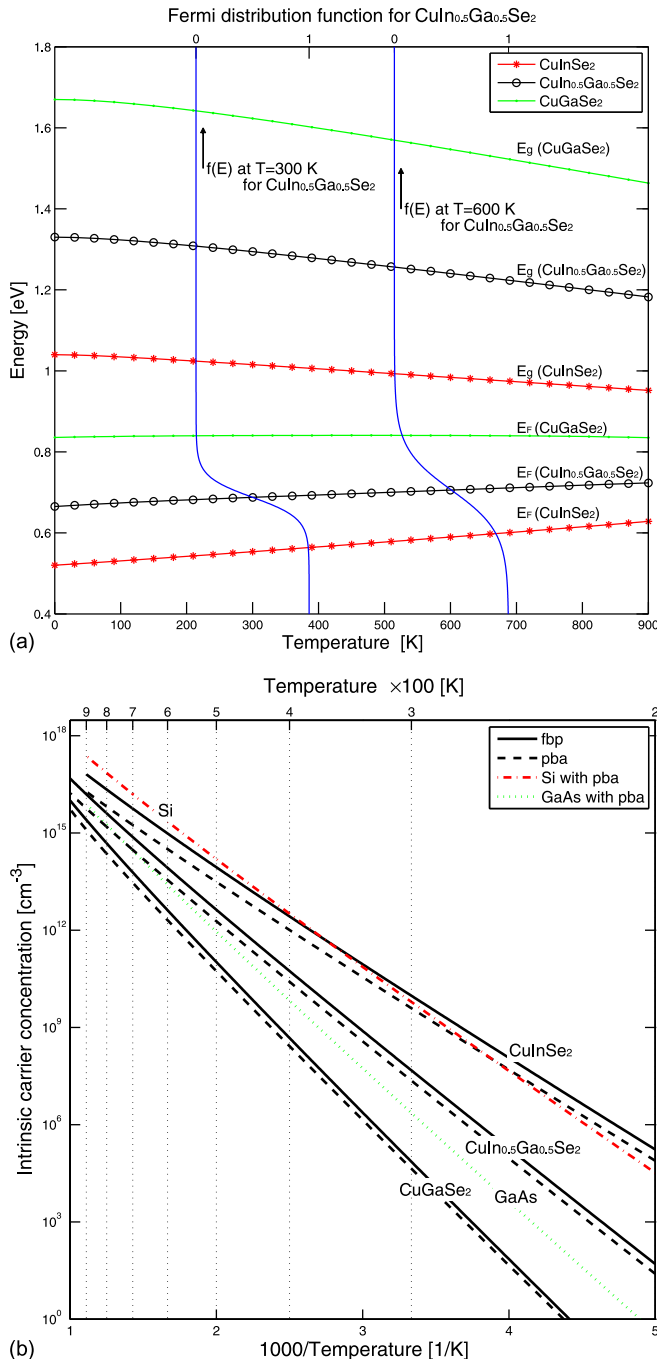


FIG. 7. (a) Band-gap energy E_g and Fermi energy E_F for $1 \leq T \leq 900\text{ K}$ of intrinsic CuInSe_2 , $\text{CuIn}_{0.5}\text{Ga}_{0.5}\text{Se}_2$, and CuGaSe_2 , determined from the full band parameterization. In this figure, we also present the Fermi distribution $f(E)$ of $\text{CuIn}_{0.5}\text{Ga}_{0.5}\text{Se}_2$ for $T = 300\text{ K}$ and 600 K . (b) Intrinsic carrier concentration as function of temperature. For comparison, the theoretical result for GaAs and Si using the parabolic band approximation is given.

concentration $n=p$ (see Fig. 7(b)). From the Fermi distribution of $\text{CuIn}_{0.5}\text{Ga}_{0.5}\text{Se}_2$, the probability of occupying the VB maximum (CB minimum) by a hole (an electron) is $\sim 3 \times 10^{-12}$ ($\sim 6 \times 10^{-11}$) at $T=300\text{ K}$. The corresponding probability at $T=600\text{ K}$ is $\sim 1 \times 10^{-6}$ ($\sim 3 \times 10^{-5}$), and this relative increase of $\sim 10^6$ is directly seen in the temperature dependent carrier concentration.

Generally, at the same temperature, In rich compounds with small band gaps have higher carrier concentration

TABLE I. Γ -point energy gaps E_g , Fermi energies E_F with respect to the VB maximum, and free carrier concentrations $n=p$ in intrinsic $\text{CuIn}_{1-x}\text{Ga}_x\text{Se}_2$ ($x=0$, 0.5, and 1) at temperature $T=300\text{ K}$. Corresponding Fermi energies E_F^P and hole concentrations p are presented in p -type $\text{CuIn}_{1-x}\text{Ga}_x\text{Se}_2$ with effective acceptor concentrations of $N_A=10^{17}$ and 10^{19} cm^{-3} . At $T \approx 0\text{ K}$, the band gap is $E_g=1.04$, 1.33, and 1.67 eV for $x=0$, 0.5, and 1, respectively.

	$\text{CuIn}_{1-x}\text{Ga}_x\text{Se}_2$		
	$x=0$	$x=0.5$	$x=1$
Intrinsic			
E_g [eV]	1.02	1.29	1.62
E_F [eV]	0.55	0.69	0.84
$n=p$ [cm^{-3}]	1×10^{10}	5×10^7	7×10^4
$N_A=10^{17}\text{ cm}^{-3}$			
E_F^P [eV]	0.138	0.137	0.126
p [cm^{-3}]	9×10^{16}	9×10^{16}	7×10^{16}
$N_A=10^{19}\text{ cm}^{-3}$			
E_F^P [eV]	0.046	0.058	0.047
p [cm^{-3}]	3×10^{18}	2×10^{18}	1×10^{18}

compared with CuGaSe_2 . This is due to a larger effect from the Fermi distribution function for materials with small energy gaps. One can notice from Fig. 7(b) that the free carrier concentration of CuInSe_2 (with the low-temperature band gap of $E_g=1.04\text{ eV}$) is comparable with that of Si (with a similar gap of $E_g=1.17\text{ eV}$). Also, the carrier concentration of GaAs (with $E_g=1.52\text{ eV}$) lies between the carrier concentrations of $\text{CuIn}_{0.5}\text{Ga}_{0.5}\text{Se}_2$ ($E_g=1.33\text{ eV}$) and CuGaSe_2 ($E_g=1.67\text{ eV}$). Thus, the free carrier concentration of the intrinsic materials is strongly correlated to the band-gap energy. However, also the energy dispersion of the bands affects the carrier concentration. Taking into account the non-parabolicity of the band, the free carrier concentration is increased by a factor of 2 to 3.

The free carrier concentration in the intrinsic compounds is too small to affect the device performance; for example, $n=p \approx 1 \times 10^{10}\text{ cm}^{-3}$ at 300 K and $3 \times 10^{12}\text{ cm}^{-3}$ at 400 K in CuInSe_2 , which has the smallest band gap. Thus, dopants/defects with low activation energies are required for activate the semiconductor material.

IV. RESULTS: p -TYPE $\text{CuIn}_{1-x}\text{Ga}_x\text{Se}_2$

The determination of the Fermi level in p -type $\text{CuIn}_{1-x}\text{Ga}_x\text{Se}_2$ alloys is based on the band dispersion of the intrinsic materials, and by considering that the two inequivalent and shallow acceptor levels (see Sec. II B) are uncompensated. In addition to the temperature dependent band-gap energies $E_g(T)$ in Eq. (7) of the intrinsic materials, we also include a defect-induced narrowing of the gap according to Ref. 19. The resulting defect and temperature dependent band gap is then

$$E_g^p(T, N_A) = E_g(T) + \Delta E_{c1}(N_A) - \Delta E_{v1}(N_A). \quad (8)$$

Here, $\Delta E_{c1}(N_A)$ and $\Delta E_{v1}(N_A)$ are the energy shifts of the Γ -point CB minimum and VB maximum, respectively, due to the present of ionized acceptors with the concentration

N_A . We use the parameterized values of the energy shifts for p -type $\text{CuIn}_{1-x}\text{Ga}_x\text{Se}_2$ ($x = 0, 0.5$, and 1) from Ref. 19

$$\begin{aligned}\Delta E_{c1}(N_A) &= A_{c1}(N_A/10^{18})^{1/2} + B_{c1}(N_A/10^{18})^{1/4} \\ \Delta E_{v1}(N_A) &= A_{v1}(N_A/10^{18})^{1/2} + B_{v1}(N_A/10^{18})^{1/4} \\ &\quad + C_{v1}(N_A/10^{18})^{1/3}.\end{aligned}\quad (9)$$

We use parameters from Ref. 19: $A_{c1} = -0.27, -0.52$, and -0.44 eV, $B_{c1} = -10.72, -11.42$, and -14.64 eV, $A_{v1} = 7.16, 20.87$, and 13.26 eV, $B_{v1} = 40.71, 69.23$, and 38.40 eV, and $C_{v1} = -25.11, -67.11$, and -26.66 eV, for $x = 0, 0.5$, and 1 , respectively. Apart from this acceptor-induced band-gap narrowing, we assume no effect on the host energy bands due to the presence of the shallow acceptors, although it is known that very high hole concentrations can affect the band dispersion²⁹ (still, the effective masses at the Fermi energy is almost unaffected).

A. Temperature dependent band gap and Fermi level

The calculated Fermi level E_F^P in p -type materials is presented in Fig. 8, referred to the Fermi level of the intrinsic materials E_F from Fig. 7(a). Only at very high temperatures ($T > 400$ K) and for low acceptor concentrations, the Fermi level of p -type $\text{CuIn}_{1-x}\text{Ga}_x\text{Se}_2$ will reach the Fermi level of corresponding intrinsic compounds. Moreover, although the different compounds have comparable acceptor ionization energies, the Ga rich alloy has lower relative Fermi level; this is a direct consequence of the larger band gap of the Ga rich alloy.

By comparing the calculations with the parabolic band approximation (dotted lines in Fig. 8) and the full band approach (solid lines) for each of the three $\text{CuIn}_{1-x}\text{Ga}_x\text{Se}_2$ alloys, one can notice that the Femi level is similar for the two models only at low and at very high temperatures. In the mid-temperature region the difference is however apparent, especially for the high acceptor concentrations. Assuming parabolic bands yields always a lower Fermi level. The reason for this effect is that the energy dependent effective mass $m_{v/c}^{DOS}(E)$ in the full band parameterization is always larger than the corresponding Γ -point mass. Although the effect on the absolute value of the Fermi level seems to be small, it

has an impact on the free carrier concentrations for highly doped materials.

B. Carrier concentration

The free carrier concentrations of p -type $\text{CuIn}_{1-x}\text{Ga}_x\text{Se}_2$ as functions of temperature and acceptor concentration are presented in Fig. 9. The carrier concentration can be divided into three regions: the freeze-out region for low temperatures, the extrinsic region in the mid-temperature region, and the intrinsic region at sufficiently high temperatures. For example, consider CuInSe_2 with the acceptor concentration $N_A = 10^{13}$ cm⁻³ in Fig. 9. At very low temperatures ($T < 100$ K), part of the host electrons are excited to the acceptor-like states whereas remaining host electrons are “frozen.” With an increase of the temperature, more and more electrons in the VBs are thermally excited, until all acceptor states are occupied. The calculated concentrations in this region are in fairly good agreement with experimental carrier concentrations from low-temperature Hall mobility measurements by Schroeder *et al.*⁹ Both the calculated and measured data indicate that the freeze-out region is as high as room-temperature even for moderately doped CuInSe_2 ($N_A \approx 10^{17}-10^{18}$ cm⁻³).

With a further increase of the temperature, the free carrier concentration will be constant for a wide temperature range; this is the extrinsic region. When the temperature is increase even further, the free carrier concentration will be enhanced due to electron excitation across the band gap as for the intrinsic materials.

From the figure, one can observe that the transition from the freeze-out region to the extrinsic region occurs well below the room temperature unless the uncompensated acceptor concentration is above $\sim 10^{18}$ cm⁻³. Due to the slightly lower ionization energies for the In rich compounds, these compounds have lower temperature for the transition to the extrinsic region. For high uncompensated acceptor concentrations (i.e., $> 10^{18}$ cm⁻³), not all acceptors are ionized at room temperature (see Table I). Moreover, since the In rich compounds also have smaller band gaps, the transition from the extrinsic region to the intrinsic region occurs at lower temperatures for these compounds.

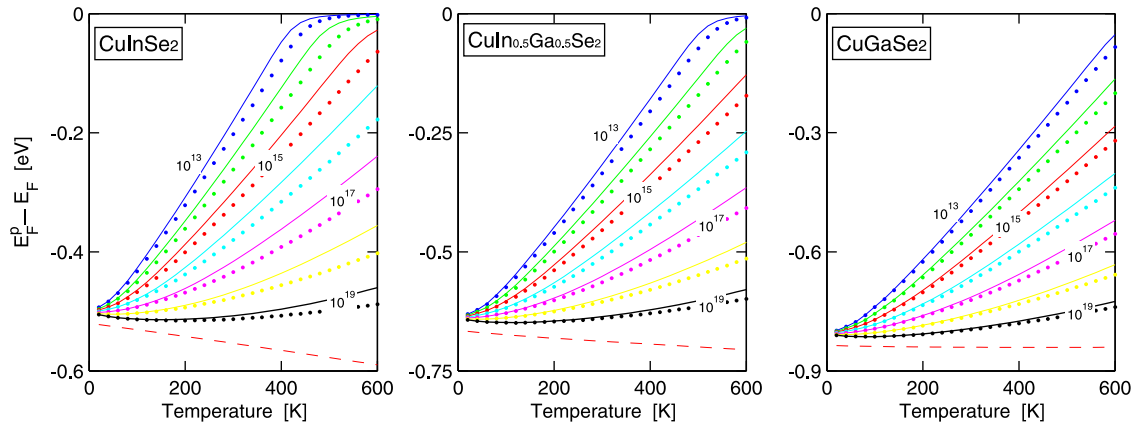


FIG. 8. Fermi level as function of the temperature $20 \leq T \leq 600$ of p -type CuInSe_2 , $\text{CuIn}_{0.5}\text{Ga}_{0.5}\text{Se}_2$, and CuGaSe_2 for the effective doping concentration $N_A = 10^{13}, 10^{14}, 10^{15}, \dots$, and 10^{19} acceptors/cm³. The energy scale $E_F^P - E_F$ describes the Fermi energy with respect to the intrinsic E_F ; see Fig. 7. Dashed lines represent the VBM with respect to the intrinsic Fermi level. Solid and dotted lines represents the full band parameterization and the parabolic band approximation, respectively.

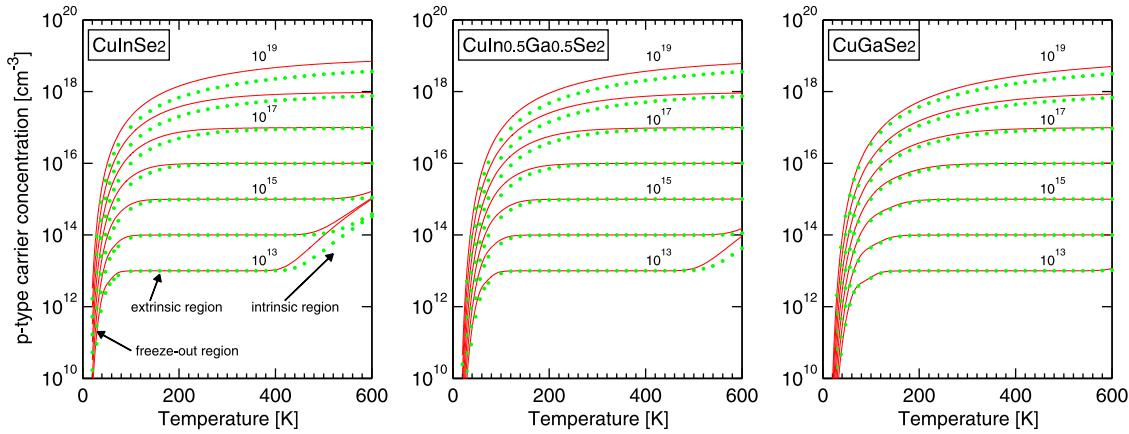


FIG. 9. Free carrier concentration as function of the temperature in *p*-type CuInSe₂, CuIn_{0.5}Ga_{0.5}Se₂, and CuGaSe₂ for the effective doping concentration $N_A = 10^{13}, 10^{14}, 10^{15}, \dots$, and 10^{19} acceptors/cm³. Solid and dotted lines represents the full band parameterization and the parabolic band approximation, respectively. The full band description of the energy dispersion is important for high doping concentrations and/or in the intrinsic region for cross-gap excitations at high temperatures.

The intrinsic region is however only important for very low acceptor concentrations.

By comparing the results from the parabolic band approximation and from the full band parameterization for each compound, one can observe that the approximation underestimates the free carrier concentrations roughly by a factor of 2 in both the freeze-out region and also in the intrinsic regions. Due to this underestimate, the transition from freeze-out to extrinsic regions tends to occur at a somewhat higher temperature for the approximated method, and also the transition from the extrinsic to the intrinsic region also at a somewhat higher temperature. Although the carrier concentration is fully described in the extrinsic region by assuming parabolic bands since all acceptors are ionized, the Fermi level is not well described within this approximation (see Fig. 8). Thus, in order accurately describe the free carrier concentration as well as its temperature dependency, a full description of the energy dispersions is needed.

V. SUMMARY

To summarize, we have analyzed the energy band dispersion and the carrier concentration in chalcopyrite CuIn_{1-x}Ga_xSe₂ ($x = 0, 0.5$, and 1) alloys. The overall results are: (i) the three uppermost VBs are strongly anisotropic and non-parabolic. (ii) The lowest CB becomes non-parabolic for energies 50–100 meV above the Γ -point band minimum. (iii) A constant DOS mass cannot accurately describe band filling of the VBs even at low hole concentrations. Instead, we introduce an energy dependent DOS mass that can be utilized to describe the carrier concentration and the Fermi energy using traditional equations for the DOS. (iv) With the full description of the energy dispersion, the hole concentration is improved by a factor of 10–50 and the electron concentration is improved by a factor of 2–10 depending on quasi-Fermi energy. (v) The transition from the freeze-out region to the extrinsic region occurs well below the room temperature for uncompensated acceptor concentration below $\sim 10^{17}$ cm⁻³, whereas for higher concentrations, not all acceptors are ionized at $T = 300$ K.

Thus, with a more correct description of the energy dispersions, one can better analyze the electron and hole dynamics in the CuIn_{1-x}Ga_xSe₂ alloys, thereby better understand the electrical properties of these compounds.

ACKNOWLEDGMENTS

This work is supported by the China Scholarship Council, the Swedish Energy Agency, and the Swedish Research Council. We acknowledge access to high-performance computing resources at the NSC and HPC2N centers through SNIC/SNAC and Matter network.

- ¹M. D. Archer and R. Hill, *Clean Electricity from Photovoltaics* (Imperial, London, 2001).
- ²V. Nadenau, U. Rau, and H. W. Schock, *J. Appl. Phys.* **87**, 584 (2000); A. Jasenek, U. Rau, V. Nadenau, and H. W. Schock, *J. Appl. Phys.* **87**, 594 (2000).
- ³S. R. Kodigala, *Cu(In_{1-x}Ga_x)Se₂ Based Thin Film Solar Cells* (Elsevier, Burlington, MA, 2010), Vol. 35.
- ⁴R. Noufi, R. Axton, C. Herrington, and S. K. Deb, *Appl. Phys. Lett.* **45**, 668 (1984).
- ⁵S. Ishizuka, H. Shibata, A. Yomada, P. Fons, K. Sakurai, K. Matsubara, S. Niki, M. Yonemura, and H. Nakanishi, *J. Appl. Phys.* **100**, 096106 (2006).
- ⁶Y.-J. Zhao, C. Persson, S. Lany, and A. Zunger, *Appl. Phys. Lett.* **85**, 5860 (2004).
- ⁷I. Mártil, J. Santamaría, G. Gonzalez-Díaz, and F. Sanchez-Quesada, *J. Appl. Phys.* **68**, 189 (1990).
- ⁸E. Arushanov, S. Siebentritt, T. Schedel-Niedrig, and M. C. Lux-Steiner, *J. Appl. Phys.* **100**, 063715 (2006).
- ⁹D. J. Schroeder, J. L. Hernandez, G. D. Berry, and A. A. Rockett, *J. Appl. Phys.* **83**, 1519 (1998).
- ¹⁰F. Luckert, M. V. Yakushev, C. Faugeras, A. V. Karotki, A. V. Mudryi, and R. W. Martin, *Appl. Phys. Lett.* **97**, 162101 (2010).
- ¹¹M. A. Mannan, M. S. Anjan, and M. Z. Kabir, *Solid-State Electron.* **63**, 49 (2011).
- ¹²S. A. Dinca, E. A. Schiff, B. Egaas, R. Noufi, D. L. Young, and W. N. Shafarman, *Phys. Rev. B* **80**, 235201 (2009).
- ¹³S. H. Han, F. S. Hasoon, A. M. Hermann, and D. H. Levi, *Appl. Phys. Lett.* **91**, 021904 (2007).
- ¹⁴A. Hofmann and C. Pettenkofer, *Phys. Rev. B* **84**, 115109 (2011).
- ¹⁵R. Chen and C. Persson, *Thin Solid Films* **519**, 7503 (2011).
- ¹⁶J. M. Luttinger and W. Kohn, *Phys. Rev.* **97**, 869 (1955); G. Dresselhaus, A. F. Kip and C. Kittel, *Phys. Rev.* **98**, 368 (1955); E. O. Kane, *J. Phys. Chem. Solids* **1**, 82 (1956).
- ¹⁷S. Siebentritt, M. Igalsen, C. Persson, and S. Lany, *Prog. Photovolt: Res. Appl.* **18**, 390 (2010).

- ¹⁸C. Persson, *Appl. Phys. Lett.* **93**, 072106 (2008).
- ¹⁹C. Persson, *Thin Solid Films* **517**, 2374 (2009).
- ²⁰S. M. Sze, *Semiconductor Devices: Physics and Technology*, 2nd ed. (Wiley, Toronto, 2002).
- ²¹M. I. Alonso, K. Wakita, J. Pascual, M. Garriga, and N. Yamamoto, *Phys. Rev. B* **63**, 075203 (2001); N. K. Hönes, M. Eickenberg, S. Siebentritt, and C. Persson, *Appl. Phys. Lett.* **93**, 092102 (2008); S.-H. Han, C. Persson, F. S. Hasoon, H. Al-Thani, A. M. Hermann, and D. Levi, *Phys. Rev. B* **74**, 085212 (2006).
- ²²See supplementary material at <http://dx.doi.org/10.1063/1.4767120> for constant energy surfaces in CuInSe₂, CuIn_{0.5}Ga_{0.5}Se₂, and CuGaSe₂.
- ²³N. N. Syrbu, I. M. Tigranyan, L. L. Nemerenco, V. V. Ursaki, V. E. Tezlevan, and V. V. Zalamai, *J. Phys. Chem. Solids* **66**, 1974 (2005).
- ²⁴H. Neumann, W. Kissinger, H. Sobotta, V. Riede, and G. Kühn, *Phys. Status Solidi B* **108**, 483 (1981).
- ²⁵H. Weinert, H. Neumann, H.-J. Höbler, G. Kühn, and N. van Nam, *Phys. Status Solidi B* **81**, K59 (1977).
- ²⁶E. Arushanov, L. Essaleh, J. Galibert, J. Leotin, M. A. Arsene, J. P. Peyrade, and S. Askenazy, *Appl. Phys. Lett.* **61**, 958 (1992).
- ²⁷*Landolt-Börnstein: Numerical Data and Functional Relationships in Science and Technology*, edited by O. Madelung *et al.*, New Series, Group III, Vol. 17h (Springer, Berlin, 1985).
- ²⁸H. Neumann, W. Hörig, E. Reccius, W. Möller, and G. Kühn, *Solid State Commun.* **27**, 449 (1978).
- ²⁹C. Persson, B. E. Sernelius, A. Ferreira da Silva, R. Ahuja, and B. Johansson, *J. Phys. Condens. Matter* **13**, 8915 (2001).

5.3 Paper III: "Dielectric function spectra at 40 K and critical-point energies for CuIn_{0.7}Ga_{0.3}Se₂"

S.G. Choi, R. Chen, C. Persson, T.J. Kim, S.Y. Hwang, Y. D. Kim, and L. M. Mansfield, *Applied Physics Letters* **101**, 261903 (2012).

Dielectric function spectra at 40 K and critical-point energies for CuIn_{0.7}Ga_{0.3}Se₂

S. G. Choi,^{1,a)} R. Chen,² C. Persson,^{2,3} T. J. Kim,⁴ S. Y. Hwang,⁴ Y. D. Kim,⁴ and L. M. Mansfield¹

¹National Renewable Energy Laboratory, Golden, Colorado 80401, USA

²Department of Materials Science and Engineering, Royal Institute of Technology, SE-100 44 Stockholm, Sweden

³Department of Physics, University of Oslo, NO-0316 Oslo, Norway

⁴Department of Physics, Kyung Hee University, Seoul 130-701, South Korea

(Received 20 September 2012; accepted 6 December 2012; published online 26 December 2012)

We report ellipsometrically determined dielectric function ϵ spectra for CuIn_{0.7}Ga_{0.3}Se₂ thin film at 40 and 300 K. The data exhibit numerous spectral features associated with interband critical points (CPs) in the spectral range from 0.74 to 6.43 eV. The second-energy-derivatives of ϵ further reveal a total of twelve above-bandgap CP features, whose energies are obtained accurately by a standard lineshape analysis. The ϵ spectra determined by ellipsometry show a good agreement with the results of full-potential linearized augmented plane wave calculations. Probable electronic origins of the CP features observed are discussed. © 2012 American Institute of Physics.

[<http://dx.doi.org/10.1063/1.4773362>]

CuIn_{1-x}Ga_xSe₂ is so far the most promising thin-film photovoltaic (PV) material and its best cell efficiency has been recorded as high as 20.3%.¹ The production capacity of CuIn_{1-x}Ga_xSe₂ solar cells was 426 MW in 2010 and is now approaching gigawatt-scale.² For design and optimization of high-efficiency PV device structures, accurate knowledge of the optical response for absorber materials is of great importance.³ In the course of exploring CuIn_{1-x}Ga_xSe₂ for PV device applications, its optical properties were well characterized.^{4,5}

Spectroscopic ellipsometry (SE)⁶ is known to be a highly suitable method of determining a material's optical functions such as complex dielectric function $\epsilon = \epsilon_1 + i\epsilon_2$ and complex refractive index $N = n + ik$ over a wide spectral range. Therefore, SE has been widely used to characterize various semiconductors.⁷ For CuIn_{1-x}Ga_xSe₂, SE has been employed to study the composition-dependence of ϵ and interband critical-point (CP) energies,^{8–10} effects of Cu-deficiency on the optical properties,¹¹ and thin-film growth mechanisms.¹²

The optical information of materials at low temperature, where the thermal broadening of optical transitions is reduced and individual optical structures are better resolved, plays an important role in understanding the material's electronic structure. Hence, the ϵ spectra for many elemental^{13,14} and compound semiconductors^{15–17} have been determined by SE at low temperature. However, low-temperature SE study of CuIn_{1-x}Ga_xSe₂ is rare despite the availability of rich information on its room-temperature optical properties.

Here, we apply SE to determine the ϵ spectra of CuIn_{0.7}Ga_{0.3}Se₂ at 40 K, a composition for high-performance CuIn_{1-x}Ga_xSe₂ PV devices. The SE data are in a good agreement with the ϵ spectra of CuIn_{0.5}Ga_{0.5}Se₂ calculated by the full-potential linearized augmented plane wave (FPLAPW) method using the generalized gradient approximation (GGA)

plus an onsite Coulomb interaction U of the Cu d states.⁴ The above-bandgap CP energies are obtained from a standard lineshape analysis of SE data. We discuss the probable electronic origins of the observed CP features.

A polycrystalline CuIn_{0.7}Ga_{0.3}Se₂ thin film was grown at 600 °C by a single-stage thermal co-evaporation method, where the fluxes of Cu, In, Ga, and Se were kept at constant during the deposition and thus the compositional homogeneity is greatly improved along the growth direction.¹⁸ Ga and In fluxes were maintained at the Ga/(Ga+In) ratio of 0.3, and the atomic Cu ratio Cu/(Ga+In) was approximately 0.87. Soda-lime glass coated with an approximately 1-μm-thick molybdenum (Mo) film was used as the substrate. The nominal thickness of CuIn_{0.7}Ga_{0.3}Se₂ thin film was 1.5 μm. Chemical composition of the grown film was determined by X-ray fluorescence.

SE data were collected from 0.74 to 6.43 eV using a dual-rotating-compensators type system (J.A. Woollam Inc., RC-2 model) equipped with a variable-temperature cryostat. The angle of incidence is 68°. We reduced the microscopic roughness of CuIn_{0.7}Ga_{0.3}Se₂ film by chemical-mechanical polishing of the surface using a colloidal silica suspension with 0.02-μm particles.

The ϵ spectra for CuIn_{0.7}Ga_{0.3}Se₂ are obtained by the multilayer analysis of the SE data.¹⁹ The multilayer model consists of the ambient, a surface roughness layer, the CuIn_{0.7}Ga_{0.3}Se₂ layer, and the Mo layer. The glass substrate is not included in the model because its presence is completely obscured by the metallic Mo layer in the spectral range used for this study. We estimate the surface-roughness layer to be ~2.2 nm thick, and modeled its response as a Bruggeman effective-medium-approximation²⁰ 50–50 mixture of the CuIn_{0.7}Ga_{0.3}Se₂ layer and void. The ϵ spectra for CuIn_{0.7}Ga_{0.3}Se₂ layer were reconstructed by the B-spline formulation.²¹

Real (ϵ_1) and imaginary (ϵ_2) parts of the modeled ϵ spectra for CuIn_{0.7}Ga_{0.3}Se₂ taken at 40 and 300 K are given in

^{a)}Author to whom correspondence should be addressed. Electronic mail: sukgeun.choi@nrel.gov.

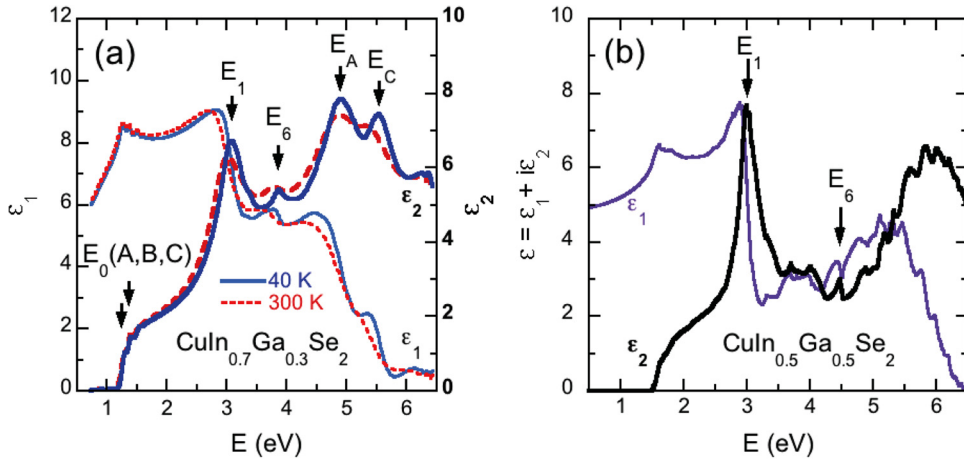


Fig. 1(a). For both temperatures, the optical structures associated with the E_1 , E_6 , E_A , and E_C interband CPs are clearly seen in the ε_2 spectra at around 3.0, 3.8, 4.8, and 5.5 eV. In the 40 K spectra, however, the CP features are better resolved and their energies increase slightly from those in the 300 K data. For example, the E_C CP feature at ~ 5.5 eV is seen only as a weak shoulder in the ε_2 spectra at 300 K, but it appears as a distinct peak in the 40 K data. We note that Alonso *et al.*⁹ identified the electronic origins of the CP features observed in their room-temperature SE data based on the results from density functional theory calculations done by Jaffe and Zunger.²² The E_1 , E_6 , and E_A CPs in our data may correspond to the $E_1(A)$, $E_1(B)$, and $E_2(A)$ CPs in Ref. 9.

The overall shape of the SE-determined ε data shows a good agreement with the averaged $\varepsilon = [2\varepsilon_\perp + \varepsilon_\parallel]/3$ spectrum for $\text{CuIn}_{0.5}\text{Ga}_{0.5}\text{Se}_2$ calculated by the FPLAPW method with the GGA+U potential that is presented in Fig. 1(b). The ordinary (ε_\perp) and extraordinary (ε_\parallel) components of the ε were calculated in our previous work.⁴ It appears that the theory slightly underestimates the CP energies below 4 eV, but overestimates those above 4 eV. Although the Ga/(Ga+In) ratio x for the experimental data ($x=0.3$) and calculated spectrum ($x=0.5$) are different, our calculations suggest⁴ that no significant difference in the optical properties is anticipated between those two close compositions, other than the shift of CP energies. This is also evidenced by the similarities in the calculated ε spectrum and the CP features between $\text{CuIn}_{0.5}\text{Ga}_{0.5}\text{Se}_2$ and CuInSe_2 .⁴

For the analyses of the observed CP features, we numerically calculated second-energy-derivatives of the pseudodielectric function⁶ $\langle \varepsilon \rangle$ data using a Savitzky-Golay type²³ linear-filtering algorithm. The CP energies are obtained by assuming the standard analytic CP expressions^{24,25} for the lineshapes and then fitting them to the data by least squares schemes. Details of the lineshape analysis procedures can be found elsewhere.^{13–16}

The lineshape analysis for the 40 K data is presented in Fig. 2. A total of twelve lineshapes were needed to analyze the data from 2.5 to 6.4 eV. The majority of the CP features are fit best with the two-dimensional lineshapes, whereas the E_2 , E_6 , E_B CPs are better represented by the excitonic lineshapes and the E_D CP is by the three-dimensional lineshape. Both real and imaginary parts are fit simultaneously. Similar fit quality was achieved for the 300 K data (not shown). The

FIG. 1. (a) Modeled ε_1 and ε_2 spectra for $\text{CuIn}_{0.7}\text{Ga}_{0.3}\text{Se}_2$ taken at 40 K (solid blue lines) and 300 K (dashed red lines). Four prominent above-bandgap CP features are indicated by arrows, which are labeled in the numeric and alphabetic order. (b) The ε spectra for $\text{CuIn}_{0.5}\text{Ga}_{0.5}\text{Se}_2$ calculated by the FPLAPW using the GGA + U. The major CP features corresponding to the SE results are identified.

fit-determined CP energies are listed in Table I. For comparison, the CP energies for various $\text{CuIn}_{1-x}\text{Ga}_x\text{Se}_2$ previously reported^{8–10,12} are also included. Although Alonso *et al.*⁹ observed the $E(\Gamma\chi)$ CP at ~ 2.4 eV for $\text{CuIn}_{0.6}\text{Ga}_{0.4}\text{Se}_2$, our data do not resolve this CP. We note, however, that we probed two additional CPs E_2 and E_4 , which have not been seen in previous room-temperature SE studies.^{8–10,12}

The electronic origins of each CP are examined based on the results from the FPLAPW calculations. First, we identify the different contributions to ε_2 in terms of the transitions between the valence bands v_i and the conduction bands c_j . Here, the v_1 and c_1 denote the highest valence band and lowest conduction band, respectively. This contribution is labeled as $v_1 \leftrightarrow c_1$ in Fig. 3. As expected,^{8,9} the E_0 CPs in the low-energy region are associated with the transitions from v_1 to c_1 near the Γ (0, 0, 0) point of the Brillouin zone (BZ). A broad optical structure in the ε_2 spectrum spanning from 5 to 7 eV is composed of several contributions from the low-lying valence bands. Therefore, unambiguous identification of the major contributions to the CP features in the high-energy region is very difficult.

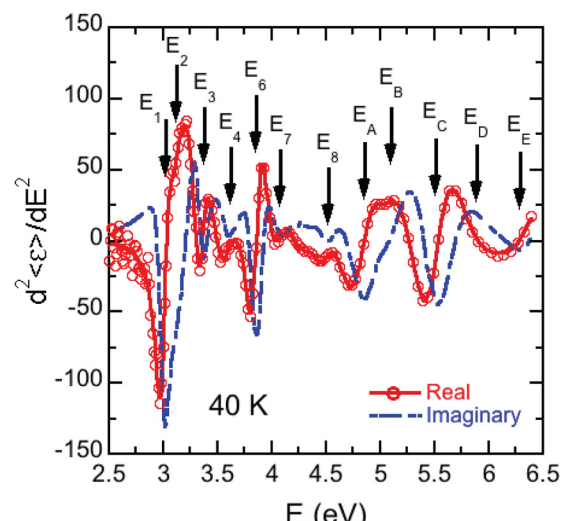


FIG. 2. (a) Solid red are standard CP lineshapes best fit to $d^2\langle \varepsilon_1 \rangle / dE^2$ (open circles) and dashed-dotted blue lines are $d^2\langle \varepsilon_2 \rangle / dE^2$. For clarity, only half the data points are shown and the $d^2\langle \varepsilon_2 \rangle / dE^2$ are not displayed. Energies of each CP are indicated by arrows and labeled in a numeric and alphabetic order.

TABLE I. CP energies in eV for $\text{CuIn}_{0.7}\text{Ga}_{0.3}\text{Se}_2$ at 40 and 300 K. Previously reported CP energies for various $\text{CuIn}_{1-x}\text{Ga}_x\text{Se}_2$ are also included for comparison.

This work $x=0.5$ (Theory)	This work $x=0.3$ (40 K)	This work $x=0.3$ (300 K)	Ref. 12 $x=0.0$ (300 K)	Ref. 8 $x=0.0$ (300 K)	Ref. 8 $x=1.0$ (300 K)	Ref. 9 $x=0.4$ (300 K)	Ref. 10 $x=0.3$ (300 K)
$E_0(\text{A},\text{B})$	1.48, 1.50	1.33 ^a	1.21 ^a	1.02	1.040, 1.039	1.648, 1.717	1.22, 1.25
$E_0(\text{C})$	1.68	1.46 ^a	1.44 ^a	1.22	1.274	1.92	1.47
					2.4	2.8	~2.38
E_1	3	2.998 ± 0.002	2.883 ± 0.015	2.84	2.821/2.901	3.127/3.247	~2.9
E_2	3.09	3.156 ± 0.006	2.997 ± 0.032				
E_3	3.32	3.342 ± 0.002	3.228 ± 0.003	3.21	3.174	3.501	~3.25
E_4	3.69	3.548 ± 0.008	3.472 ± 0.001				3.302
E_5	4.02						
E_6	4.47	3.858 ± 0.001	3.755 ± 0.017	3.65	3.635/3.626	4.049/4.03	~3.7
E_7	4.85	4.192 ± 0.011	4.086 ± 0.185	4.11	4.07	4.49	~4.0
E_8	5.17	4.504 ± 0.010	4.363 ± 0.062	4.18	4.21		~4.3
E_{A}		4.836 ± 0.011	4.760 ± 0.102	4.56	4.71	4.89	~4.7
E_{B}		5.120 ± 0.023	5.096 ± 0.374	4.81	4.84	5.1	~5.0
E_{C}		5.486 ± 0.008	5.317 ± 0.107	5.11			
E_{D}		5.857 ± 0.040	5.872 ± 0.086	5.41			
E_{E}		6.467 ± 0.023	6.419 ± 0.013	5.91			

^aThe $E_0(\text{A},\text{B})$ and $E_0(\text{C})$ energies estimated from the modeled ε_2 spectra.

Second, we analyze the k -dependence of the CPs along the main symmetry directions, which is depicted in Fig. 4. The pronounced E_1 CP originates from the $v_1 \rightarrow c_1$ transitions near the P ($1/2, 1/2, 1/2$) point of the BZ (in the conventional coordinates). This is consistent with the results from room-temperature SE studies by Alonso *et al.*,^{8,9} where this CP is assigned to the $E_1(\text{A})$ CP. We observed a small doublet

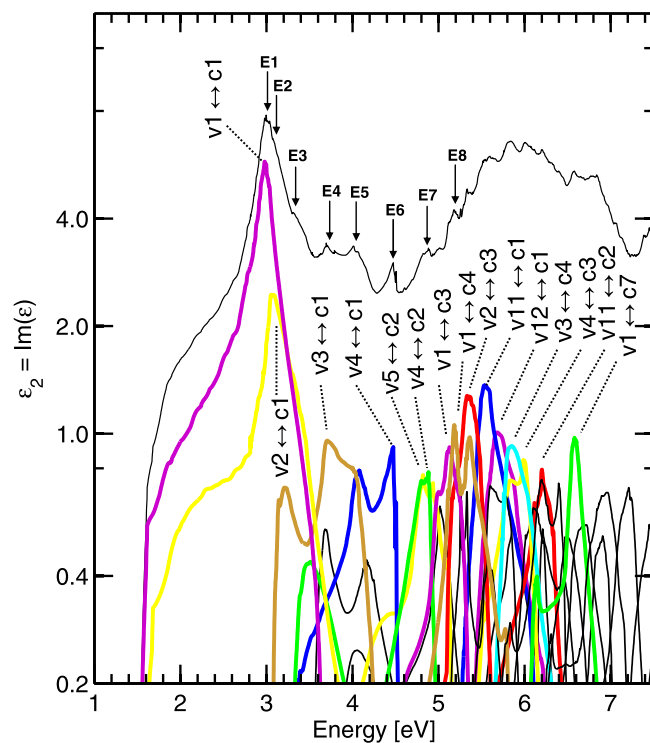
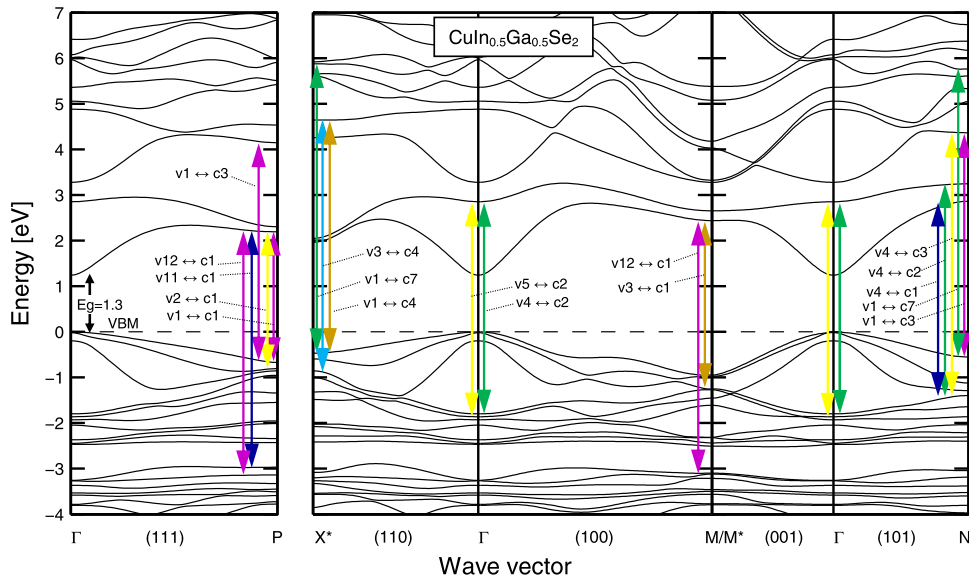


FIG. 3. Band-to-band analysis of the contribution to the total ε_2 spectrum (thin black trace). The most important valence-to-conduction band transitions ($v_i \rightarrow c_j$) are marked by thick colored curves. Spin-orbit interaction is included, and the band-to-band transitions involve a summation of the spin up and down contributions. Note: The vertical axis ε_2 is in the log scale.

structure in the E_1 peak arising from the spin-orbit split. The E_2 and E_3 CPs involve transitions from the second valence band, $v_2 \rightarrow c_1$. This band-to-band transition generates two structures in ε_2 , where the main peak is associated with transitions at the P-point as for the E_1 CP. In $\text{CuIn}_{0.5}\text{Ga}_{0.5}\text{Se}_2$, the E_2 and E_3 peaks modify only slightly the main ε_2 spectrum around 3.2 eV. However, the calculations for CuInSe_2 reveal that the E_2 and E_3 CPs occur 0.1–0.2 eV higher than the E_1 CP, and appear as distinct spectral features. Thus, the observation of E_2 and E_3 CPs in $\text{CuIn}_{0.7}\text{Ga}_{0.3}\text{Se}_2$ is anticipated. The E_4 CP originates from the $v_3 \rightarrow c_1$ transitions at the M ($1, 0, 0$) = M^* ($0, 0, 1$) point. The E_5 CP is mainly attributed to the transition to $v_4 \rightarrow c_1$ at the N ($1/2, 0, 1/2$) point, but the $v_3 \rightarrow c_1$ transitions at the M/ M^* points also contribute to this CP feature. This E_5 CP can be understood as the $E_1(\text{B})$ CP in previous SE studies.^{8,9} The E_6 CP feature is a result of the $v_4 \rightarrow c_1$ transition at the N point. The E_7 CP corresponds to the $v_4 \rightarrow c_2$ transitions at the Γ ($0, 0, 0$) and N point, and the $v_5 \rightarrow c_2$ transitions at the Γ point. The E_{A} , another prominent CP feature equivalent to the $E_2(\text{A})$ CP in Refs. 8 and 9, also has multiple contributions from the various symmetric points of BZ: The $v_1 \rightarrow c_4$ transitions at the X^* ($1/2, 1/2, 0$) point of the BZ, and the $v_1 \rightarrow c_3$ transitions at the N and P points. We conjecture that the $v_{11} \rightarrow c_1$ and $v_{12} \rightarrow c_1$ transitions near the P point of BZ are the major contributions to the E_{C} CP. Although this CP has not been discussed in previous SE studies^{8,9} of $\text{CuIn}_{1-x}\text{Ga}_x\text{Se}_2$ probably due to their limit on the spectral range, a recent real-time SE study¹² of CuInSe_2 observed a similar structure at 5.11 eV without identification of its electronic origin.

Our calculations suggest that the energy differences in the E_0 transitions are $E_0(\text{B}) - E_0(\text{A}) = 0.02$ eV and $E_0(\text{C}) - E_0(\text{A}) = 0.20$ eV for $\text{CuIn}_{0.5}\text{Ga}_{0.5}\text{Se}_2$, which stem from the negative crystal field split of $\Delta_{cf} = -0.03$ eV and a relatively large spin-orbit split $\Delta_{so} = 0.19$ eV. From the similarities in the valence bands dispersion in $\text{CuIn}_{1-x}\text{Ga}_x\text{Se}_2$ with



different alloy compositions,²⁶ one may expect $\Delta_{cf} \approx 0$ eV and $\Delta_{so} \approx 0.2$ eV for $\text{CuIn}_{0.7}\text{Ga}_{0.3}\text{Se}_2$, which is consistent with our experimental observation.

In summary, the ϵ spectra for $\text{CuIn}_{0.7}\text{Ga}_{0.3}\text{Se}_2$ were determined by spectroscopic ellipsometry at 40 and 300 K. From a standard lineshape analysis of ellipsometric data, a total of twelve CP energies were obtained from 2.5 to 6.4 eV, which include two additional CPs at 3.01 and 3.48 eV. Electronic origins of the observed CP features were discussed based on the results from FPLAPW calculations of the electronic band structure for $\text{CuIn}_{0.5}\text{Ga}_{0.5}\text{Se}_2$. The pairs of valence and conduction bands along the main symmetry directions of Brillouin zone were suggested for the major CP features observed in the ϵ_2 spectra.

This work was supported by the U.S. Department of Energy under Contract No. DE-AC36-08-GO28308. The work done at the Royal Institute of Technology was supported by the China Scholarship Council and the Swedish Energy Agency, and with the access to HPC resources at NSC and HPC2N through SNIC/SNAC. The work done at Kyung Hee University was supported by WCU program (Grant No. R33-2011-000-10118-0) and NRF program (Grant No. 2012-0004085) funded by the MEST.

FIG. 4. The calculated electronic band structure of $\text{CuIn}_{0.5}\text{Ga}_{0.5}\text{Se}_2$ where the CPs are identified along the main symmetry directions. Contributions of individual CPs to the ϵ_2 are shown in Fig. 3.

¹P. Jackson, D. Hariskos, E. Lotter, S. Paetel, R. Wuerz, R. Menner, W. Wischmann, and M. Powalla, *Prog. Photovoltaics* **19**, 894 (2011).

²S. Mehta, *PV News* **30**, 3 (2011).

³O. E. Semonin, J. M. Luther, S. Choi, H.-Y. Chen, J. Gao, A. J. Nozik, and M. C. Beard, *Science* **334**, 1530 (2011).

⁴C. Persson, *Appl. Phys. Lett.* **93**, 072106 (2008).

⁵M. J. Romero, H. Du, G. Teeter, Y. Yan, and M. M. Al-Jassim, *Phys. Rev. B* **84**, 165324 (2011).

⁶D. E. Aspnes, in *Handbook of Optical Constants of Solids*, edited by E. D. Palik (Academic, New York, 1985), chap. 5.

⁷S. Adachi, *Optical Constants of Crystalline and Amorphous Semiconductors: Numerical Data and Graphical Information* (Kluwer Academic, Boston, 1999).

⁸M. I. Alonso, K. Wakita, J. Pascual, M. Garriga, and N. Yamamoto, *Phys. Rev. B* **63**, 075203 (2001).

⁹M. I. Alonso, M. Garriga, C. A. Durante Rincón, E. Hernández, and M. León, *Appl. Phys. A* **74**, 6592002

¹⁰P. D. Paulson, R. W. Birkmire, and W. N. Shafarman, *J. Appl. Phys.* **94**, 879 (2003).

¹¹S.-H. Han, F. S. Hasoon, H. Al. Al-Thani, A. M. Hermann, and D. H. Levi, *J. Phys. Chem. Solids* **66**, 1895 (2005).

¹²T. Begou, J. D. Walker, D. Attygalle, V. Ranjan, R. W. Collins, and S. Marsillac, *Phys. Status Solidi (RRRL)* **5**, 217 (2011).

¹³L. Viña, S. Logothetidis, and M. Cardona, *Phys. Rev. B* **30**, 1979 (1984).

¹⁴P. Lautenschlager, M. Garriga, L. Viña, and M. Cardona, *Phys. Rev. B* **36**, 4821 (1987).

¹⁵P. Lautenschlager, M. Garriga, S. Logothetidis, and M. Cardona, *Phys. Rev. B* **35**, 9174 (1987).

¹⁶S. Zollner, M. Garriga, J. Humlíček, S. Gopalan, and M. Cardona, *Phys. Rev. B* **43**, 4349 (1991).

¹⁷T. J. Kim, J. J. Yoon, S. Y. Hwang, Y. W. Jung, T. H. Ghong, Y. D. Kim, H. Kim, and Y.-C. Chang, *Appl. Phys. Lett.* **97**, 171912 (2010).

¹⁸C. L. Perkins, B. Egaas, I. Repins, and B. To, *Appl. Surf. Sci.* **257**, 878 (2010).

¹⁹See supplementary material at <http://dx.doi.org/10.1063/1.4773362> for detailed information on the sample's microstructure and the multilayer analysis. Modeled refractive index, normal-incidence reflectivity, and penetration depth are also provided.

²⁰G. E. Jellison, Jr., L. A. Boatner, D. H. Lowndes, R. A. McKee, and M. Godbole, *Appl. Opt.* **33**, 6053 (1994).

²¹B. Johs and J. S. Hale, *Phys. Status Solidi A* **205**, 715 (2008).

²²J. E. Jaffe and A. Zunger, *Phys. Rev. B* **28**, 5822 (1983).

²³A. Savitzky and M. J. E. Golay, *Anal. Chem.* **36**, 1627 (1964).

²⁴M. Cardona, "Modulation spectroscopy," in *Solid State Physics*, edited by F. Seitz, D. Turnbull, and H. Ehrenreich (Academic, New York, 1969), Suppl. 11, p. 119.

²⁵D. E. Aspnes, in *Handbook of Semiconductors*, edited by M. Balkanski (North-Holland, Amsterdam, 1980), Vol. 2, p. 109.

²⁶R. Chen and C. Persson, *Thin Solid Films* **519**, 7503 (2011).